EUROPEAN ORGANIZATION FOR NUCLEAR RESEARCH

NP DIVISION
Internal Report 68-2
15 January 1968

THE OMEGA PROJECT

Proposal for a large magnet and spark chamber system

by the

Omega Project Working Group

67/1372/5/Rev.
SIS/mn

Preface

This report is the preliminary result of the work of a number of CERN physicists and engineers, the so-called Omega Project Working Group which was set up in April 1967. This group now consists of the following members:

W.F. Baker, W. Beusch, G. Brautti, G. Cocconi, B. French, O. Gildemeister, M. Martin, A. Michelini, M. Morpurgo, B. Nellen, G. Petrucci, P. Preiswerk, E. Quercigh, B. de Raad, C. Rubbia, K. Tittel, and P. Zanella.

This group is grateful for much help from and discussions with several other people, and especially to E. Keil, who wrote the chapter on the tolerances of an "Omega" set-up at the ISR, and to M. Borghini for discussions on the possible use of polarized targets for the "Omega".

CONTENTS

1. INTRODUCTION

During the last few years, the field of counter experiments in high-energy physics has been marked by the extensive use of spectrometer magnets associated with spark chamber systems. In most cases, because of the relatively small aperture of the magnets, a limited number of particle secondaries (≤ 2) were detected at each interaction.

For the future, it is expected that an increasing demand will arise for larger spectrometer magnets in order to perform experiments on more complicated types of interactions with detection of many secondaries over a large solid angle, with better momentum resolution and higher statistics.

To cater for these future requirements, the Omega Project Working Group has worked out, in the present report, a proposal for a large spectrometer magnet and spark chamber system to be built as a part of the improvement programme of CERN. The proposed instrument is expected to be installed during the first period of operation in the new PS West Experimental Hall and possibly later in one of the interaction regions of the ISR (see Fig. 1). The global cost of the magnet and of an optical spark chamber system including construction staff is estimated to be 13.7 MSFr. (1967 prices, and no provision is made for contingencies).

The basic idea of the project is a large-aperture spectrometer magnet and a system of spark chambers to be operated within this magnet associated to an efficient data-handling system. This relative configuration of magnet and spark chambers makes it possible to perform a new class of experiments, especially on interactions where a large number (≥ 2) of secondary particles or unstable mesons and baryons such as K^0, Λ^0, etc., have to be completely detected and measured. An additional merit of the proposed system is its ability to perform experiments on relatively simple types of reactions but with very small cross-section ($\leq 1\ \mu b$). As examples of the use of the system, we have considered various experiments such as: the study of resonances with a missing-mass trigger on the recoil proton,

and complete detection and measurement of the resonance secondaries (Section 3.1); the study of baryon exchange processes requiring an ingoing meson and a forward outgoing proton of relatively high momentum (Section 3.2); and the study of leptonic decays of hyperons (Section 3.3). These types of experiments will form a part of the experimental programme of the apparatus. However, it is impossible to foresee all the experiments that will be performed with the magnet, and the aim is therefore to build a flexible system which can be used in a large number of experiments. The experience with the CERN-ETH-Imperial College spectrometer magnet makes us confident that this can be done. It is possible to state a few general properties and requirements of the proposed system which are independent of the final design adopted.

Firstly, the magnet has to be large so that it is possible to observe complex interactions in which several charged and neutral particles are produced. As is described below, a useful magnet volume of ~ 14 cubic metres is large enough to permit:

i) use of a target mounted inside the magnet volume so as to detect charged and neutral secondary particles emitted at all angles; besides liquid hydrogen, polarized targets have also been considered. The observation of all the interaction products is particularly important when a polarized target is used and the target nucleus has to be identified.

ii) momentum measurements up to 25 GeV/c with accuracy limited by multiple scattering rather than the spatial resolution of the chamber (see Appendix);

iii) efficient detection of neutral particles and γ-rays in detectors surrounding the momentum-measuring region;

iv) possibility of operating the magnet around an interaction region at the ISR for a "4π geometry" type of experiment.

Secondly, the magnet has to be designed to permit sufficient access for counter system and spark chambers. It must also be possible to perform experiments using optical or wire chambers inside the magnet. Both types of chambers have important advantages for certain classes of experiment. An isometric view of the magnet is shown in Fig. 2.

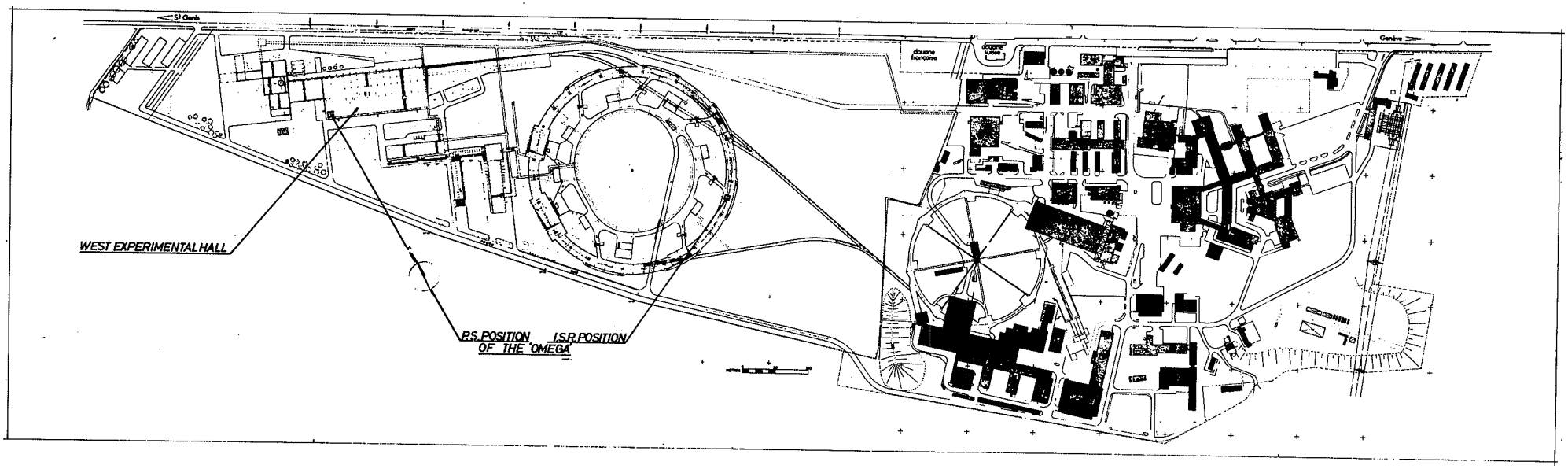

FIG.1. PROPOSED POSITION OF THE OMEGA MAGNET

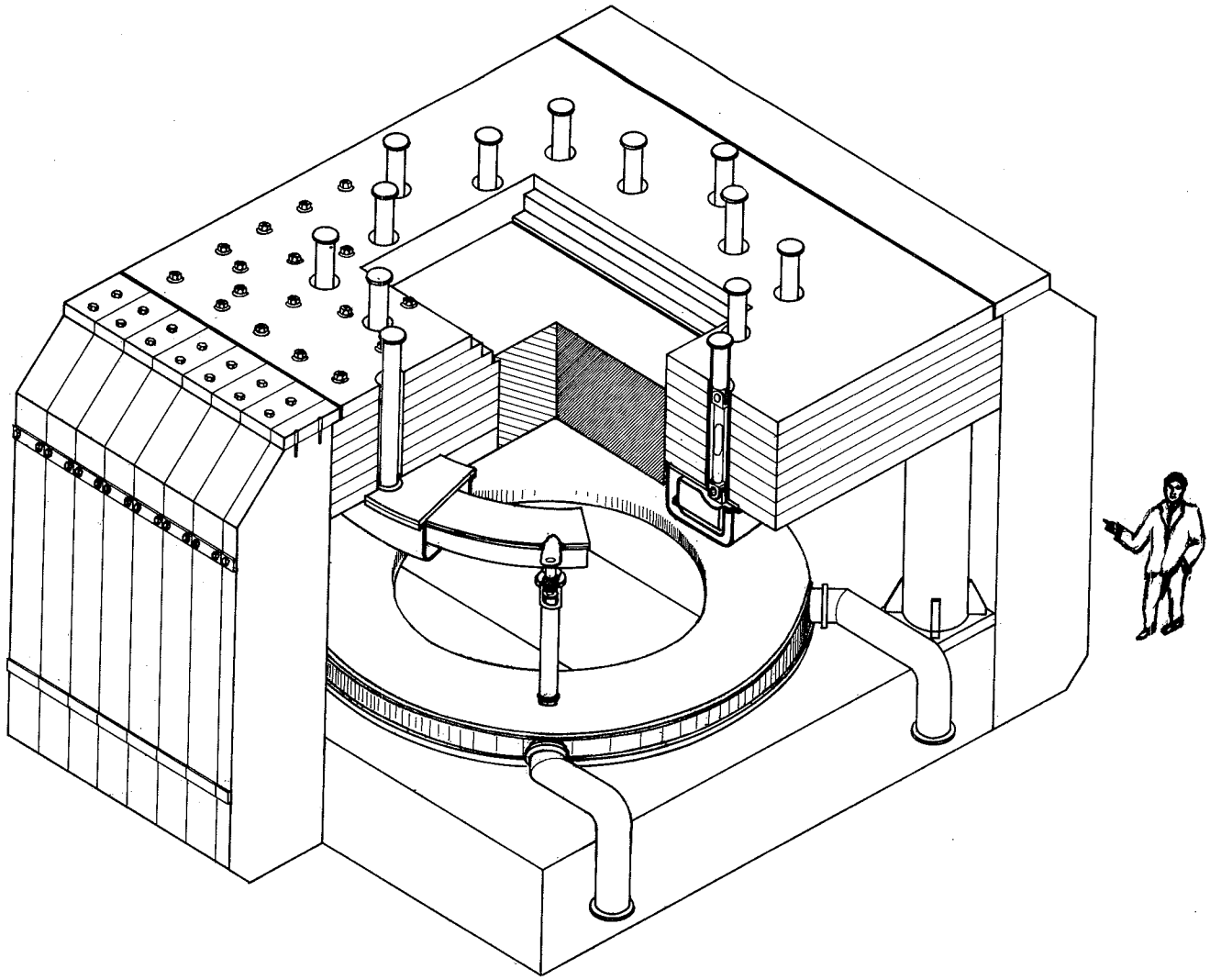

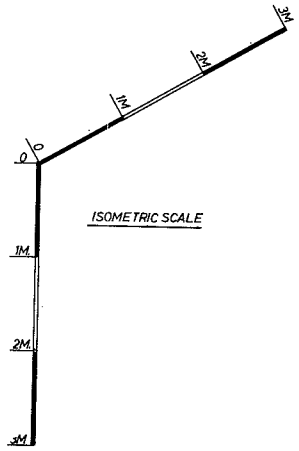

FIG 2. ISOMETRIC VIEW OF OMEGA MAGNET

Its main characteristics are:

pole face, circular	3 m diameter
gap between poles	2 m
gap between coils	1.5 m
field at the centre (top pole removed)	17 kG
weight	1300 t

Either conventional or superconducting coils could excite the magnet. In this paper both versions are considered for a field of 17 kG.

Because of the large size and weight the magnet has to be considered as a fixed installation in the experimental area where it is mounted.

Initial experiments would probably use optical chambers, as there is now considerable experience of HPD measurement of spark chamber photographs and a well-developed system of analysis programmes.

To avoid major changes of analysis programmes and of the evaluation of optical distortions between experiments, one has to develop a basic optical system associated with particular geometries of spark chambers, and, as far as possible, confine apparatus changes to changes of target, triggering systems, and perhaps the material of some of the spark chamber plates. So a large number of experiments can be performed in a short time -- a desirable feature of this apparatus.

A system of wire chambers with on-line computer needs development, testing, and programming work. Much of this can be done during the construction of the new system. The possibilities of wire chamber read-out in a magnetic field are discussed in Section 4.1.

The data handling clearly represents a fundamental aspect of the whole project. As is shown later, the total number of events to be analysed is between 2 and 10 millions per year for optical chambers, depending on the type of experiment and camera dead-time. A factor of ~ 5 increase is expected in the case of wire chambers.

It is proposed that a fixed amount of the analysis load be handled inside CERN (~ 2 - 3 million events per year) and the rest in European laboratories and universities. Two different schemes for the data handling including HPD, computer on-line, and general computer facilities, have been considered so far (Section 2.5). The two schemes differ by the amount of computation which is assigned to the CERN Central Computing Facility. While the first foresees that the data reduction up to the geometrical reconstruction be done on a computer specially assigned to the project, the second relies on the CERN Central Computer Facility for all stages of the analysis.

1.1 Construction programme and costs

On the assumption that the detailed design work can start now and that the final decision on the project can be made until the middle of 1968, the project could probably be finished in 1971. Figure 1.1 shows a time scale of the project.

The total costs are listed below. They are estimated on the basis of present prices. (The data handling system is listed separately since it is not yet clear how the budgeting will be handled.)

Experimental part:

Magnet, refrigerator, etc. (superconducting coil)	MSFr.	9.5
Spark chambers, optics, etc.,		1.7
Staff during construction period		2.5
Total	MSFr.	13.7

Data-handling system: (first of the proposed versions)

Computers	MSFr.	5.7
HPD, interface, scanning tables, links		1.9
Buildings		0.6
Total	MSFr.	8.2

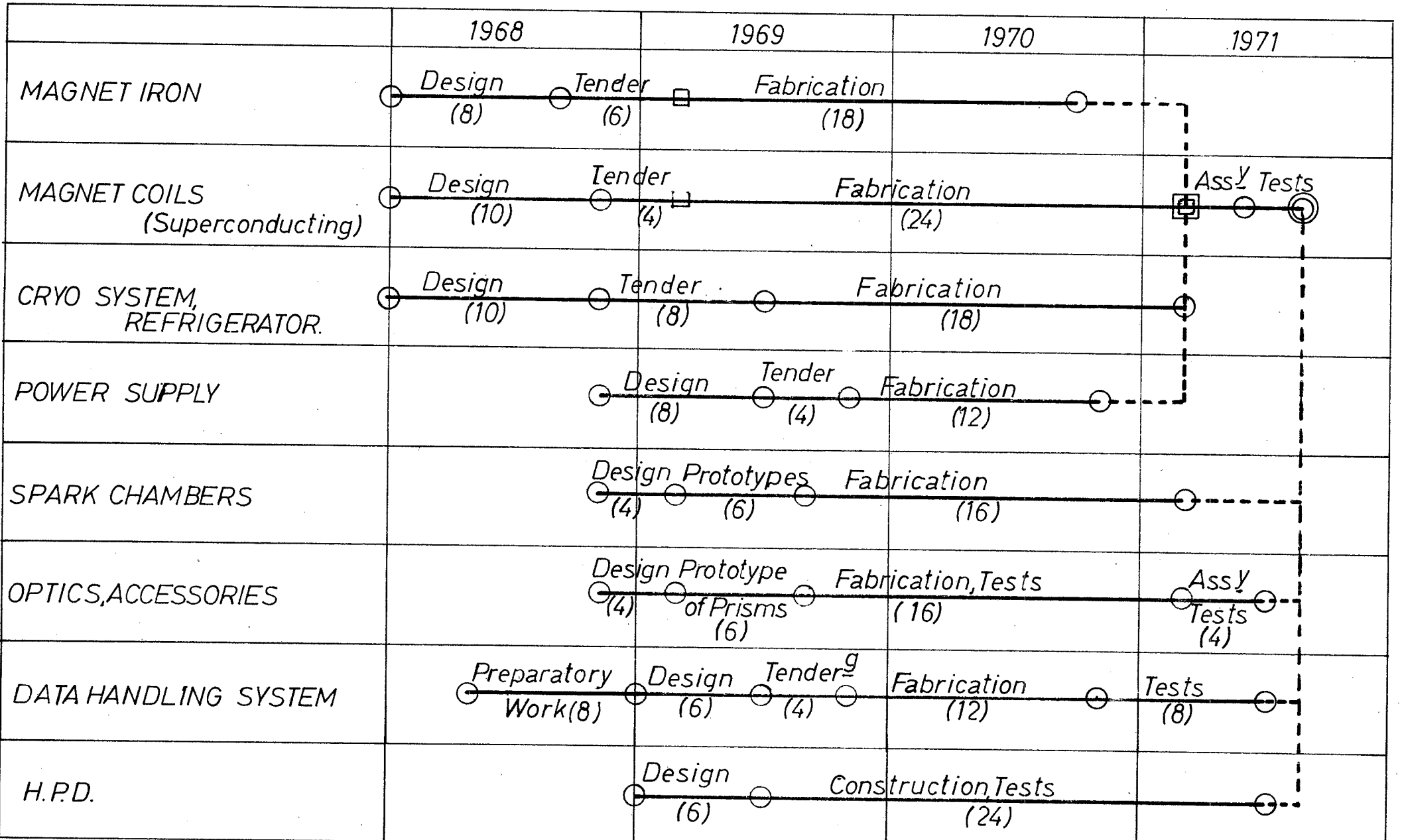

PROJECT PLAN

FIG 1.1.

The running costs*) for staff, power, maintenance, film, and tape are estimated at 2.2 MSFr./year if superconducting coils are used. In addition, the required central computer time would correspond to one-quarter of the time of a CDC 6600.

The expected distribution of the costs over the years will be

	1968	1969	1970	1971	Total
Experimental part	3.0	2.7	3.2	4.8	13.7
Data handling	-	4.1	4.1	-	8.2
Total	3.0	6.8	7.3	4.8	21.9

* * *

*) including the analysis up to the event recognition by means of the first of the proposed versions of the data-handling system.

67/1372/5
SIS/ma

2. DETAILED DESCRIPTION OF THE PROJECT

2.1 Magnet

The general characteristics of the magnet are:

max. magnetic field at the centre	=	17 kG
inner diameter of circular coils	=	3.0 m
free gap between coils	=	1.5 m
free gap between poles	=	2.0 m

At a first approximation, taking the fringing field into account, the bending power of this magnet will be = 7.2 Wb/m.

A magnet having the above-mentioned characteristics can be designed either with superconducting or conventional copper coils. Both solutions have been studied in some detail; a decision as to which of the two alternatives will be used has not yet been taken. A cost estimate for both solutions is given below (Section 2.6).

The magnet coils will be circular because this simplifies the construction and makes it more economic, without adding any major inconvenience with respect to coils of other shapes.

A general layout of the magnet in the case of superconducting coils is given in Fig. 2.1.1.

2.1.1 Iron core

The two horizontal yokes [item (1)] of the magnet are spaced apart by means of four pillars (2) which are designed to withstand the weight of the iron and the attracting magnetic forces which are of the order of 3000 tons. The top and bottom horizontal yokes are obtained by bolting together a number of relatively thin (15 cm) steel plates. The rectangular windows (3×1.5 m^2) can be filled by removable pole pieces (4). The vertical yokes (3) are subdivided into a number of slabs (40 cm thick) which can be mounted in various positions along the perimeter of the horizontal yokes, so as to leave side apertures where required by the experimental needs.

The weight of the largest individual magnet part does not exceed 40 tons. The total weight of the iron is approximately 1300 tons.

2.1.2 Superconducting coils

The coils are wound with fully stabilized superconducting cable, and will provide a maximum number of 2×10^6 ampturns per coil, with an average current density of 1600 amp/cm^2 within the coil cross-section. In these conditions, the field at the magnet centre will be at least 17 kilogauss when the top pole is removed.

Each coil is suspended from 16 stainless steel legs (6) which will be able to withstand a total vertical force of approximately 600 tons. Tangential rods will clamp the coils against forces in the horizontal plane. Each coil will be able to withstand a maximum horizontal force of approximately 300 tons.

The clamping system of the coil is designed in such a way that the thermal contraction of the coil will not prevent operation.

The coils are immersed in liquid helium contained in the reservoirs (7). Helium consumption is given by radiation and transmission losses, and by the ohmic dissipation of the current leads.

Assuming that the warm ends of the coil clamps are kept at liquid nitrogen temperature, the heat losses through the vertical and horizontal clamps are < 50 watts per coil.

The radiation losses with a 3 cm thick layer of superinsulation and no nitrogen shield are approximately 15 W/coil. The heat dissipation through current leads capable of carrying 5000 amps will be 20 W/coil. Therefore a refrigerator having a power of 500 W at 4°K should be sufficient.

2.1.3 Conventional coils

The conventional coils can be designed for the same iron yoke, and they will consist of a number of pancakes wound with water-cooled hollow copper conductor. Approximately 75 tons of copper will be required. The electric power will be 7.5 MW.

2.1.4 Model magnet

In order to have more detailed information on the field configuration and to allow a better magnet design, a reduced scale model (1 : 10) has been constructed. A general view of this model is shown in Fig. 2.1.2. The model

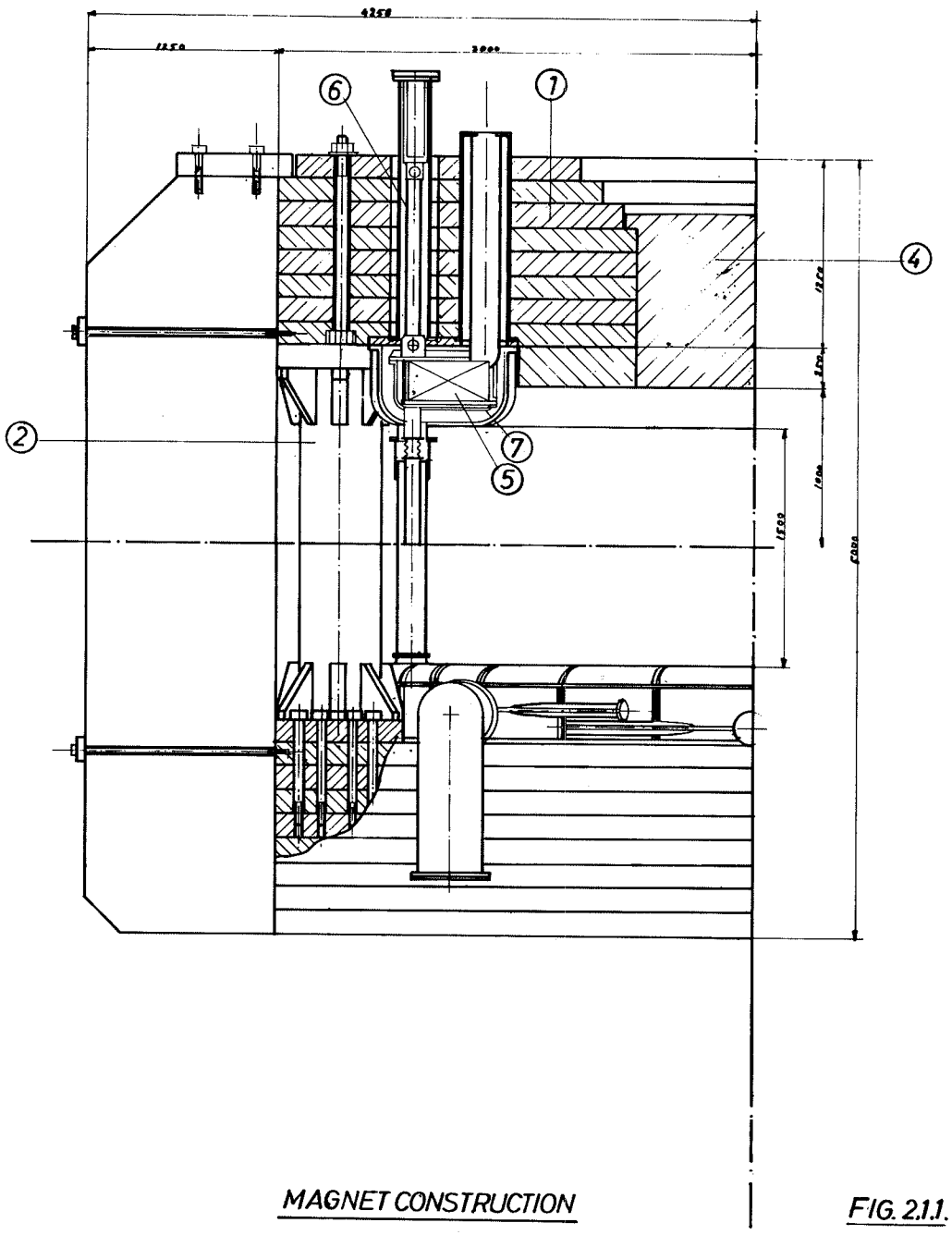

MAGNET CONSTRUCTION

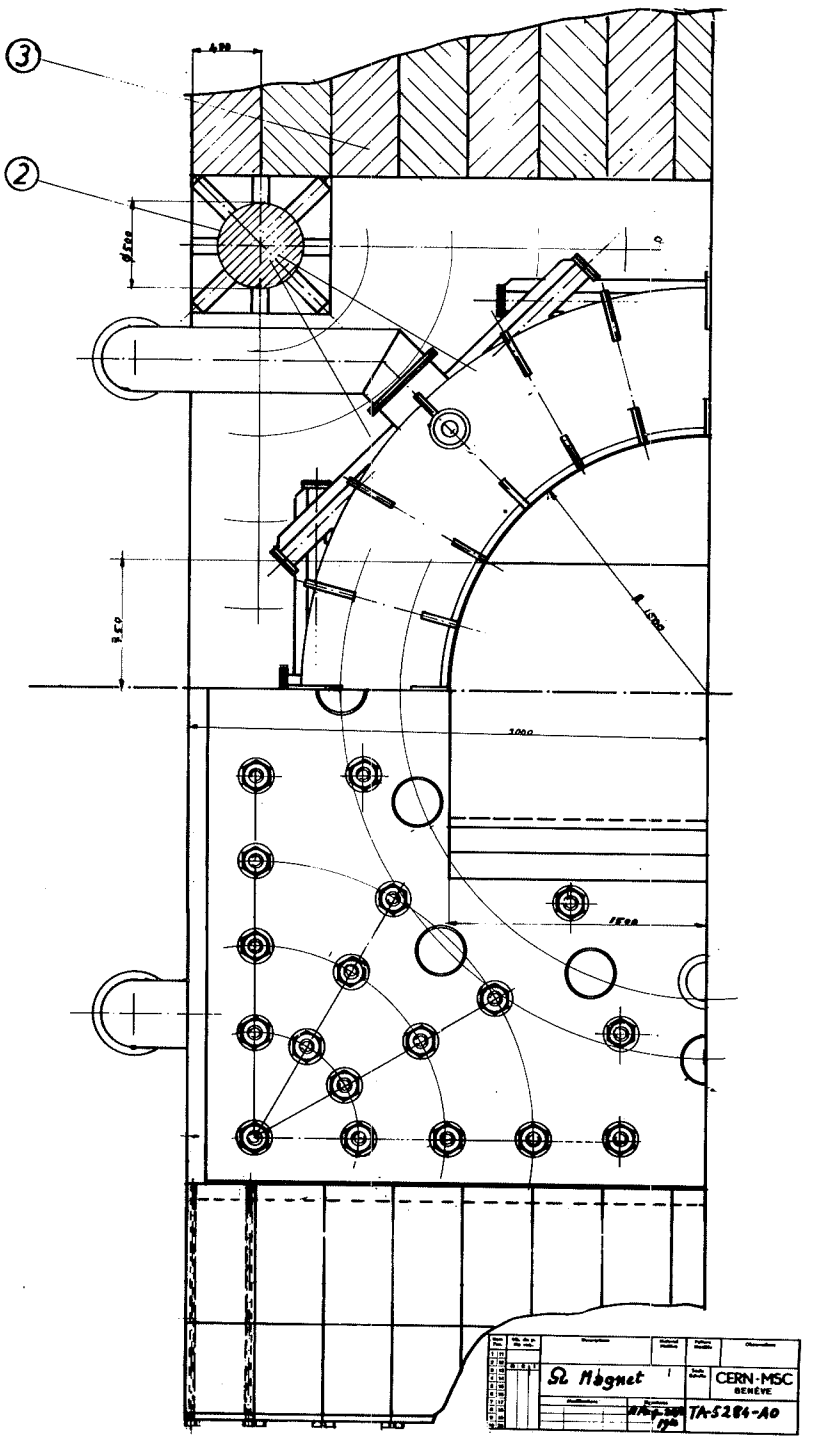

FIG. 2.1.1.

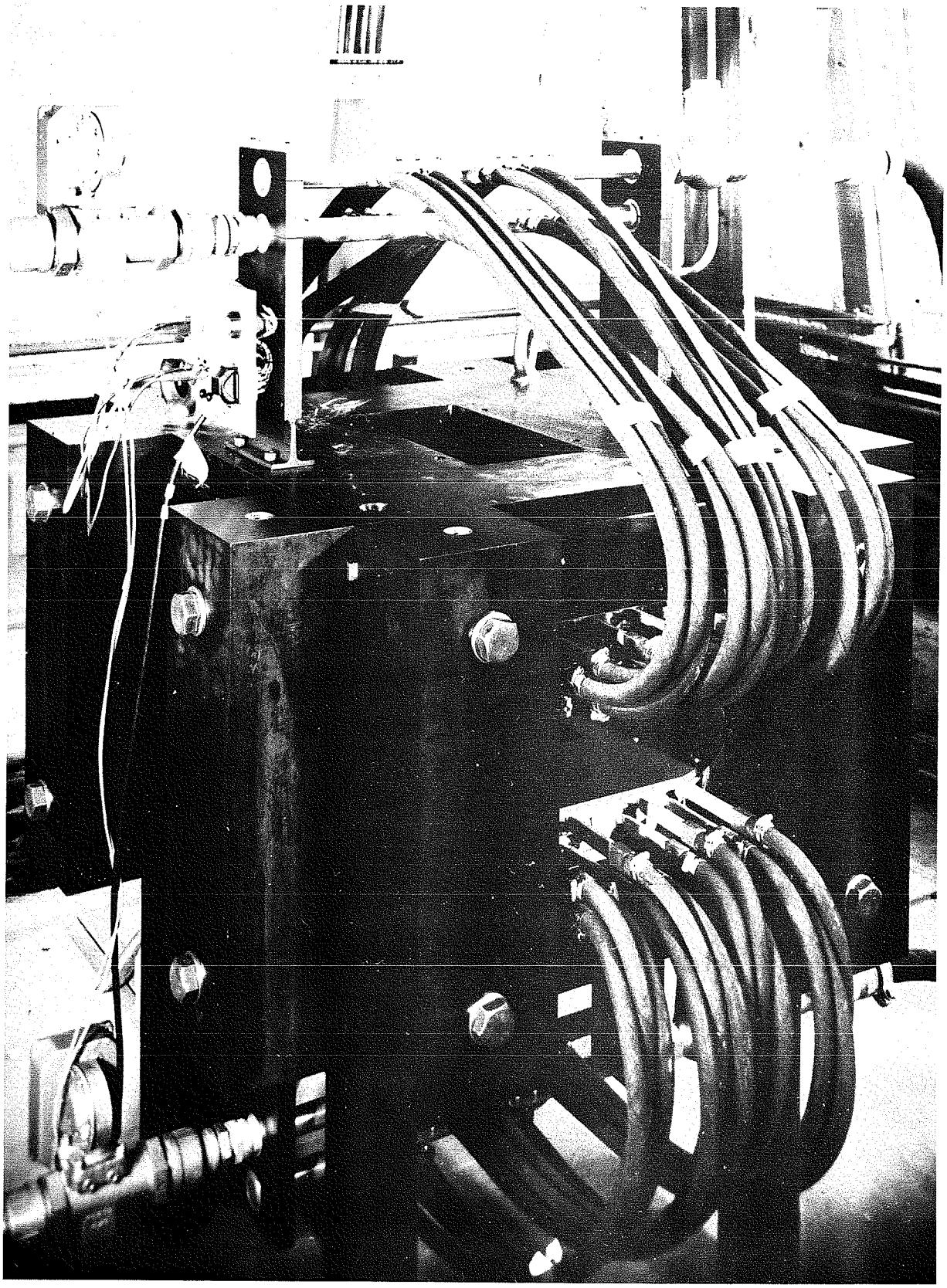

Fig. 2.1.2 Model magnet

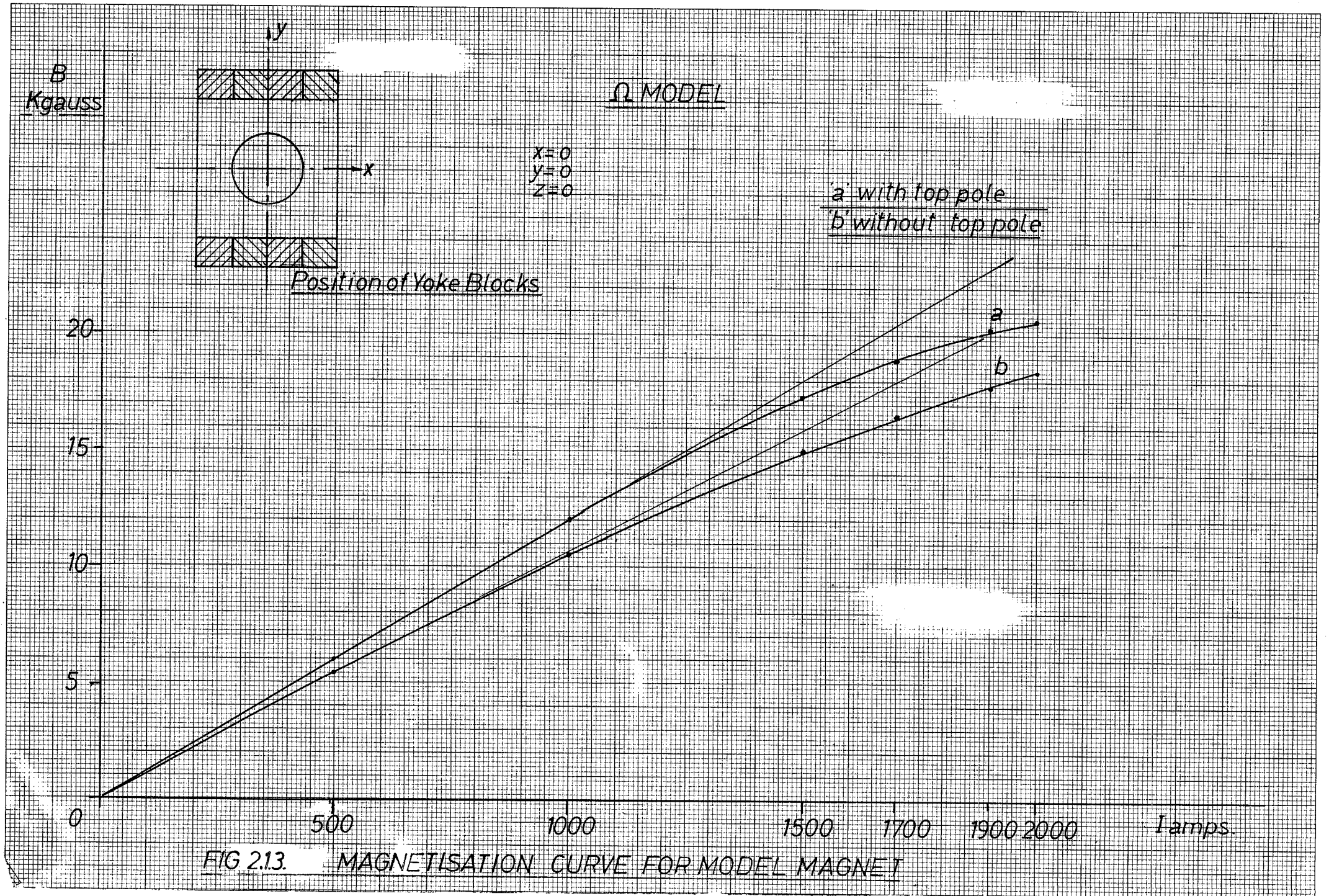

FIG 2.1.3. MAGNETISATION CURVE FOR MODEL MAGNET

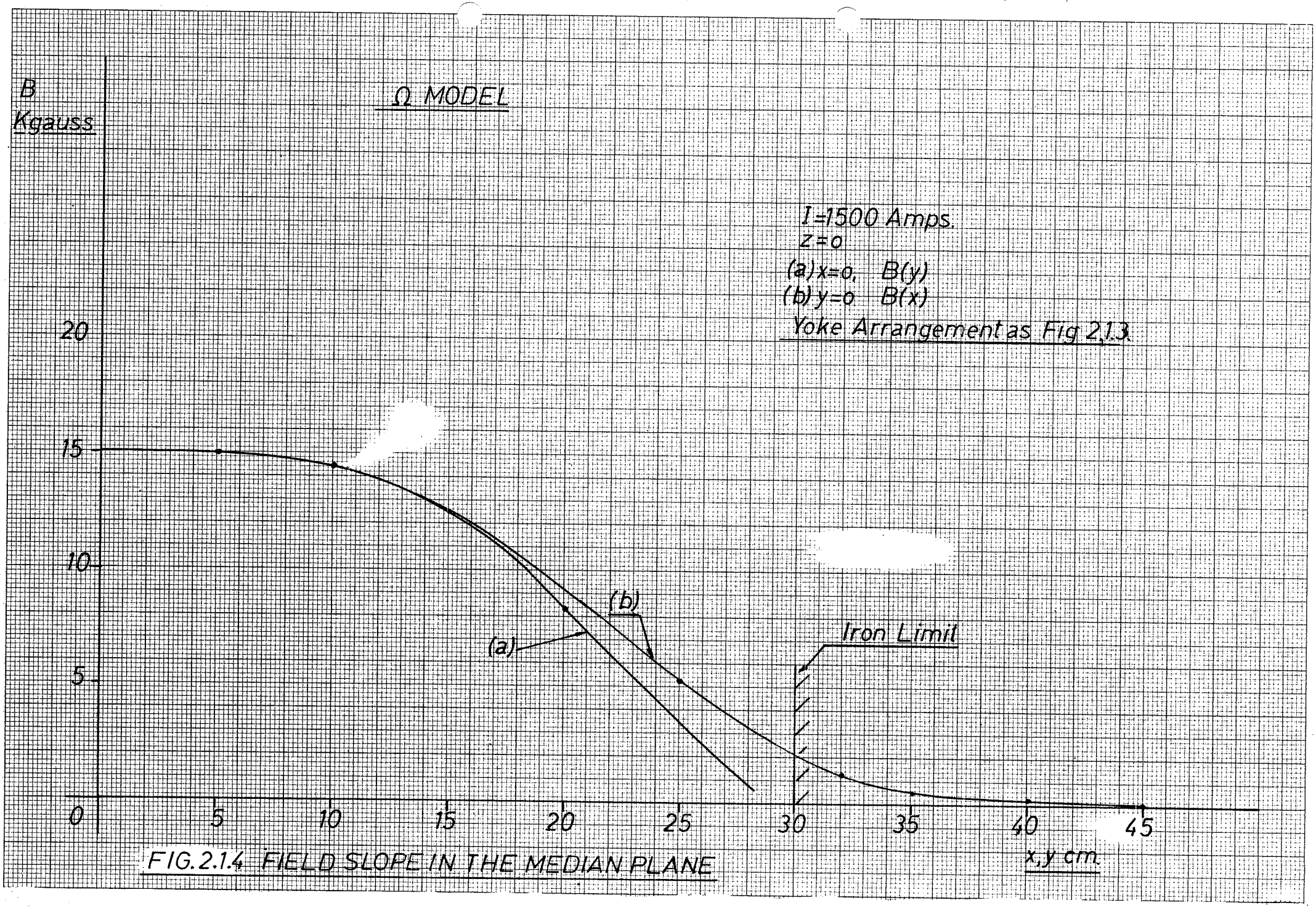

FIG. 2.1.4 FIELD SLOPE IN THE MEDIAN PLANE

magnet is energized by two conventional water-cooled copper coils and requires a power of about 0.7 MW.

In the model as well as in the full-scale magnet the top pole-piece is removable and the side yokes can be mounted in various positions.

Figures 2.1.3 and 2.1.4 give the results of preliminary magnetic measurements on the model.

2.2 Spark chambers and optics

2.2.1 Optical spark chambers. For optical spark chambers we have to consider the following types:

- sampling spark chambers; many gaps of $\approx$ 1 cm;
- wide-gap chambers, the spark follows the track up to a certain angle; gaps of 10 cm or more;
- isotropic streamer chambers, the track is displayed by localized streamers.

These chambers may be in plane, cylindrical, or other geometries and contain opaque (foil) or transparent plates (wire mesh).

For the time being, we base the discussion on sampling spark chambers with opaque parallel plates. This very conservative approach results in an extrapolation of an existing magnet spark chamber (CERN-ETH-I.C.-group). We can, therefore, give reasonably safe predictions on the feasibility of chambers and optical system, accuracy in track parameter measurement, and scanning and measuring problems. Obviously, the system described here is not optimal for all experiments, and sufficient flexibility must be built into the camera and the HPD measuring technique in order to cope with other, more complicated, chamber arrangements.

2.2.2 Spark chamber arrangement. A possible arrangement is shown in Fig. 2.2.1. All gaps are perpendicular to the beam direction except for two gaps on one side of the system which are parallel to the beam. The gap width is 1 cm. The frames holding the foils may be chosen to be 1.5 cm thick giving an (active space)/(dead space) ratio of 2 : 3. The frames should be as thin as possible on one side in order to allow low momentum particles to leave the spark chamber at the side to be used for triggering. A "typical event" is shown in Fig. 2.2.1.

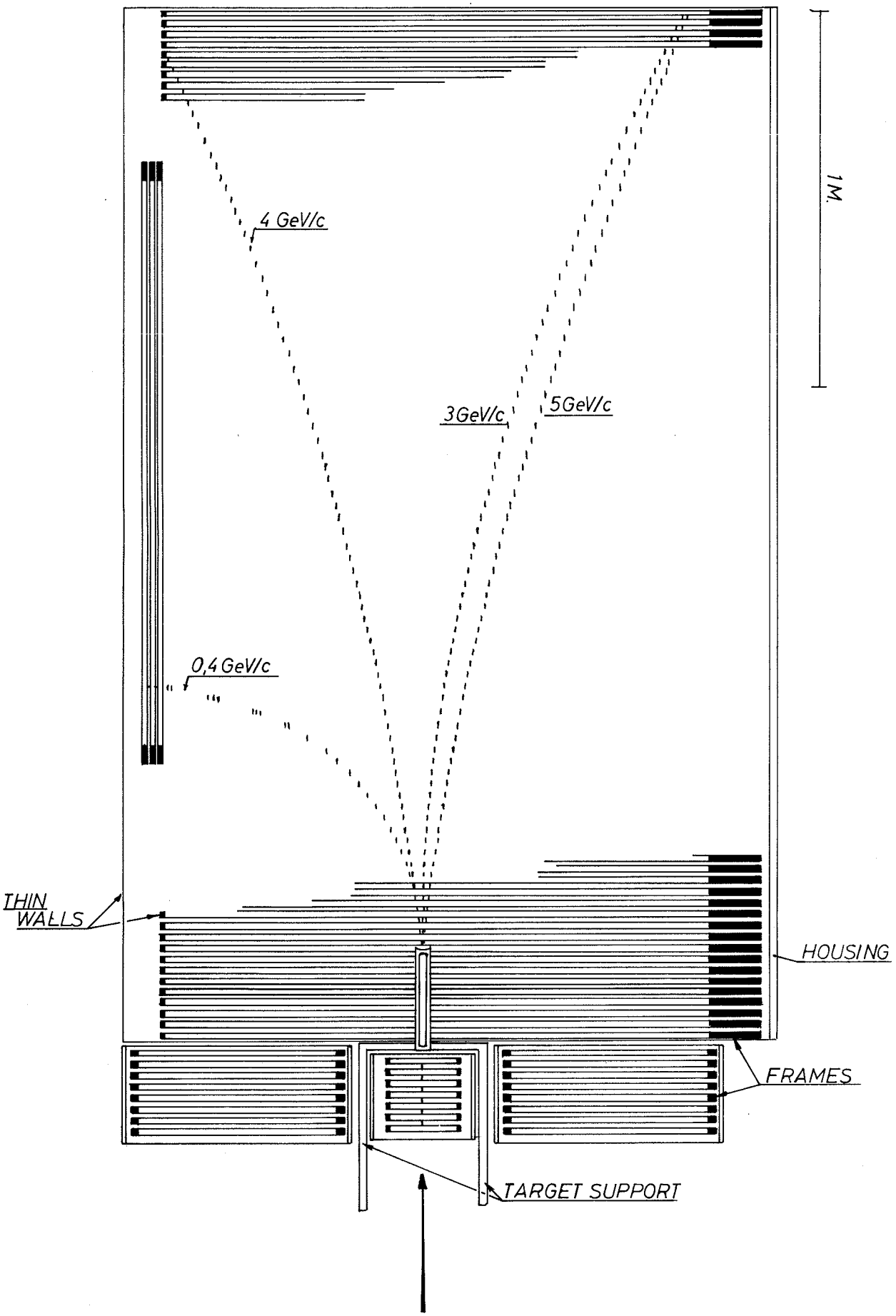

FIG. 2.2.1. TOP VIEW OF TARGET & SPARK CHAMBER

The material of the spark chambers should be kept to a minimum. Aluminium foils of 25 μ thickness are commonly used. Thinner foils, e.g. 10 μ, would be preferable but are difficult to handle. Taking into account the contributions of the aluminium in the foils and the neon in the gaps, one finds for the radiation lengths L_o

$$25\ \mu\ \text{Al} : L_o = 38\ \text{m}$$
$$10\ \mu\ \text{Al} : L_o = 83\ \text{m}$$

Any system of spark chambers (also wire) with planes oriented in more than one direction calls for some supporting structure inside the active volume. A very light one is proposed by A. Roberts*). These Al/plastic-foam/Al sandwiches have a radiation length of 24 m. A system with a minimum of material near the target is obtained if the target is located inside a cylindrical hole in the spark chamber plates. It has been found that the foils stay flat if a hole is cut with appropriate care, for example by galvanic etching.

Particle trajectories at a large angle to the beam direction will be poorly resolved in such a system. Figure 2.2.3 shows a track turning parallel to the spark chamber planes. Such tracks are quite well recorded in a sampling spark chamber. Since the particles in question generally have low momentum, a large relative momentum error results in a moderate error in the over-all momentum balance.

2.2.3 Optical system

This spark chamber system inside the magnet has to be photographed from the top with small-angle stereoscopy. In the case of parallel plates, a cylindrical lens of some kind is needed to bend the light from the sparks, emitted parallel to the plates, into the camera lenses. We believe that a system with a prism for each gap is simpler and more accurate than other

---

*) S. Bernstein et al., Purdue Instrumentation Conference on High-Energy Physics, May 12-14, 1965.

solutions (mirrors, cylinder lens, etc.). Machining and polishing perspex prisms to the tolerances required seems to be just at the limit of the state of the art.

The light paths are shown in Figs. 2.2.4 and 2.2.5. We propose to use 70 mm film (future standard perforation) and put the two stereo views side by side. This choice poses some problems for HPDs outside CERN that are designed for the 50 mm film of the 2 m HBC. However, 70 mm film is also foreseen for the 3.5 m HBC. Possible parameters of the optical system are:

- Optical distance to beam height — 5 m
- Stereo angle — 17°
- Proportionality constant for depth measurement — $dz/d(y_2 - y_1) = 3.5$
- Demagnification — m = 50
- Focal length of lenses — 10 cm
- Width of spark image on film — 0.04 mm
- Length of spark image on film — 0.2 mm at centre, 0.15 mm at far end
- Two images 30×60 mm^2 side by side on film, frame length $\approx$ 8 cm

A larger stereo angle could be reached by reducing the optical distance. This would increase the variation of the spark image length and the systematic errors of the prism system. These errors introduce here a maximum apparent shift of spark position of 0.95 cm along the beam line. The corresponding sparks will be photographed after one reflection by a chamber plate surface; no appreciable error in position is introduced.

2.2.4 Spatial resolution

The r.m.s. spark position fluctuation in small-gap chambers is known to be somewhat less than 0.2 mm. Optical system and measurement should introduce only smaller errors. In the existing magnet spark chamber the combined random errors of optics and measurement are 0.09 mm in space*).

This may be looked at as a 5% error in centring on the width of a spark, and might be explained entirely by the non-uniformity of spark shapes. Under this assumption, about 0.1 mm of random error would also be expected in the proposed chamber, since the variation of spark shape

*) Astbury et al., Nucl. Instr. and Methods 46, 61 (1967).

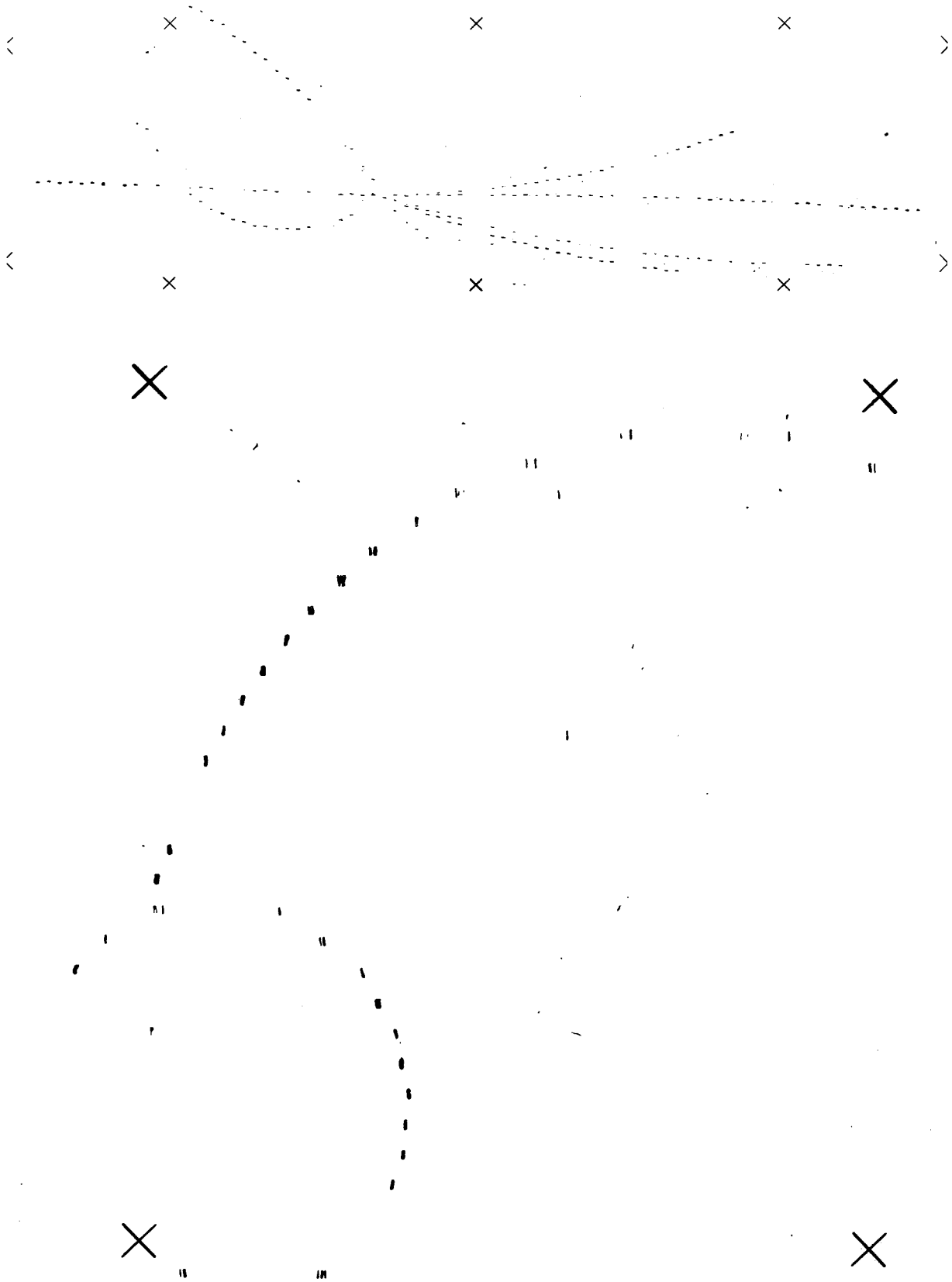

Track photos taken with the CERN-ETH system

Fig. 2.2.2 typical many body reaction

Fig. 2.2.3 low momentum tracks

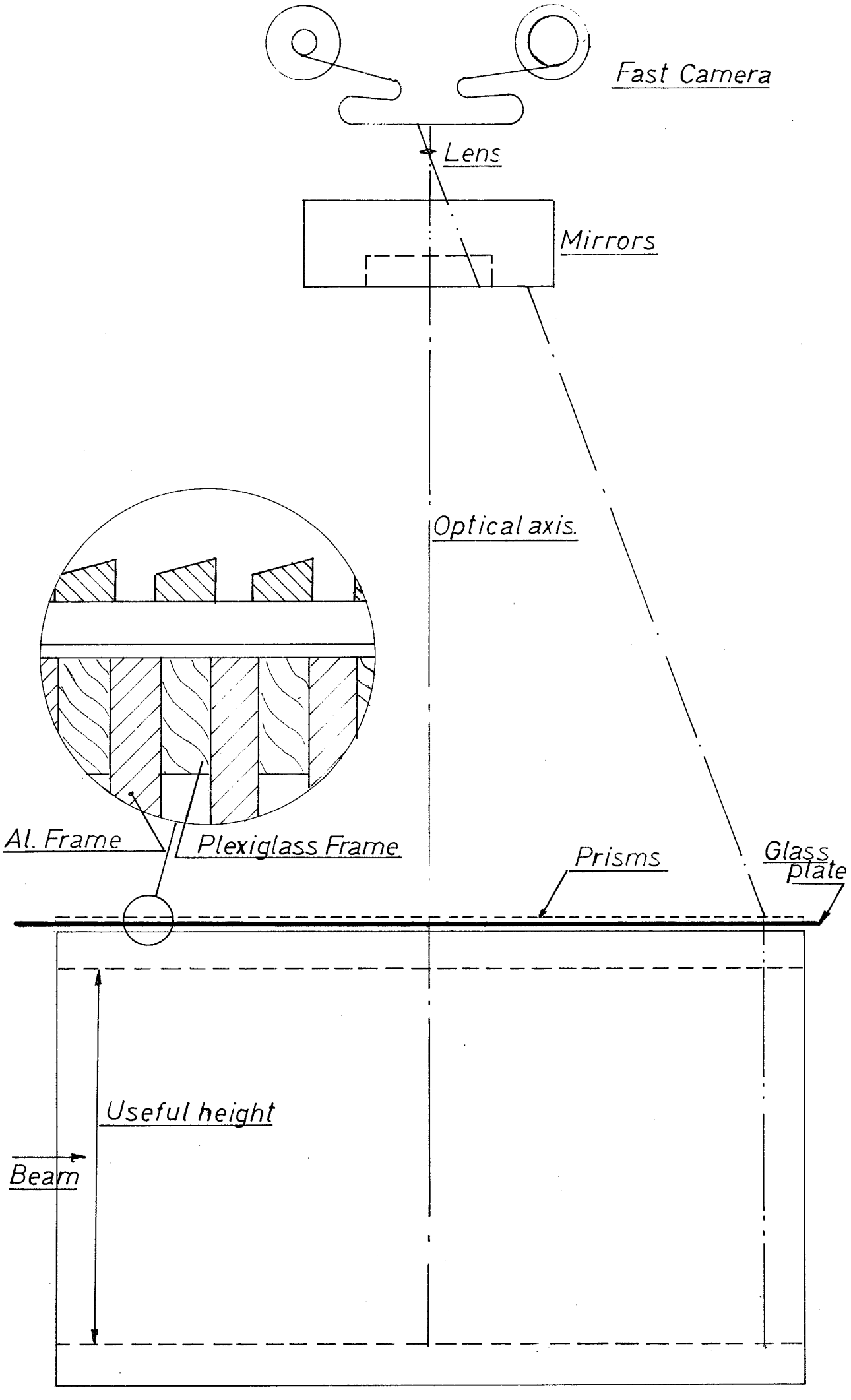

OPTICAL SYSTEM, SECTION ALONG BEAM. FIG. 2.24

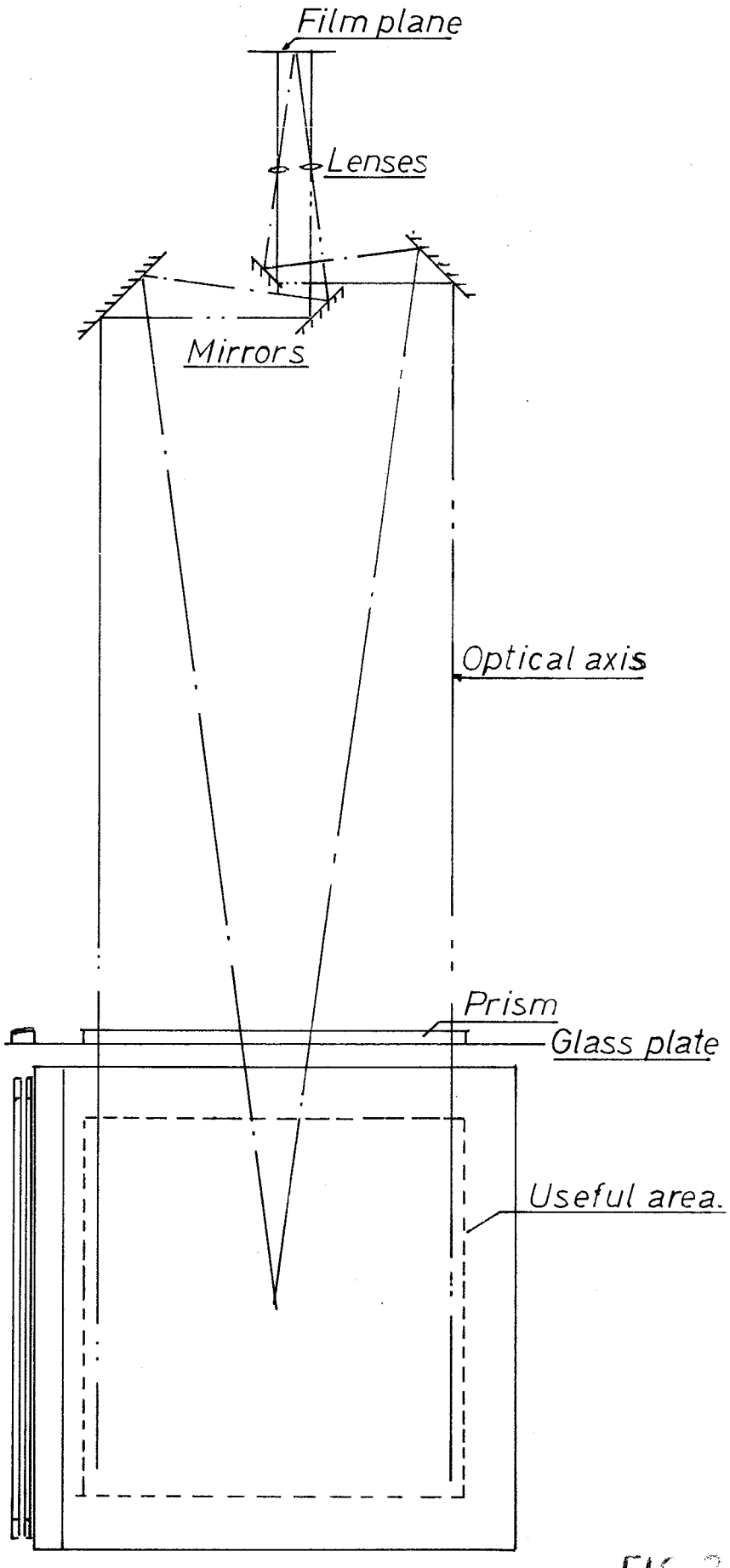

FIG. 2.5.

OPTICAL SYSTEM, SECTION ACROSS BEAM DIRECTION.

is unlikely to change with the size of the chambers. This assumption gives a lower limit. An upper limit of 0.2 mm is obtained if this random error is thought to come from any combination of:

- imperfections of optical surfaces (prisms)
- film resolution
- HPD resolution

which would all increase with the linear dimensions, the picture size being kept constant. It seems unlikely that the error will be mainly due to film and HPD resolution (4 μ on film). One can therefore hope to approach the 0.1 mm random error due to measurement and optics, provided the mirror and prism surfaces are sufficiently good.

The larger demagnification might create some problems of contrast due to the variation of spark brightness; however, the difficulties appear less severe than those met in a large bubble chamber.

2.2.5 Conclusion

The extrapolation of the present $60 \times 66 \times 160$ cm^3 magnet spark chamber to a $150 \times 150 \times 300$ cm^3 system, doubling the demagnification, seems to be possible without the need of introducing new techniques.

2.3 Beam layout

To make the best use of the Omega apparatus, beams with high momentum resolution, good intensities, and large momentum range are needed. A possible design of two beams covering different energy ranges and satisfying these requirements is shown schematically in the optical diagrams of Fig. 2.3.1.

The features of these two beams are the following:

	High-energy beam	Medium-energy beam
Maximum momentum	24 GeV/c	8 GeV/c
Angular acceptance	10^{-4} sr	4×10^{-4} sr
Production angle	0 - 20 mrad	0 - 50 mrad
Momentum bite	± 2%	± 2%
Momentum resolution	± 0.05%	± 0.1%
Total length of the secondary beam	≃ 140 m	≃ 70 m
Bending magnet length required	≃ 14 m	≃ 7 m
Quadrupole magnet length required	≃ 18 m	≃ 14 m

The high-energy beam is a four-stage beam; the first two stages are intended to provide momentum selection and reduction of background; the third stage is used to perform momentum analysis; the fourth one compensates the momentum dispersion and matches the beam to the experiment target.

The medium-energy beam has only three stages. Actually, the first stage provides momentum selection and sufficient background reduction, so that in the second stage the momentum analysis can be performed.

In both beams the momentum analysis is done by means of a rather large bending (8° in the h.e. beam and 10° in the m.e. beam) and of three hodoscopes (A,B,C). Hodoscope B is placed in a position where in the analysis plane an optical image of A is formed. Hodoscope C, which should provide only a very rough resolution, is used to divide the angular acceptance of the beam and thus reduce the errors due to chromatic aberrations. To achieve the desired momentum resolution, hodoscopes A and B should provide

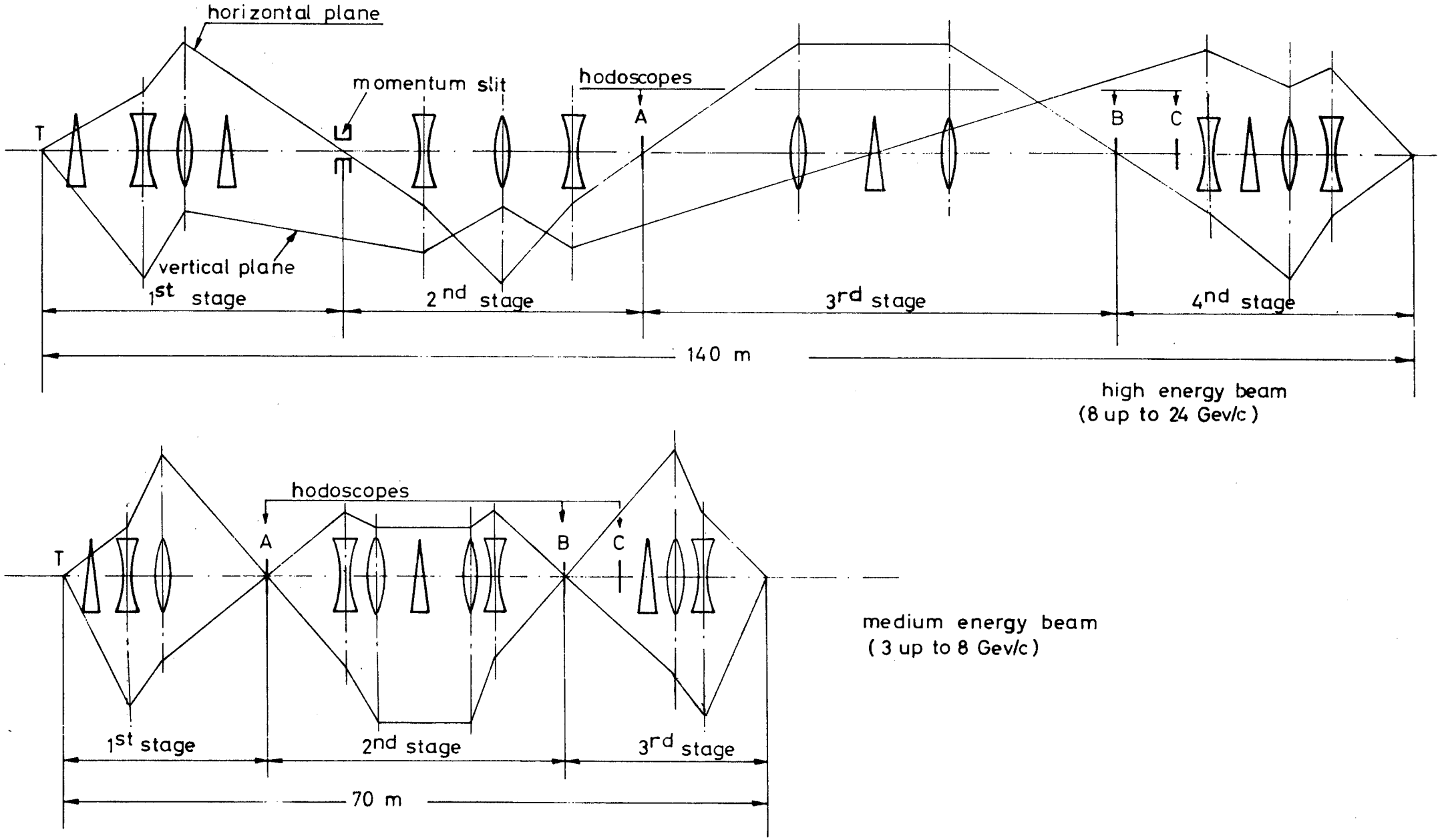

Fig. 231. Optical diagrams of high momentum resolution beams

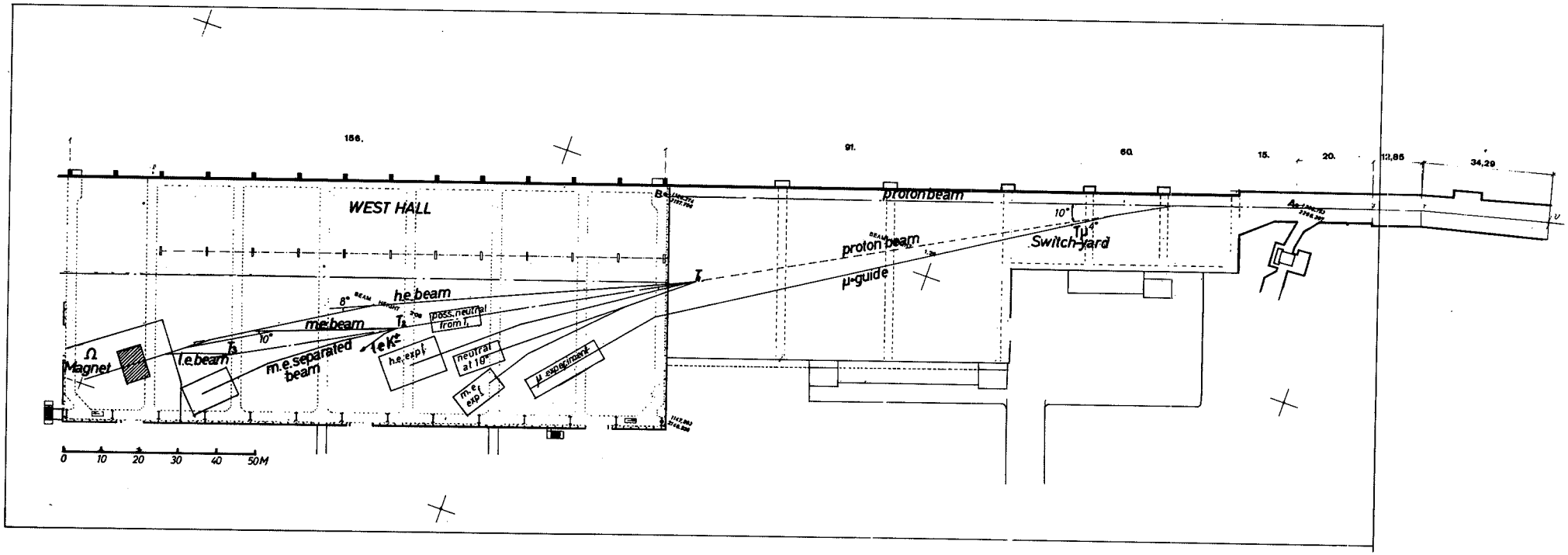

FIG. 2.3.2. LAYOUT OF BEAMS

a space resolution of about 1.5 mm for the first beam, and about 3 mm for the second one. Multiple scattering in the three hodoscopes does not, in practice, influence the precision of measurements.

The expected intensities at the end of the two beams can be deduced by the curves shown in Fig. 2.4.15, taking into account the appropriate solid-angle acceptances and path length of the two beams.

Figure 2.3.2 shows a general layout of possible counter beams in the West Hall. The two high-resolution beams described above are shown to supply the Omega area as well as a possible lower energy separated beam (below 3 GeV/c). Because of the different beam lengths, different targets have to be located along the proton line. This line crosses the whole West Hall. It starts at the far end of the switch yard under 10° to the bubble chamber proton line, which runs along the building. Several other conventional beams starting from the three targets used for the Omega beams are also indicated as well as a muon guide. It must be noticed that the beams for the Omega will be deflected also vertically to compensate for the difference in level between the Omega medium plane and the proton lines (0.5 - 1 m).

A possible improvement in the Omega exploitation of beams could be achieved by mounting long-pulse RF mass separators in the beam. Such separators could speed up considerably all the experiments when positive particles are requested, especially in the high-energy range where the protons constitute a very large fraction of the positive secondaries. [See first draft report of the Working Group on Long-Pulse RF Separator (5 April 1966).]

2.4 Beam intensities and data-taking rate

The purpose of this Section is to estimate the rate of events to be analysed per year and the corresponding beam intensities required.

As it will be shown below, the results of this estimate depend upon various assumptions, which have to be considered, on the operation of the PS, the beam, the spark chamber system and on the type of experiment performed. We will, therefore, present first a list of all the assumptions made (Section 2.4.1), we will then describe briefly the way the calculations have been carried out (Section 2.4.2), and finally we will discuss the results (Section 2.4.3).

2.4.1 The assumptions made can be listed as follows:

PS and beam operation

Some of the parameters assumed are:

i) PS energy	19.2 GeV	19.2 GeV	25 GeV
ii) Beam pulse	0.2 sec	0.5 sec	0.2 sec
iii) PS cycle	1 sec	1.5 sec	2 sec

Further parameters are:

iv) A PS running efficiency of 50% due to machine maintenance

v) A beam halo of 0% to 100% *)

vi) A beam attenuation of 10% in the target and eventually in counters surrounding the target. This attenuation is responsible for the accidental interactions (see below).

---

*) A beam halo of 100% means that the beam which traverses the spark chamber has twice the intensity of the beam focused in the beam telescope.

vii) Different kinds of "wanted beam particles" represent different fractions of the total beam intensities. We have considered the two cases of 100% beam fraction (as π^-, p) and 1% beam fraction (as K^-, $\bar{p}$).

Spark chamber operation

viii) A spark chamber memory time of 1.5 μsec.

ix) Dead-time (camera dead-time in the case of optical spark chambers) from 0 to 0.2 sec.

x) Spark chamber operation with unprotected plates (referred to as B. + INT.) when both accidental beam particles (B.) and accidental interactions (INT.) can be associated with a trigger.

xi) Spark chamber operation with protected plates (referred to as INT.) when the spark chamber plates are rendered insensitive in the region traversed by the beam particles so that only accidental interactions (INT.) can be associated with a trigger.

Experiment

xii) Trigger level*) from 10^{-6} to 10^{-4}.

xiii) For a "useful trigger" there are not more than two accidental beam particles and there are no accidental interactions associated with the triggering event.

xiv) A fraction of 50% of the total number of recorded events are good events which have to be measured.

xv) A 100% running time of the Omega spectrometer and a data taking time of 50%.

---

*) Trigger level is the ratio of triggers to the number of the "wanted" beam particles focused in the beam telescope.

2.4.2 By using the above assumptions the estimate is performed through the following calculations.

Firstly, the number of triggers recorded per PS cycle is calculated on the assumption of an exponential distribution of the time intervals between two subsequent triggers for a given dead-time [Section 2.4.1, point (ix)]. Secondly the efficiency for having a "useful trigger" is calculated [see Section 2.4.1, point (viii)]. This efficiency is then used to obtain from the total number of triggers the number of useful triggers recorded per PS cycle.

Finally from these values we estimate the rate of events per year to be measured by making assumptions on various PS and data-taking efficiencies [Section 2.4.1, points (xiv) and (xv)].

2.4.3 The results are presented in Figs. 2.4.1 to 2.4.14. Figure 2.4.1 shows the number of triggers recorded per PS cycle as a function of the trigger level for different values of the spark chamber system dead-time. For a given value I of the beam intensity the trigger level scale has to be multiplied by the factor $I/1.6 \times 10^6$ to obtain the appropriate number of triggers. For the following calculations only the two cases of 0.01 and 0.05 sec dead-time have been considered.

Figure 2.4.2 shows the efficiency for "useful triggers" [as defined by Section 2.4.1, point (viii)] as a function of the beam intensity. Various cases are considered according to the assumptions made on beam pulse, beam halo, unprotected and protected spark chamber plates [see Section 2.4.1, points (ii), (v), (x) and (xi)].

Figures 2.4.3 to 2.4.6 show the number of "useful triggers" recorded per PS cycle as a function of beam intensity.

Figures 2.4.7 to 2.4.10 show the maximum number of "useful triggers" recorded per PS cycle and the corresponding optimum beam intensities as a function of trigger level.

Finally Figs. 2.4.11 to 2.4.14 show the estimate of the number of events to be analysed per year as a function of the trigger level.

The parameters used in Figs. 2.4.3 to 2.4.14 are summarized in the following table

Figure No.	Dead-time	Wanted beam particles	Beam pulse
2.4.3, 7, 11	0.01 sec	100%	0.2 sec
2.4.4, 8, 12	0.05 sec	100%	0.2 sec
2.4.5, 9, 13	0.01 sec 0.05 sec	1%	0.2 sec
2.4.6, 10, 14	0.05 sec	100%	0.5 sec

The results displayed in Figs. 2.4.11 to 2.4.14 occasion the following remarks.

a) There are two main sources of large variations on the rate of recorded triggers to be measured: the trigger level and the percentage of wanted beam particles. They in fact produce, separately, changes of the trigger rate by 10 to 100 times as the trigger level goes from 10^{-4} to 10^{-6} and the percentages of wanted beam particles from 10 to 100%. Furthermore they both depend on the type of experiment. Therefore it is difficult to make very definite predictions on the amount of triggers to be analysed per year. As an example, in the case of the optical spark chamber operation one can estimate an average of 4×10^6 useful triggers to be analysed per year for a trigger level of 10^{-5} [i.e. 10 μbarn cross-section for 25 cm of liquid H_2 target and 100% detection efficiency or 1000 μbarns cross-section and 10^{-2} detection efficiency.].

b) There is a number of sources of improvements which can be obtained in the triggering rate, namely:

Beam pulse: an improvement of a factor of ~ 2 can be obtained going from 0.2 to 0.5 sec.

Beam halo: same improvement as for beam pulse going from 100% to 0% beam halo.

Dead-time: an improvement of a factor of 1.5 to 3.5 can be obtained as the dead-time goes from 0.05 to 0.01 sec.

Protection of spark chamber plates (in the region traversed by the beam): again a factor of ~ 2 improvement can be obtained with respect to the case of unprotected plates.

c) The intensities which are required will be available for the designed beams as is shown in Fig. 2.4.15.

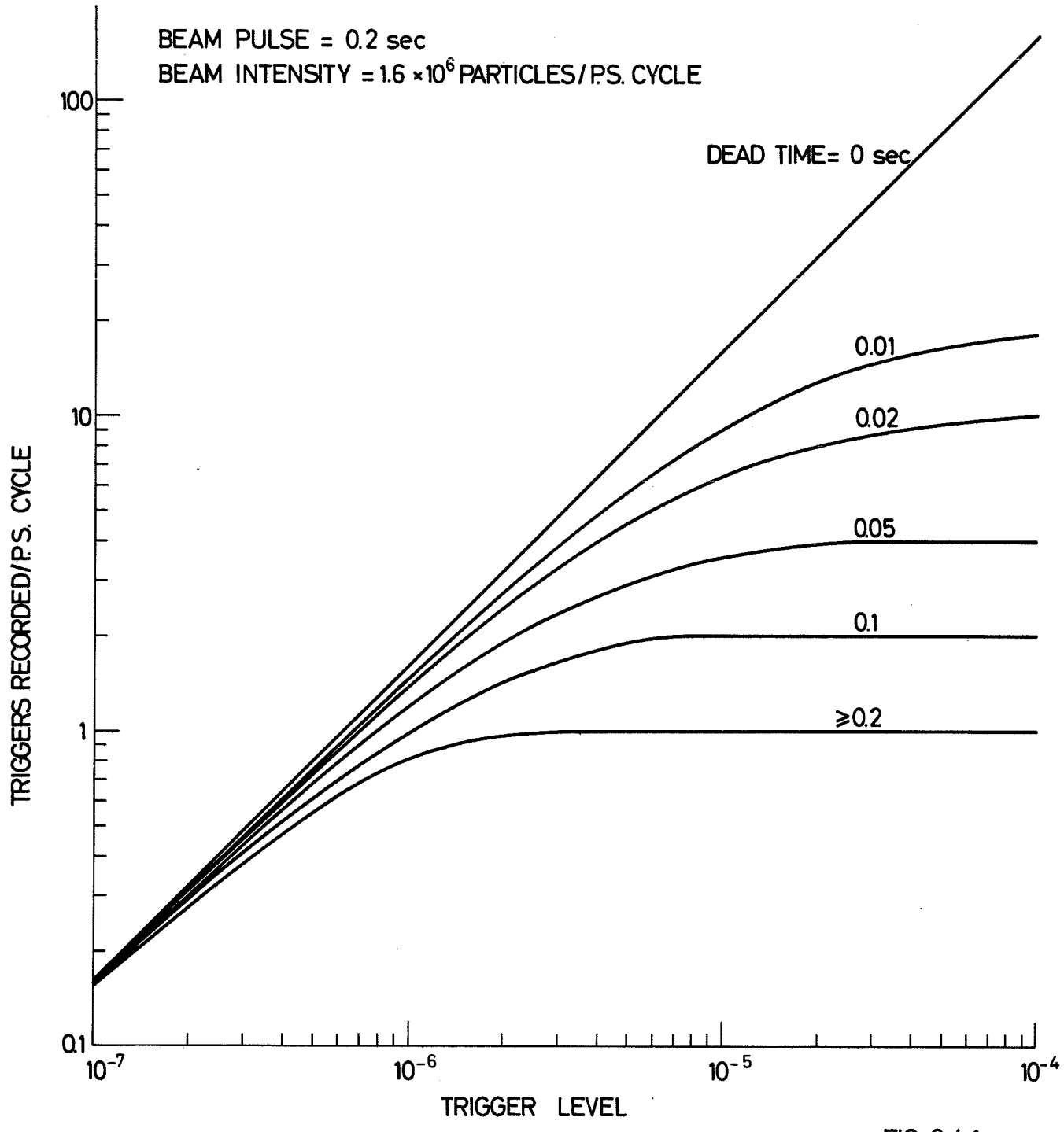
BEAM PULSE = 0.2 sec
BEAM INTENSITY = 1.6 ×10^6 PARTICLES/P.S. CYCLE
DEAD TIME= 0 sec
0.01
0.02
0.05
0.1
≥0.2
100
10
1
0.1
TRIGGERS RECORDED/P.S. CYCLE
10^-7
10^-6
10^-5
10^-4
TRIGGER LEVEL

FIG. 2.4.1

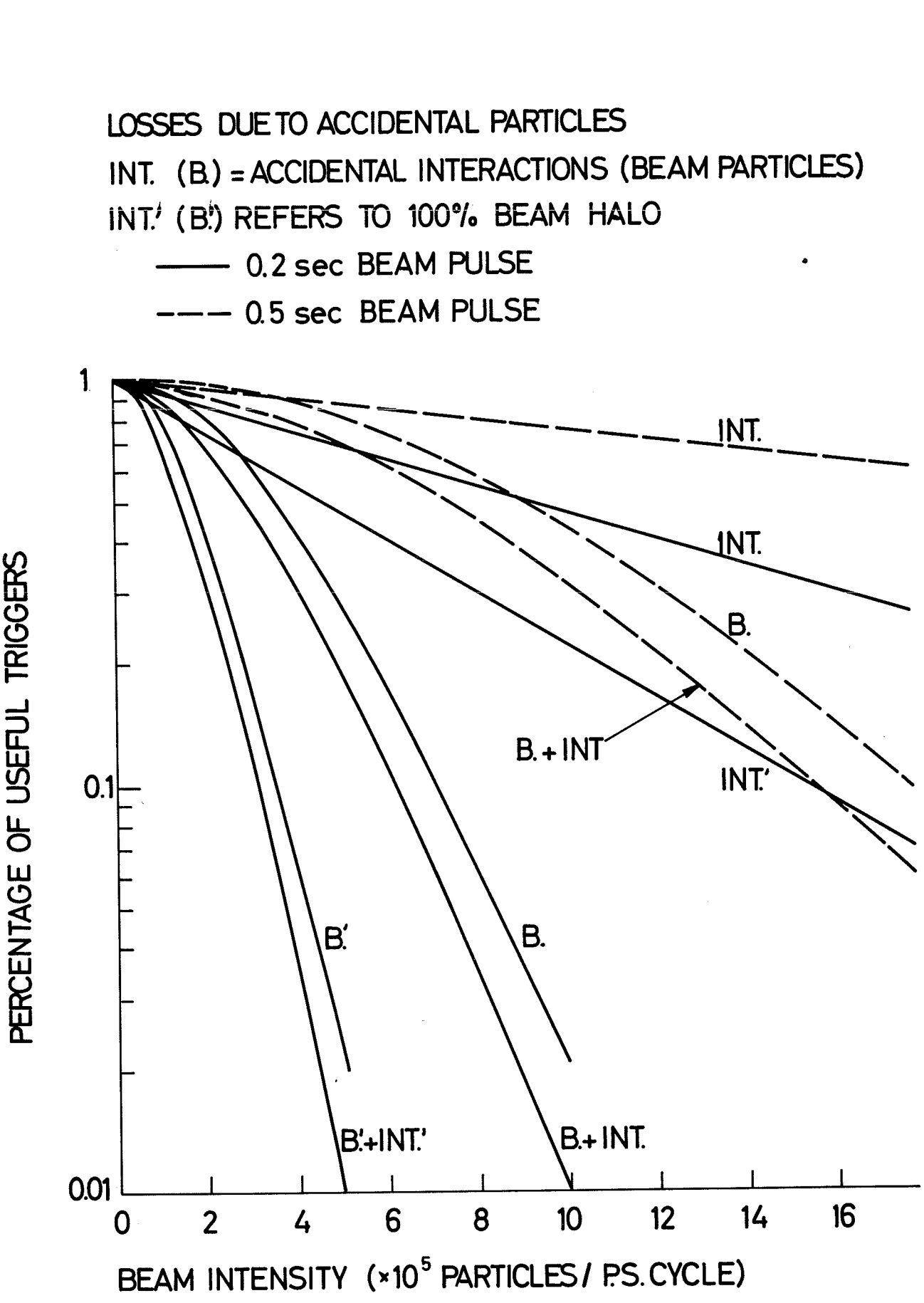
LOSSES DUE TO ACCIDENTAL PARTICLES
INT. (B.) = ACCIDENTAL INTERACTIONS (BEAM PARTICLES)
INT.' (B.') REFERS TO 100% BEAM HALO
—— 0.2 sec BEAM PULSE
---- 0.5 sec BEAM PULSE
PERCENTAGE OF USEFUL TRIGGERS
1
0.1
0.01
INT.
INT.
B.
B. + INT
INT.'
B.'
B.
B.'+INT.'
B.+ INT.
0
2
4
6
8
10
12
14
16
BEAM INTENSITY (×10⁵ PARTICLES / P.S. CYCLE)

FIG. 2.4.2

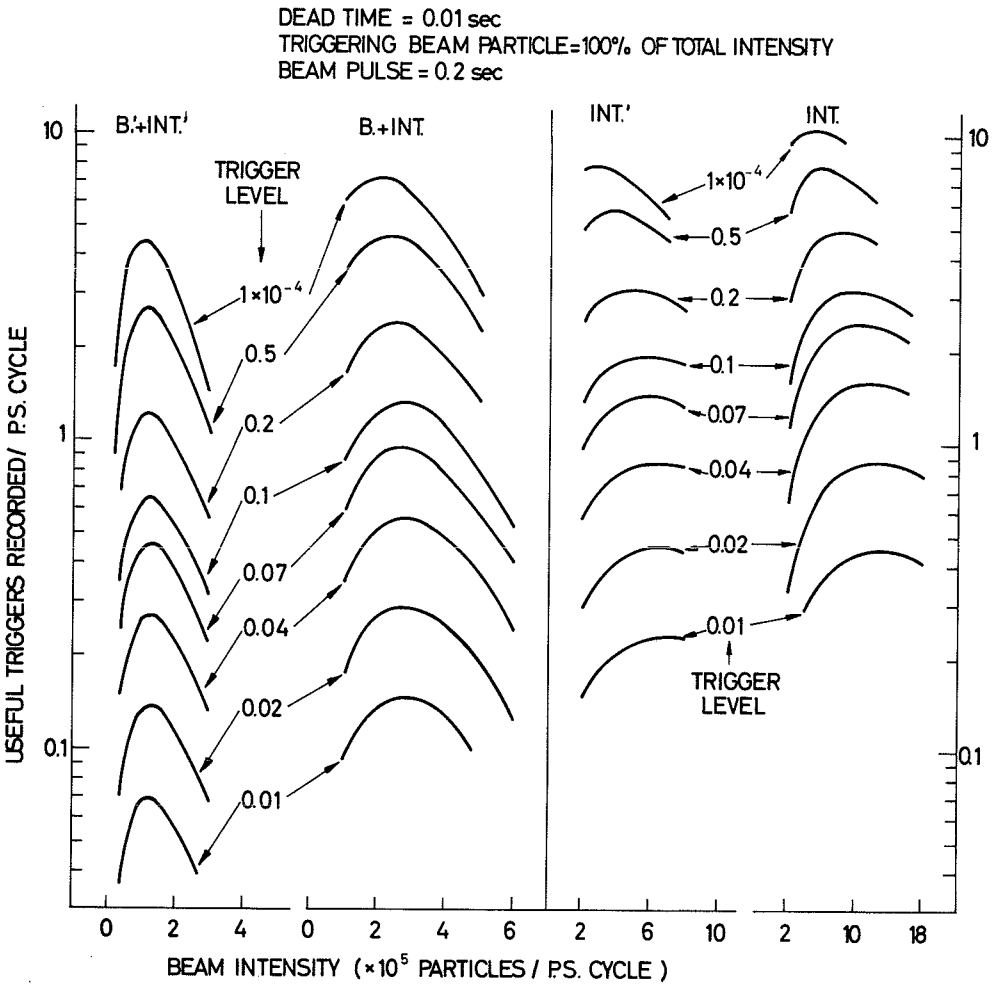

FIG. 2.4.3

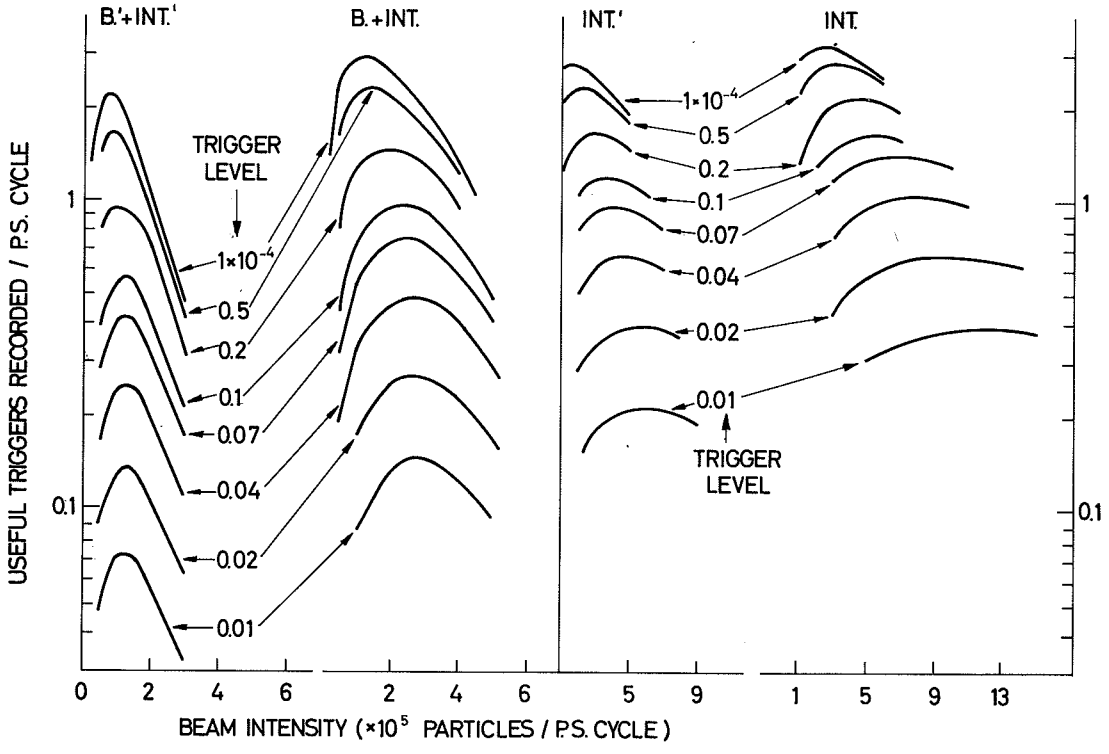

FIG. 2.4.4

DEAD TIME = 0.01sec —— AND 0.05 sec – – –

TRIGGERING BEAM PARTICLE = 1% OF TOTAL INTENSITY

BEAM PULSE = 0.2 sec

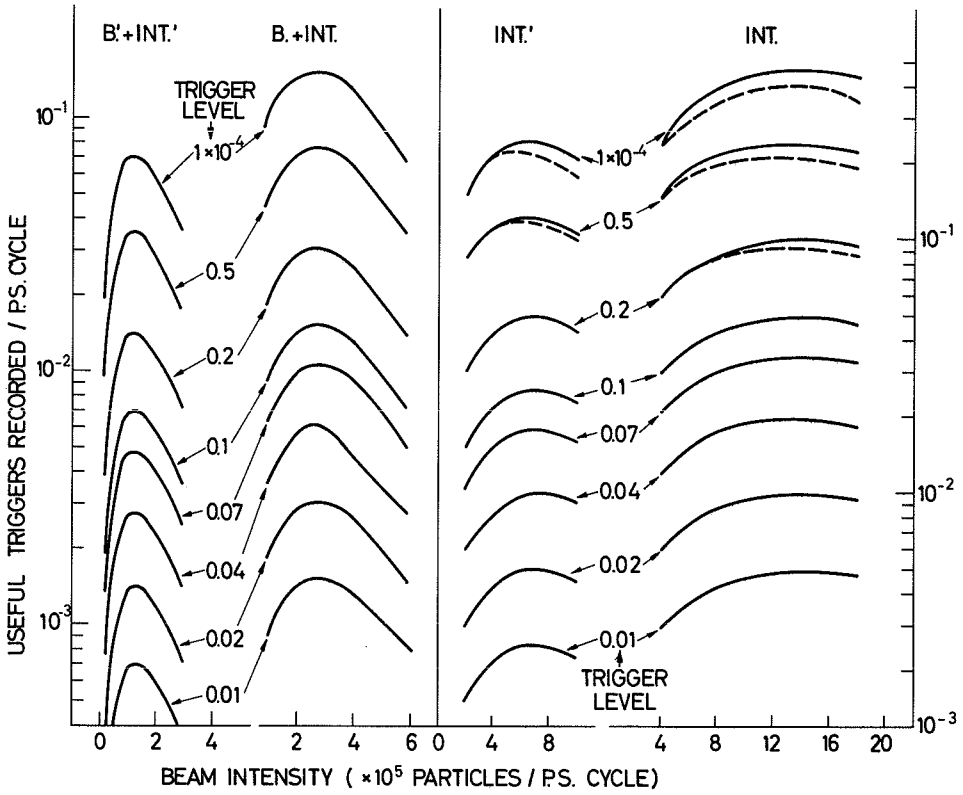

FIG.2.4.5

DEAD TIME = 0.05 sec

TRIGGERING BEAM PARTICLE = 100% OF TOTAL INTENSITY

BEAM PULSE = 0.5 sec

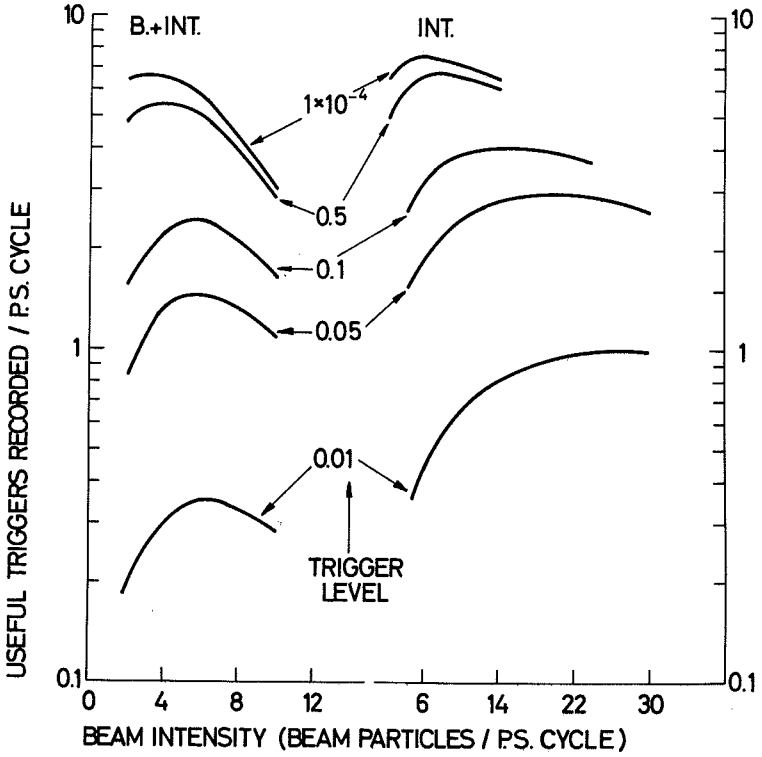

FIG. 2.4.6

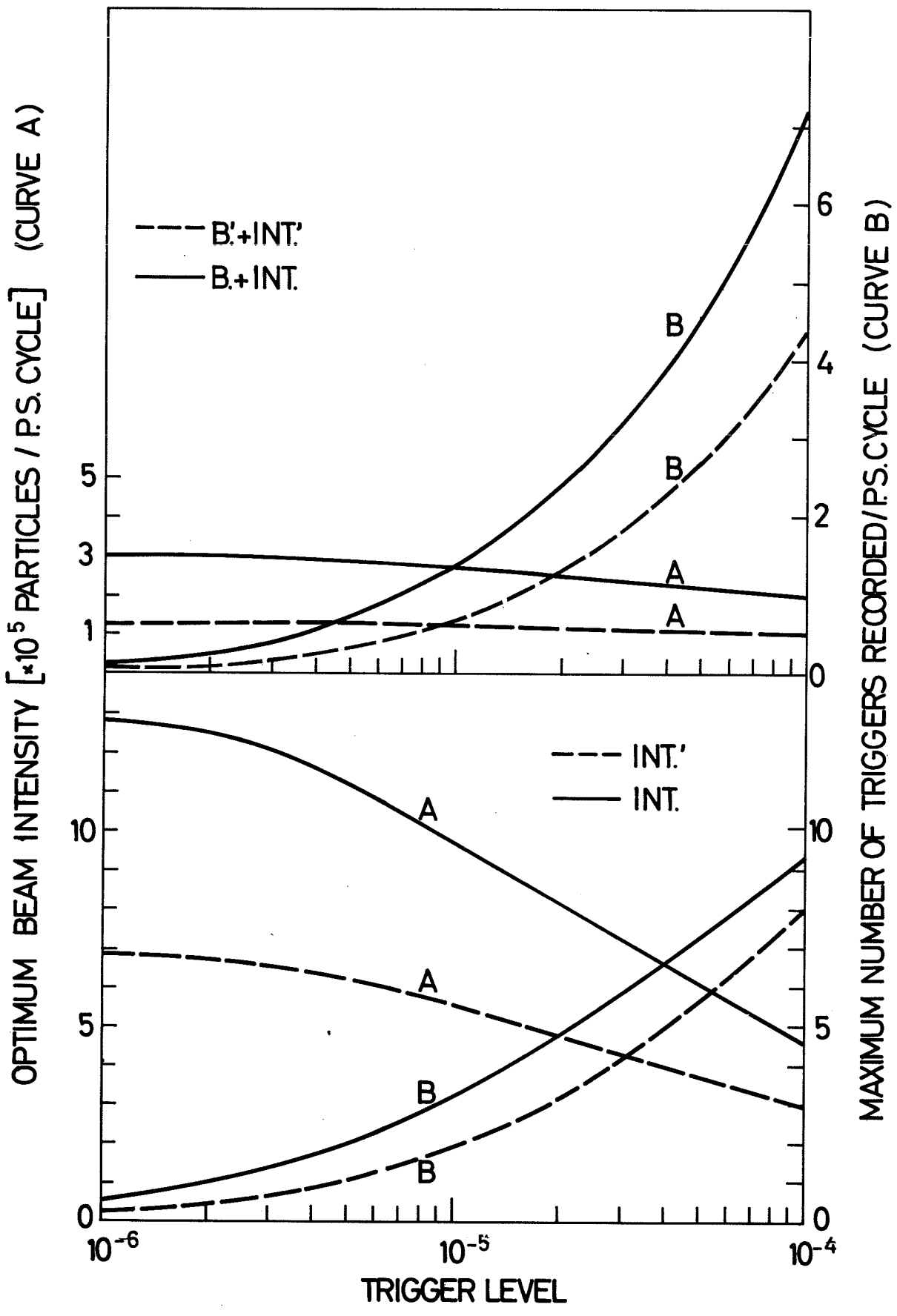
DEAD TIME = 0.01 sec
TRIGGERING BEAM PARTICLE = 100%
BEAM PULSE = 0.2 sec
B'+INT.'
B.+INT.
INT.'
INT.
A
B
OPTIMUM BEAM INTENSITY [×10⁵ PARTICLES / P.S. CYCLE] (CURVE A)
MAXIMUM NUMBER OF TRIGGERS RECORDED/P.S.CYCLE (CURVE B)
TRIGGER LEVEL
10⁻⁶
10⁻⁵
10⁻⁴
0
1
3
5
2
4
6
10

FIG. 2.4.7

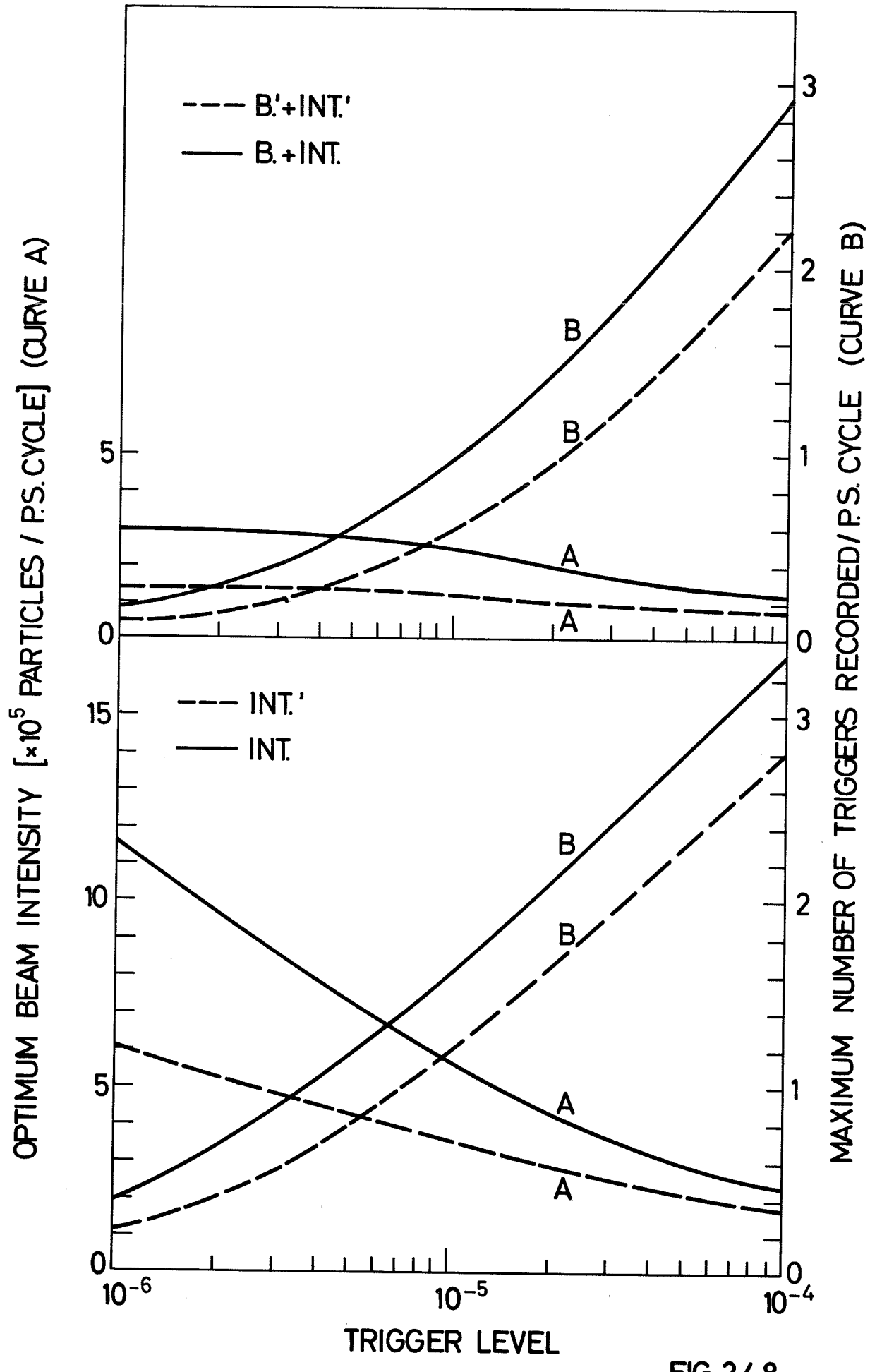
DEAD TIME = 0.05 sec
TRIGGERING BEAM PARTICLE = 100%
BEAM PULSE = 0.2 sec
B'+INT.'
B.+INT.
INT.'
INT.
B
B
A
A
OPTIMUM BEAM INTENSITY [×10^5 PARTICLES / P.S. CYCLE] (CURVE A)
MAXIMUM NUMBER OF TRIGGERS RECORDED / P.S. CYCLE (CURVE B)
TRIGGER LEVEL
10^-6
10^-5
10^-4
0
5
10
15
1
2
3

FIG. 2.4.8

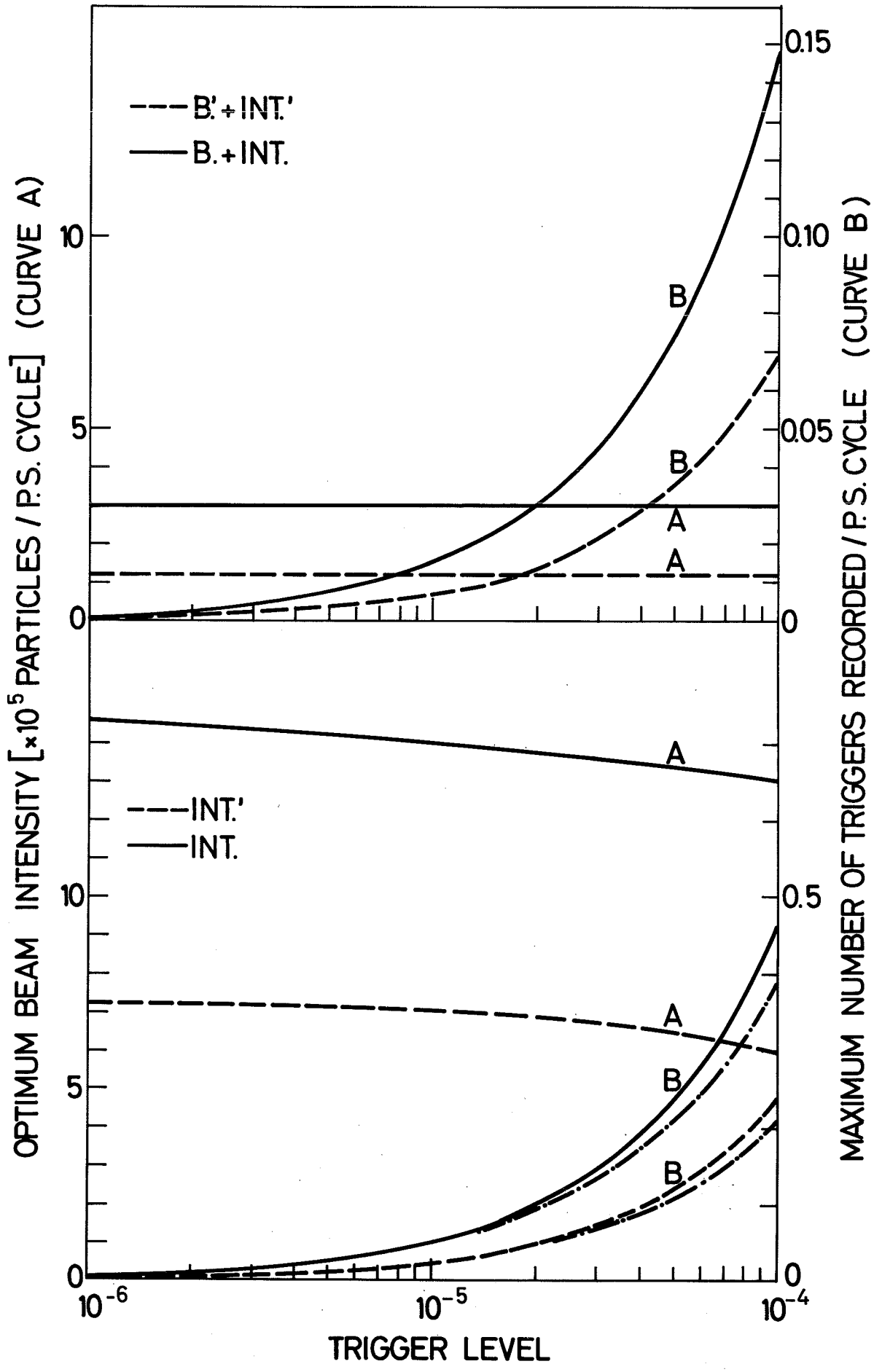
DEAD TIME = 0.01 sec —— and 0.05 sec —·—·—
TRIGGERING BEAM PARTICLE = 1%
BEAM PULSE = 0.2 sec
B'+INT.'
B.+INT.
INT.'
INT.
A
B
OPTIMUM BEAM INTENSITY [×10^5 PARTICLES / P.S. CYCLE] (CURVE A)
MAXIMUM NUMBER OF TRIGGERS RECORDED / P.S. CYCLE (CURVE B)
TRIGGER LEVEL
10^-6
10^-5
10^-4
0
5
10
0.05
0.10
0.15
0.5

FIG. 2.4.9

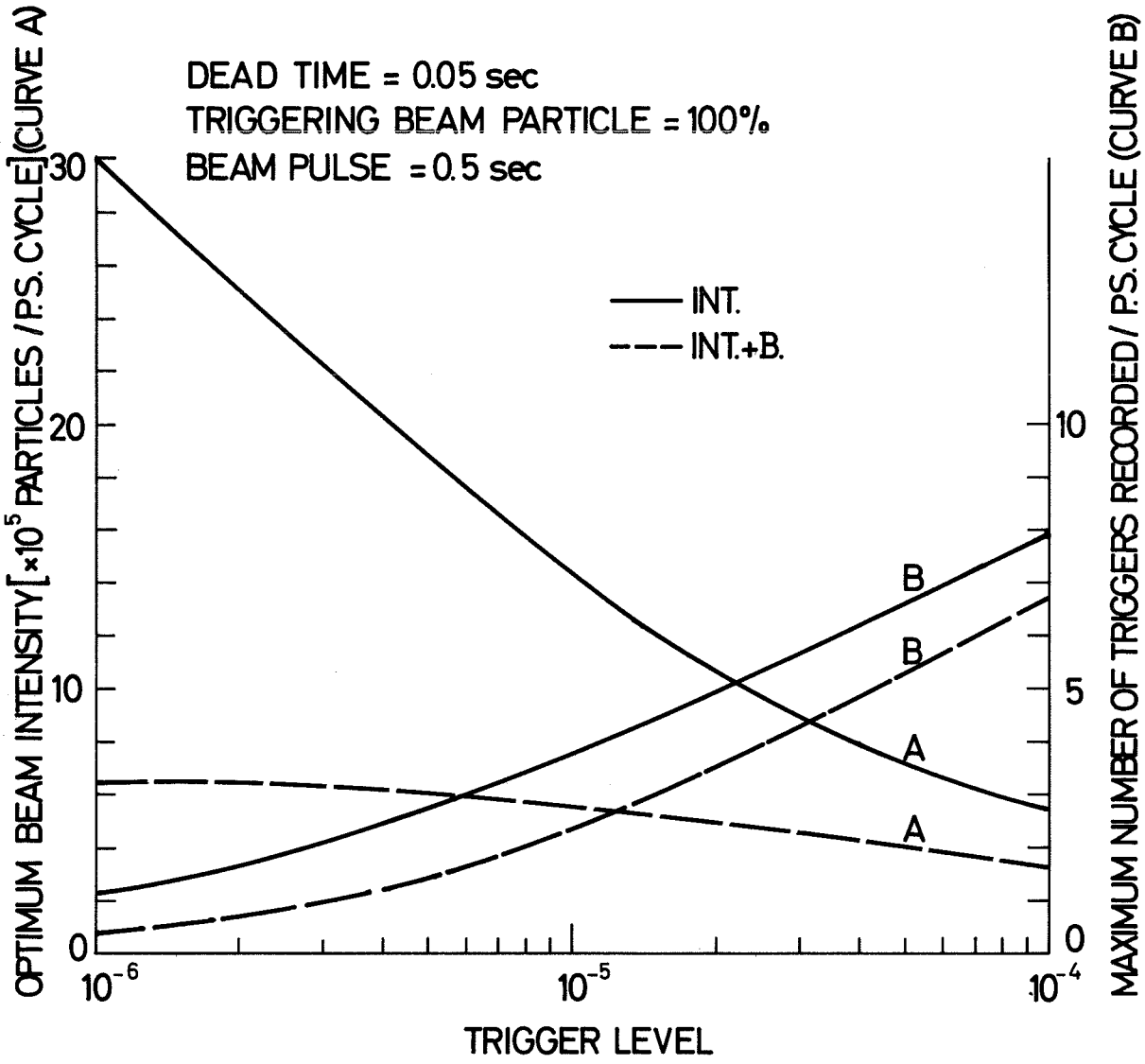
DEAD TIME = 0.05 sec
TRIGGERING BEAM PARTICLE = 100%
BEAM PULSE = 0.5 sec
INT.
INT.+B.
OPTIMUM BEAM INTENSITY [×10^5 PARTICLES / P.S. CYCLE] (CURVE A)
MAXIMUM NUMBER OF TRIGGERS RECORDED / P.S. CYCLE (CURVE B)
30
20
10
0
10
5
0
B
B
A
A
10^-6
10^-5
10^-4
TRIGGER LEVEL

FIG. 2.4.10

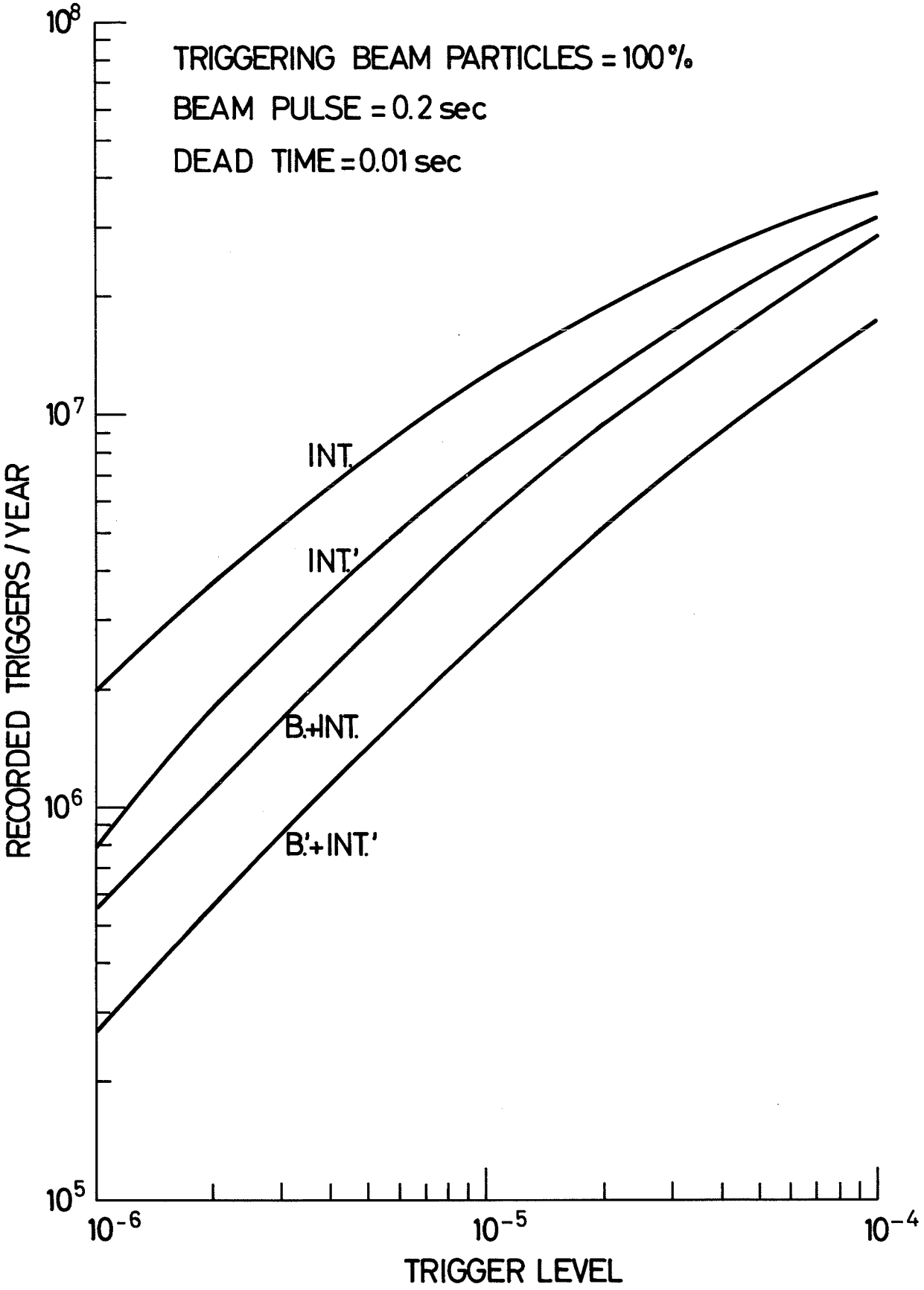
TRIGGERING BEAM PARTICLES = 100%
BEAM PULSE = 0.2 sec
DEAD TIME = 0.01 sec
INT.
INT.'
B.+INT.
B.'+INT.'
RECORDED TRIGGERS / YEAR
10^8
10^7
10^6
10^5
10^{-6}
10^{-5}
10^{-4}
TRIGGER LEVEL

FIG. 2.4.11

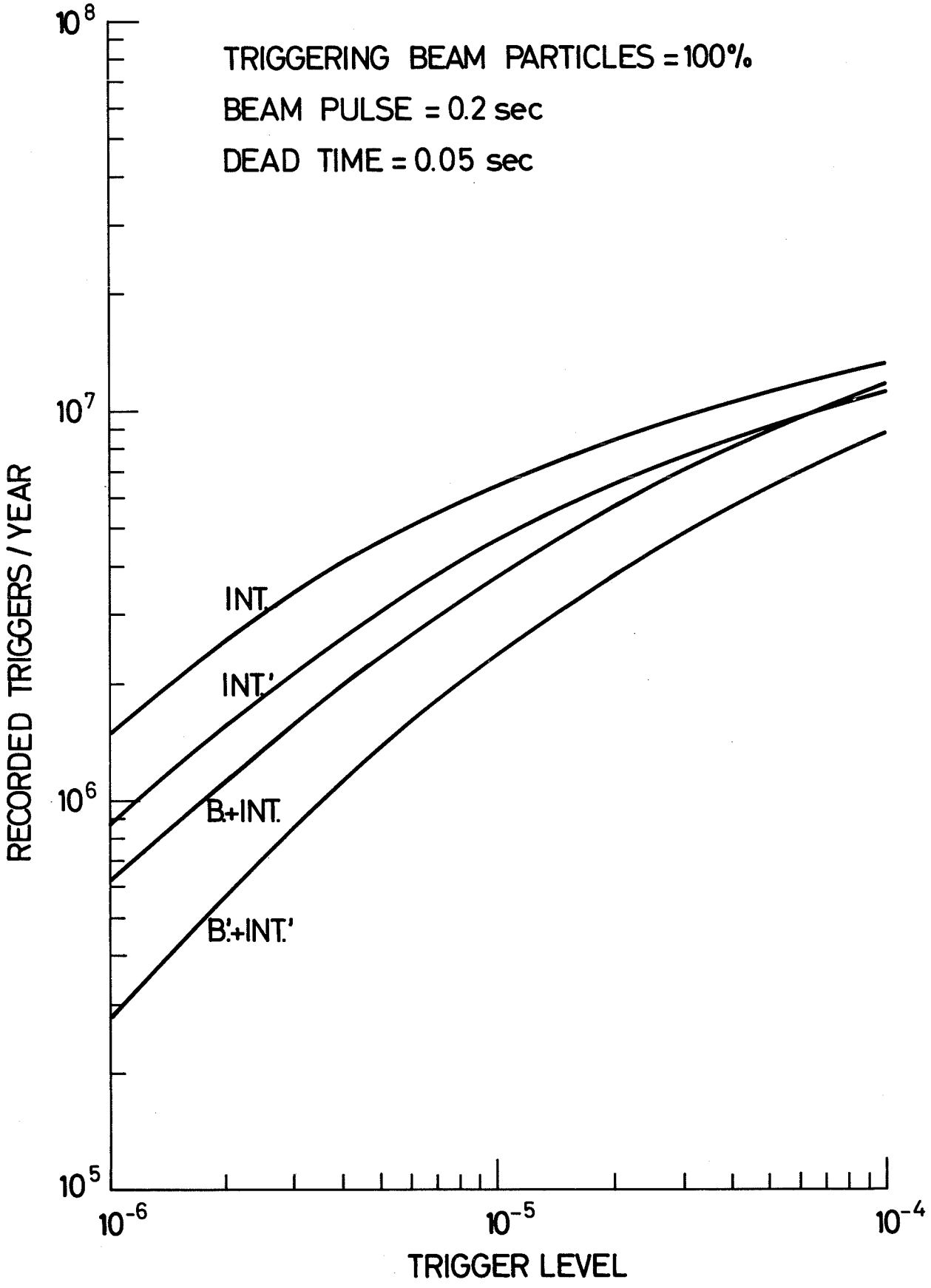
TRIGGERING BEAM PARTICLES = 100%
BEAM PULSE = 0.2 sec
DEAD TIME = 0.05 sec
RECORDED TRIGGERS / YEAR
10^8
10^7
10^6
10^5
INT.
INT.'
B.+INT.
B.'+INT.'
10^{-6}
10^{-5}
10^{-4}
TRIGGER LEVEL

FIG. 2.4.12

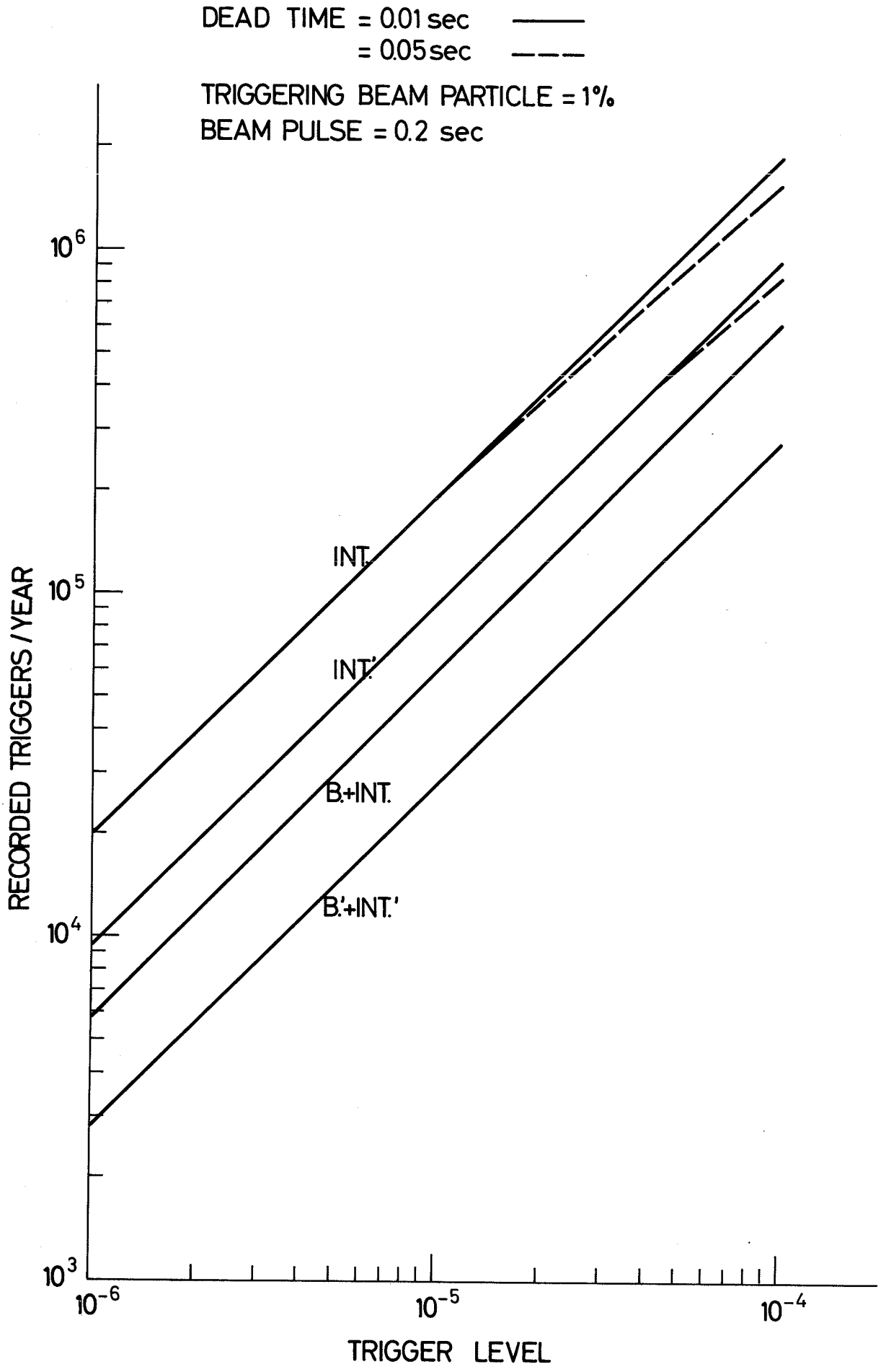
DEAD TIME = 0.01 sec
= 0.05 sec
TRIGGERING BEAM PARTICLE = 1%
BEAM PULSE = 0.2 sec
RECORDED TRIGGERS / YEAR
10^6
10^5
10^4
10^3
INT.
INT.'
B.+INT.
B.'+INT.'
10^{-6}
10^{-5}
10^{-4}
TRIGGER LEVEL

FIG. 2.4.13

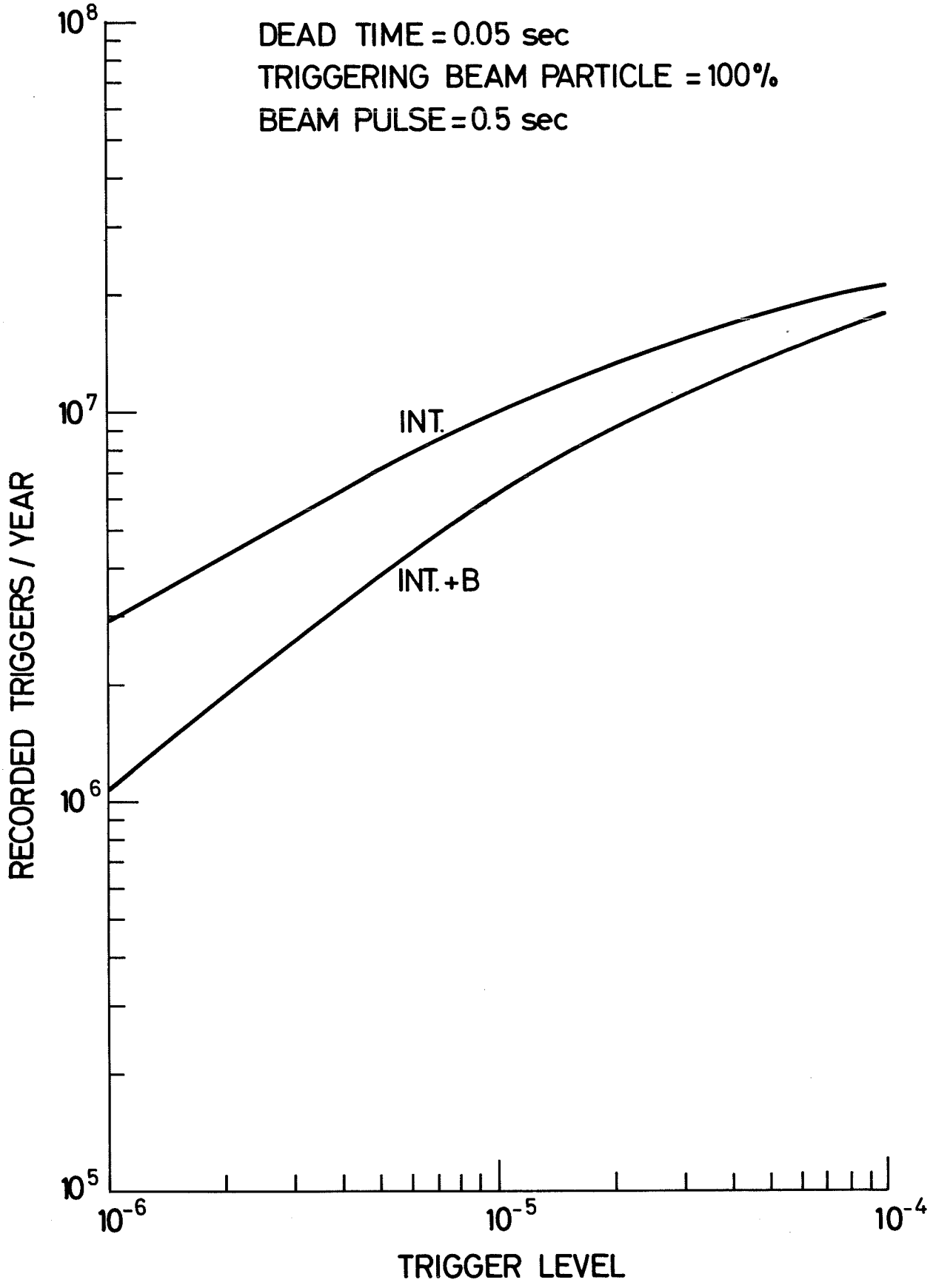
DEAD TIME = 0.05 sec
TRIGGERING BEAM PARTICLE = 100%
BEAM PULSE = 0.5 sec
INT.
INT.+B
RECORDED TRIGGERS / YEAR
TRIGGER LEVEL
10^8
10^7
10^6
10^5
10^{-6}
10^{-5}
10^{-4}

FIG. 2.4.14

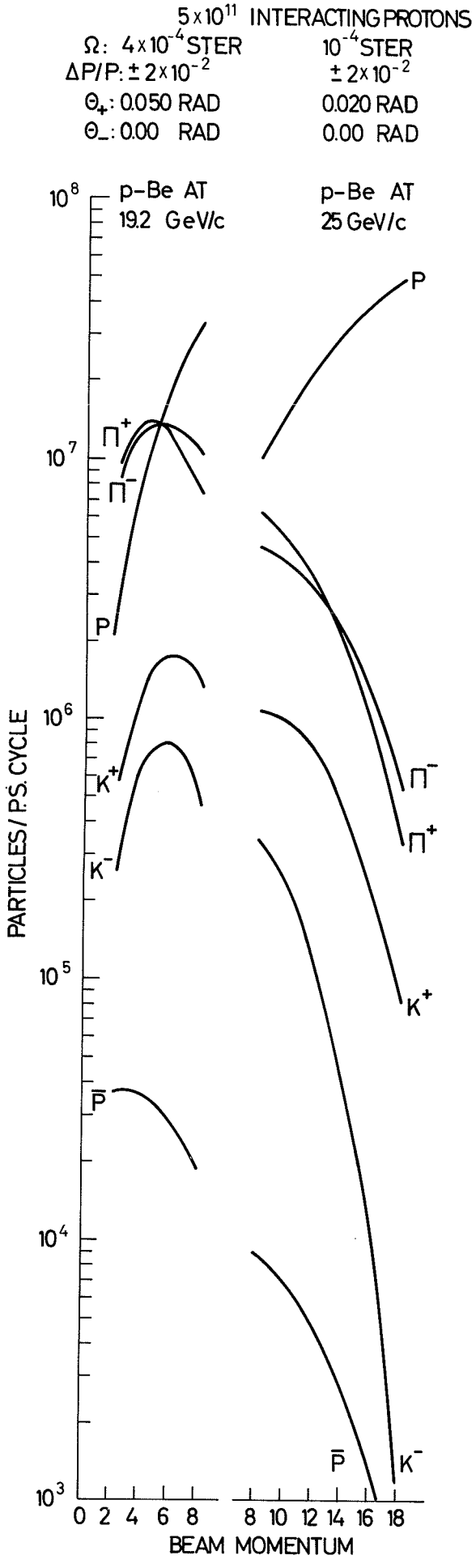
5 x 10^11 INTERACTING PROTONS
Ω: 4 x 10^-4 STER
ΔP/P: ± 2 x 10^-2
Θ+: 0.050 RAD
Θ−: 0.00 RAD
10^-4 STER
± 2 x 10^-2
0.020 RAD
0.00 RAD
p-Be AT 19.2 GeV/c
p-Be AT 25 GeV/c
PARTICLES / P.S. CYCLE
BEAM MOMENTUM
P
Π+
Π−
K+
K−
P̄
0 2 4 6 8
8 10 12 14 16 18

FIG. 2.4.15

2.5 Data-handling facilities

The proposed data-handling system for the Omega project is based on the following conditions:

i) photographic read-out of the spark chambers;

ii) computer control of the experimental equipment and on-line recording of some information (such as triggering conditions, times-of-flight, beam flux, counter efficiencies, etc.);

iii) full analysis at CERN of a fraction of the recorded data (say 30%).

The essential components of the system are an HPD flying-spot digitizer, a digital computer and the CERN central computing facilities.

After consideration of several possible configurations, we arrived at this system as an economical fulfilment of the above conditions consistent with adaptability to a possible future utilization of filmless techniques.

2.5.1 Description of the system

Both the computer and the HPD are located in the Omega area. This will permit the most efficient use to be made of the computer, sharing it among the various tasks:

i) HPD operation;

ii) control of experimental equipment;

iii) on-line recording of information;

iv) visual recovery with a CRT display and light-pen of events not recognized by the pattern recognition programs.

The HPD plus computer combination will produce spark coordinates of recognized events on magnetic tapes, which are then taken to the CERN central computing facilities for final analysis.

Figure 2.5.1 is a schematic diagram of the system proposed. Each of the three applications, HPD, CRT, and on-line recording and control, are coupled to the computer via a buffer or small computer. All three make use of the power of the main computer, but whereas the HPD and CRT require the main computer for operation, the on-line data recording and control application can,

if necessary, operate independently. This latter mode of operation is designed as a safety feature that permits the "Omega" to record data even if the main computer is out of operation.

2.5.2 Main computer configuration

The basic features are:

1) Core memory size 64 K
2) Word length 32 bits (should be a multiple of 16 bits)
3) Memory cycle time ≈ 1 μsec or less
4) Floating point hardware
5) Priority interrupt system
6) Card reader/punch (say ~ 400 cpm/150 cpm)*)
7) Line printer (say ~ 250 lpm)*)
8) 4 or 5 magnetic tape units (say ½", 7-9 tracks, 800 bpi, 60 kc)*)
9) Typewriter on-line
10) CRT + LP display with controller
11) Backing store (disk driver for monitor, program overlays and data)
12) A buffered 32-bit I/O channel for the HPD
13) Memory protection
14) Auxiliary card-handling equipment
15) Software (FORTRAN compiler, assembler, operating system).

The total cost of such a configuration is estimated to be about 5 million Swiss francs. As this computer is to be located near experimental equipment, and as it will possibly be on-line to this equipment, it should be capable of operation under varying environmental conditions and should be highly reliable in its operation. A fundamental condition of its speed of calculation is that it should match (with some margin) the speed of the HPD.

---

*) Peripherals should be rented due to rapidly changing compatibility conditions.

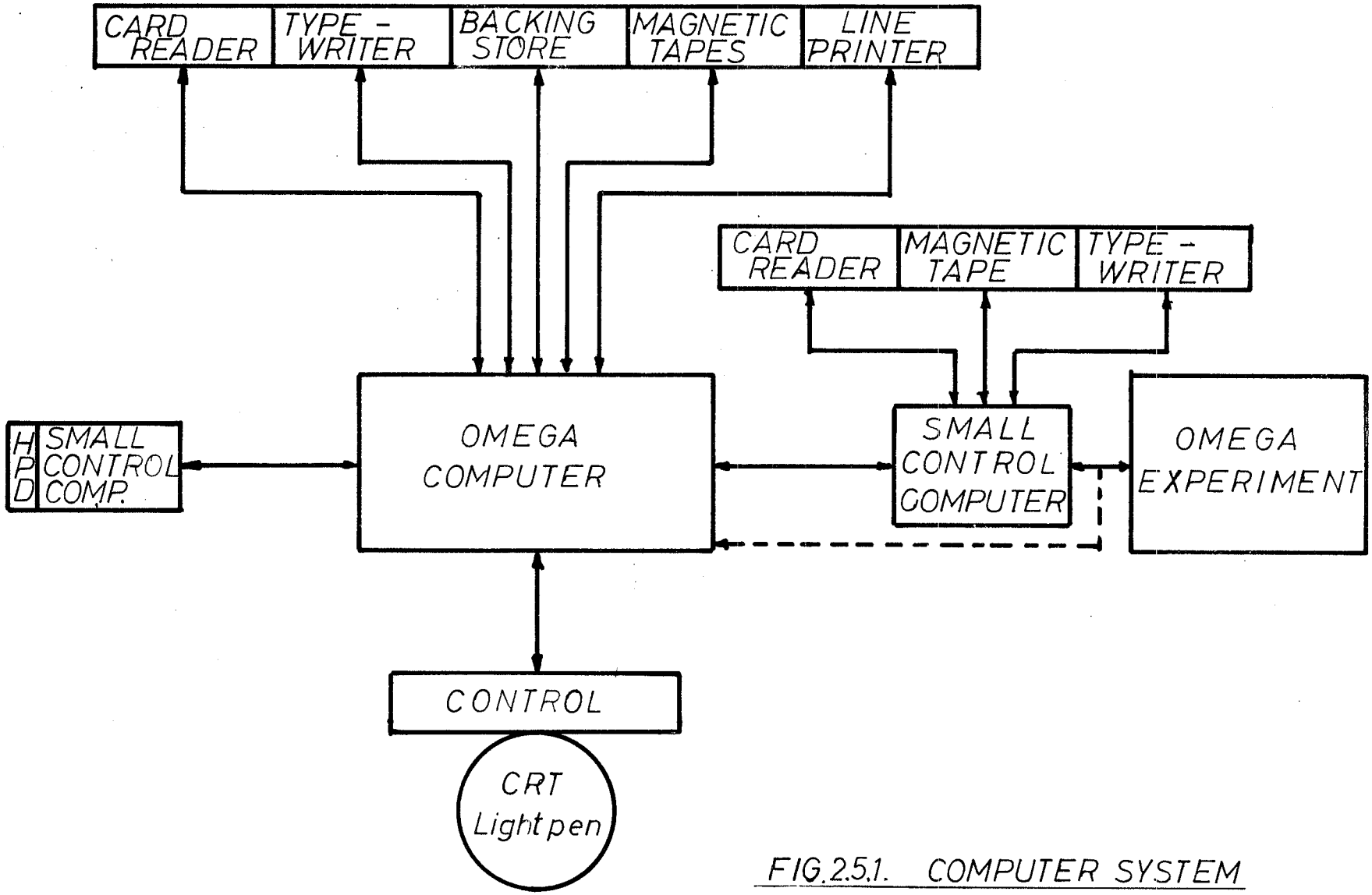

FIG.2.5.1. COMPUTER SYSTEM

2.5.3 HPD characteristics

A typical picture as described in Section 2.2.1 is assumed, i.e. 70 mm film, 70 × 60 mm^2 frame, all the gaps oriented in one direction across the film, two views side by side, each approximately 30 × 60 mm^2.

The geometry of the chambers can be slightly different from the above proposed solution, i.e. spark dimensions on the film not smaller than 40 × 190 μm^2. Otherwise the time estimates which follow must be scaled accordingly.

The characteristics of the HPD should be 70 mm scan length and a 2 μm least count in both x and y leading to a 16-bit coordinate. (Width measure optional.) Pitch would be reasonably set at about 60 μm to guarantee three crossings per spark, and the whole frame would be scanned by a 1000-line raster. The resolution of the device, defined as the ability to measure two distinct sparks lying very close together, would be limited to 45 μm (distance between spark centres).

The HPD rotating disk would be designed for 6000 rpm, but the estimates of the measurement times given below are based on the more conservative speed of 3000 rpm at which HPD-2 is now operated at CERN. Scan-line time is 2.5 msec, hence 1000 lines $\simeq$ 2.5 sec. The overheads (film advance, stage setting, etc.) are $\simeq$ 2.5 sec. The time per picture is therefore estimated at 5 sec. This means about 720 frames/hour or some 15,000 frames a day as a maximum.

If one takes into account film changes, tests, operator interventions, breakdowns, and all other contributions to inefficiency, only about 60-70% of this maximum rate can be maintained over long production periods, i.e. a rate of about 10,000 such frames a day could be achieved in the steady production stage. Hence, one would expect to measure 2-3 million frames/year, which would yield approximately 1000 magnetic tapes.

This, of course, implies that the computer can do its job on the digitized data during the 5 seconds taken by the HPD to scan one frame. This will influence the choice of the computer. It is worth mentioning that the task of the computer is rather well defined; that FORTRAN programs, similar to those which will be used at the Omega, exist and will have to be run on the various candidate computers to give a fair indication of their capabilities.

The HPD hardware is partly commercially available (mechanical and optical parts). A very small computer would be substituted for a substantial part of the electronics involved, and would constitute a flexible and reliable interface. The total cost of the HPD hardware is estimated at 0.8 million Swiss francs. Its construction will involve some 18 man-years and could be achieved in a period of about two years.

2.5.4 Visual recovery application

A human operator will view on a CRT display the events that are not recognized by the computer programs. With the aid of a light-pen and typewriter, the operator can supply some guidance to the programs in order to complete the pattern recognition. This application will use 5,000-10,000 words of central memory, some disk space, and one or two tape units, when it is in operation. Moreover, it will have access to the pattern recognition program sitting in core. The image on the CRT is maintained by the private memory of the CRT controller; the light-pen activity is relatively slow because of human response time, and the transfer of information from tape or disk storage to CRT is comparatively infrequent. Therefore the load placed on the processing unit of the main computer should be relatively small for this application.

2.5.5 Recording and control application

This mode permits the recording on tape of subsidiary data during the running of the experiment at the PS; it can also perform monitoring and control functions of the experimental equipment. It will operate through its own small computer and will also have at its disposal the main computer with its peripherals, such as the CRT, disk and line-printer. As this part of the system is absolutely necessary during a run, the small computer will be capable of operating alone, and for this reason it is equipped with its own tape unit, card reader, and typewriter. Conversely, in case the small computer is inoperative, this mode could operate directly into the main computer.

When optical chambers are being used one would record such information as scaler readings, triggering conditions, magnet settings, Čerenkov counter pressures, and times-of-flight. With wire chambers, this computer would, in addition, serve as the input buffer for the main computer. Its core memory would store up the spark coordinates of events during one PS burst, and pass them on to the main computer for recording, monitoring, and some analysis between bursts.

As the function of this small computer is mainly to buffer and record information it need not have floating point hardware, although it should have a FORTRAN compiler and operating system for monitor and control duties. The specifications for this computer are as follows:

1) Core memory size 16 K (expandable to 32 K)

2) Word length 16 bits (or multiple thereof)

3) Memory cycle time 1 - 2 μsec

4) Priority interrupt system

5) Card reader/punch

6) 1 - 2 tape units

7) Typewriter on-line

8) Software (FORTRAN compiler, assembler, and operating system).

This configuration is estimated to cost 0.6 to 0.8 million Swiss francs.

2.5.6 Organization of the programs

2.5.6-1 Allocation of storage. The HPD measurement of a typical Omega picture should produce about 10,000-15,000 digitizings. These data will be transmitted from the HPD internal buffer to an area in the core storage of the main computer via a 32-bit I/O channel; the transmission will be controlled by the interrupt system.

Two programs will be in core memory for the analysis of the HPD measurements: i) "Stage 1" program will carry out the control of the HPD, the acquisition of the data from it, the reduction of these data into spark and fiducial coordinates; ii) "Stage 2" program will perform the automatic recognition of tracks and the identification of events. Each of these two programs

would require the allocation of some 20-25,000 words. The remaining memory space will be devoted to the recovery program (CRT display) or the Omega on-line control application, whichever is carried out in parallel with the HPD operation. Special programs, such as HPD tests, calibrations, data management, etc., will have to be called into memory from overlays on disks, when required.

2.5.6-2 Use of the central processor. The priority interrupt system and some form of memory protection will enable the computer to execute two jobs in the foreground (i.e. the HPD "Stage 1" program and the light-penning) and one job in the background (i.e. the "Stage 2" pattern recognition program).

As a minimum requirement, the computer should be able to execute the "Stage 1" program simultaneously with the HPD measurement and without using all the CPU time available. "Stage 2" program will then be run asynchronously with the HPD activity, and will absorb the CPU time not utilized by "Stage 1". "Stage 2" program would be available in core both to the HPD and CRT inputs.

2.5.6-3 General operation of the system for photographic analysis. The system is loaded with films which might or might not be prescanned (depending on the experiment), and produces magnetic tapes containing the measurements of tracks of recognized events.

The recognition of the events is achieved in two stages. First the HPD output is reduced to spark coordinates; then spark patterns are identified as valid events.

The first stage is automatic. The second stage is also attempted in an automatic way (except for some guidance obtained at prescanning level), but in case of failure the spark information concerned is stored away until more guidance is obtained via the CRT-display. The events to be rescued should be presented only once to the CRT-operator, who by interacting with the "Stage 2" program, will provide the necessary guidance until the event is accepted.

One can see the advantages of having the pattern recognition programs and the CRT-recovery activity run on the same computer. Certainly the CRT-operator will work more efficiently, and the necessity of intermediate output on tapes to be processed elsewhere will be avoided. In this mode of operation, the processed information will leave the Omega system only when ready for "Stage 3" analysis programs, i.e. geometry, kinematics, statistics.

2.5.7 Load on the central computing facilities

Supposing the Omega project to be running 100 days/year yielding 2.4 million useful PS bursts, we would obtain 7-8 million photographs/year at an average of 3 photographs/burst. Of these, 2-3 million frames/year would be measured on the Omega-HPD, as stated previously. Assuming 2 sec/event of 6600 CPU time for stage 3 analysis, the resultant load would be 1500 hours/year or one-fourth of a 6600. The remaining fraction of the photographs has to be measured and analysed outside CERN.

2.5.8 Alternative data-handling system using central computing facilities at all stages

An alternative solution is to perform all analyses (except, of course, for recording and experiment control functions) at the CERN central computing facilities.

With this solution and in the case of optical spark chambers, the HPD measurements, the CRT recovery procedures, and all stages of data reduction would be performed at the central facilities. The equivalent of one HPD per year would be required, and 3000 hours of 6600 CPU time per year (or ½ a 6600) for the complete analysis of 2-3 million photographs per year.

A small computer will still be required for on-line recording and control functions. This should be an expandable machine with more powerful peripherals than the small on-line computer described in the first solution. For example, it should be equipped with two tape units, line printer, card read/punch, and typewriter. It should be an expandable machine having a 32-bit word length, and it should also have multi-level interrupt features. A memory of 8 K would be sufficient for optical chambers. A FORTRAN compiler is still necessary. We estimate that such a computer would cost from 1 to 1½ million Swiss francs.

In the case of wire spark chambers, the on-line computer should be expanded to at least 32 K of memory, a disk and more and faster tape units added, and a data-link to the central computer facility. The equivalent of a 6600 CPU should be available at all times on the link while the experiment is running.

2,6 Cost estimate

The estimates are based on interpolations or extrapolations of the costs of existing systems, and thus are not extremely accurate. They are based on present (1967) prices. No provision is made for contingencies. (The data handling system has been estimated separately.)

Experimental part:

Magnet incl. supplies	MSFr.	9.5
Instrumentation		1.7
Staff		2.5
	Total MSFr.	13.7

Data-handling system (First version): MSFr. 8.2

a) Experimental part

Magnet with superconducting coils:

Iron yoke (1300 t at 2.5 SFr./kg)	MSFr.	3.25
Superconducting stabilized cable		1.0
Coil winding, insulation, tools		0.5
Helium container, vacuum tank, supports		0.6
Superinsulations		0.3
Vacuum pumps, valves, pipes, etc.		0.5
Power supply and controls		0.4
Refrigerator (500 W)		1.4
Liquid-helium container (2000 ℓ)		0.15
Gas-helium storage (2000 m^3)		0.15
Helium		0.1
Foundation		0.5
Measurement gear		0.25
Cryogenic tests		0.4
	Total MSFr.	9.5

Magnet with conventional coils:

Iron yoke	MSFr.	3.25
Copper coil (75 t)		1.9
Power supply		1.3
Cooling towers		0.7
Cables, piping, etc.		0.5
Foundations		0.5
Measurement gear		0.15
	Total MSFr.	8.3

Instrumentation:

Spark chambers (100 frames)			
Material	MSFr. 0.1	MSFr.	0.4
Labour	0.3		
Prisms, supporting glass plate			0.15
Camera, lenses, mirrors, supports			0.2
Electronics, pulse system			0.2
Film-developing machine			0.3
Accessories			0.15
SB-installations			0.3
		Total MSFr.	1.7

Staff: physicists + engineers/technicians, etc.

	1968	1969	1970	1971
Magnet system	2/3	2/3	3/4	3/4
Instrumentation	-	1/2	2/3	2/3
Data-handling system	1/1	1/2	2/3	2/3
General	2/1	2/1	2/1	2/1
Total	5/5	6/8	9/11	9/11

Total man-years	29/35
Average costs per man-year	MSFr. 0.04
Total staff costs during construction period	MSFr. 2.5

b) Data-handling system (First version)

Main computer + CRT		MSFr.	5.0
Auxiliary computer			0.7
Electronic interfaces, links			0.1
HPD:	components		0.8
	construction staff		0.7
Scanning tables			0.25
Buildings:			
	computer and HPD-room 250 m^2, about 2000 SFr./m^2		0.5
	scanning room, offices, etc., 200 m^2, 750 SFr./m^2		0.15
		Total MSFr.	8.2

c) Running costs

Magnet, power, maintenance (supercond. coils)	MSFr./year	0.5
Film		0.5
Tapes		0.2
Staff (including analysis)		0.8
Prescanning		0.2
	Total MSFr./year	2.2

In the case of normal conducting magnet coils, the running costs would be higher by 1 MSFr./year.

* * *

3. EXPERIMENTAL PROPOSALS

3.1 Missing-mass experiment at low momentum transfer

3.1.1 Introduction

In the Omega project we can either treat the instrument as being similar to a bubble chamber (triggering whenever an interaction occurs in the target) or take advantage of the triggering possibility and bias ourselves to some specific interaction configuration. The former possibility may be interesting both from a rate and accuracy point of view, but with the latter we may in addition choose an interaction configuration so as to
(a) reduce the experimental errors (though not without some bias), or
(b) trigger on a specific mass region in which one is interested (e.g. to determine the spin-parity, decay branching ratios, and Δ^2 dependence of a resonance without having to consider the total mass spectrum).

There are two ways in which one might reduce the errors. Consider the reaction $\pi^- p \to pX^-$ and trigger on the recoil proton

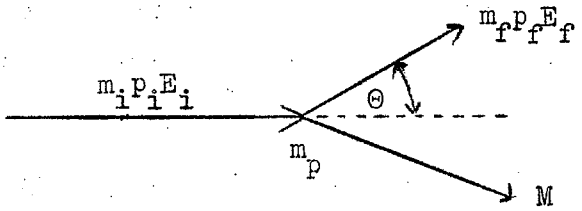

$$M^2 = m_i^2 + m_f^2 + m_p^2 + 2m_p(E_i - E_f) - 2(E_i E_f - p_i p_f \cos\Theta) \qquad (1)$$

$$\delta M_\Theta = \frac{\partial M}{\partial \Theta}\,\delta\Theta = -\frac{1}{M}\,p_i p_f \sin\Theta\,\delta\Theta \qquad (2)$$

$$\delta M_{p_i} = \frac{\partial M}{\partial p_i}\,\delta p_i = \frac{1}{M}\left[p_f \cos\Theta - \beta_i(E_f - m_p)\right]\delta p_i \qquad (3)$$

$$\delta M_{p_f} = \frac{\partial M}{\partial p_f}\,\delta p_f = \frac{1}{M}\left[p_i \cos\Theta - \beta_f(E_i + m_p)\right]\delta p_f \,. \qquad (4)$$

Now since $dM^2 = (\delta M_\Theta^2 + \delta M_{p_i}^2 + \delta M_{p_f}^2)$ we can choose, for a given $\delta p_i/p_i$ of the primary beam (which fixes δM_{p_i}), to operate in such a condition that either $\delta M_{p_f} = 0$ or $\delta M_\Theta = 0$.

Method a): $\delta M_{p_f} = 0$. From Eq. (4), $\delta M_{p_f} = 0$ when $p_i \cos \Theta - \beta_f(E_i + m_p) = 0$. This is the same condition for the maximum angle of the recoil proton in the lab. system as can be seen from Eq. (1) by solving for $\cos \Theta$ and differentiating thus

$$\cos \Theta = \frac{M^2 - [(m_i^2 + m_f^2 + m_p^2 + 2mp(E_i - E_f) - 2E_iE_f)]}{2p_ip_f}$$

$$\frac{\partial(\cos \Theta)}{\partial p_f} = \frac{(m_p + E_i)\beta_f - p_i \cos \Theta}{p_ip_f} = 0 \text{ for minimum } \left[\frac{\partial E}{\partial p} = \beta\right].$$

In this condition we therefore operate with the recoil proton at its maximum angle in the lab. system, and in order to achieve maximum accuracy in the measurement of the missing mass we must measure Θ accurately. Clearly δM_{p_i} should, if possible, be reduced below δM_Θ. This is called the "Jacobian peak method".

Method b): $\delta M_\Theta = 0$. From Eq. (2), $\delta M_\Theta = 0$ if $\Theta = 0$. In this case the error on M depends only on δM_p. That is, p_f must be measured accurately. Clearly δM_{p_i} should be made smaller than δM_{p_f}, that is $\delta p_i/p_i$ must be made sufficiently small.

Δ^2 consideration. Since $\Delta^2 = -2 m_p T_f = -2 m_p(E_f - m_p)$ we have that, for a given M, Δ^2 is smallest when p_f is smallest. Now since

$$E_f = \gamma_c(E^* + \beta_c p^* \cos \Theta^*),$$

then

$$\Delta^2 = -2m_p\left[\gamma_c(E^* + \beta_c p^* \cos \Theta^*) - m_p\right]$$

and this will be the smallest for $\cos \Theta^* = -1$.

Thus method (b) selects events with the smallest possible Δ^2, which is of interest since most Δ^2 distributions fall off exponentially with Δ^2, and one therefore might expect to attain larger rates with method (b).

We have thus considered as a first study a missing-mass experiment using method (b) (cf. Kienzle et al., EEC proposal 10 April, 1967).

3.1.2 Experimental set-up for method (b)

The idea is to trigger the Omega on recoil protons leaving the target at $\Theta^\circ \simeq 0^\circ \pm 12^\circ$ and to select the protons by time-of-flight. For example, the locus of the protons with $\Theta = 0^\circ$ and p_f in the range from 0.35 GeV/c to 1.5 GeV/c with a flight time of 30 nsec is shown in Fig. 3.1.1. Protons with $\Theta = \pm 12^\circ$ arrive ±2 nsec before or after those with $\Theta = 0^\circ$. On the other hand, relativistic pions take ~ 20 nsec from the target to the counter. The time spread due to protons coming from different points in the target is ~ 1 nsec.

3.1.3 Errors on missing mass M

For the Omega the error in p_f in the region of 0.35 tc 1.5 GeV/c is limited by multiple scattering (X_o = 30 m), and is ~ 0.5%. Table 1 gives the error contributions from Θ, p_i, p_f at various incident momenta for a ±4 mrad (¼°) error in Θ, 0.2% error in p_i, and 0.5% error in p_f.

Table 1

		$\Theta = 0^\circ$			$\Theta = 8.5$			$\Theta = 15^\circ$		
p_i	Range of M	δM_Θ	δM_{p_i}	δM_{p_f}	δM_Θ	δM_{p_i}	δM_{p_f}	δM_Θ	δM_{p_i}	δM_{p_f}
20	3.35 → 4.96	0	±4.6	±6.5	±2.0	±4.6	±6.5	±4.0	±4.6	±6.5
11	2.49 → 3.63	0	±3.6	±5.5	±1.7	±3.6	±5.5	±3.0	±3.6	±5.0
8	2.12 → 3.33	0	±3.0	±5.0	±1.5	±3.0	±5.0	±2.5	±3.0	±5.0
4	1.48 → 1.95	0	±2.2	±4.5	±1.0	±2.2	±4.5	±2.0	±2.2	±4.5
GeV	GeV	MeV			MeV			MeV		

From this table it can be seen that:

a) $\delta p_i/p_i$ should be a little less than 0.2%, say 0.1% if δM_{p_i} is to be negligible compared to δM_{p_f};

b) Θ should not be increased much beyond 15° to keep δM_Θ negligible;

c) increasing X_o by a factor 2, i.e. reducing δM_{p_f} by a factor $\sqrt{2}$ could be interesting -- that is, thinner plates or wider spacing;

d) one might expect to reduce these errors by a small amount for 4-constraint and 1-constraint kinematic fits.

* These results may be compared to those expected by Kienzle et al. For example, for p_i = 11 GeV/c and M of about 3 GeV/c they predict $\delta M = \pm$ 9 MeV, whereas with a $\delta p_i/p_i$ of 0.1% the Omega gives $\delta M = \pm$ 5.5 MeV (unfitted events). [Note: Kienzle et al. get same δM if they have same $\delta p_i/p_i$.]

Thus the main features of this experimental arrangement are large solid-angle, high data rate (limited by 20 to 50 msec dead-time of camera in the case of optical spark chambers or $\lesssim$ 10 msec dead-time for wire spark chambers), missing mass to $\pm$ 6 MeV, complete kinematic fitting of the event as in the bubble chamber, observation of the various decay modes of resonances.

3.1.4 Other errors and systematic effects

1) Error in δp_f due to $\pm$ 0.4 cm uncertainty in interaction point in H_2 target. For non-relativistic protons

$$E = \frac{p^2}{2m}$$

$$\Delta p = \frac{m}{p} \Delta E \ .$$

In liquid H_2,

$$\frac{dE}{dX} = \frac{0.24 \text{ MeV/cm}}{\beta^2} \ .$$

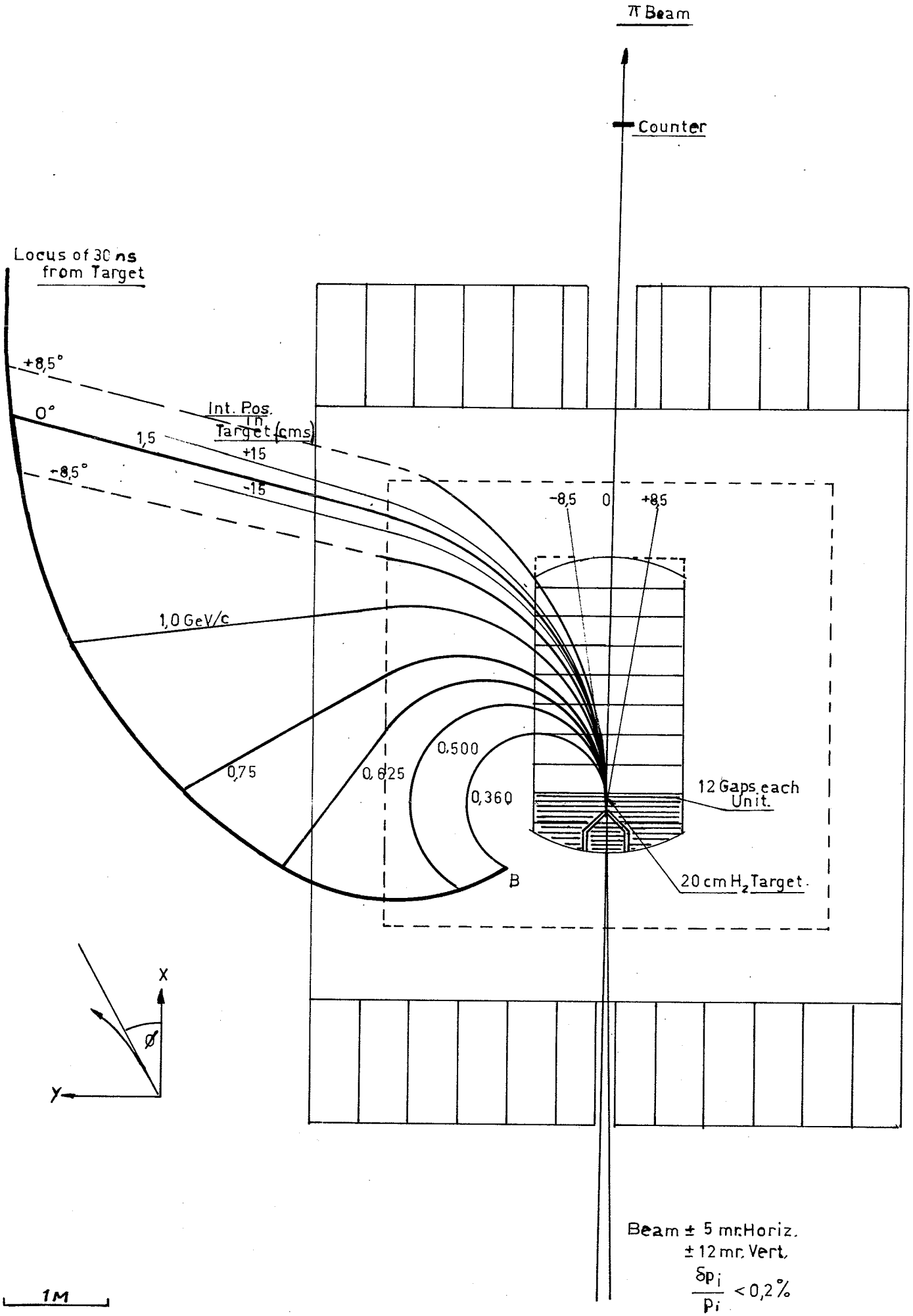

FIG 3.1.1. MISSING MASS TRIGGER

Ex. For $p_f = 0.4$ GeV/c, $\beta = 0.4$

$$\frac{dE}{dX} = 1.5 \text{ MeV/cm, giving } \delta p_f = \pm 1.5 \text{ MeV/c for } \Delta x = \pm 0.4 \text{ cm.}$$

Such an error on δp_f leads to a $\delta p_f / p_f$ of $\pm 0.37\%$ which should be compared to the $\pm 0.5\%$ coming from multiple scattering.

2) Energy loss in H_2 target and 1 mm mylar window. If target is 20 cm long we have a momentum loss of $\sim$ 75 MeV/c in 20 cm, and in 1 mm mylar $\sim$ 2 MeV/c (systematic and correctable).

3) Error on Θ of recoil proton at target due to ± 0.4 cm uncertainty of point of interaction. For $p_f = 0.4$ GeV/c, $\rho = 80$ cm.

$$\Delta\Theta = \frac{\Delta X}{\rho} = \frac{0.4}{80} \rightarrow \pm 5 \text{ mrad giving } \delta M_\Theta \sim \tfrac{1}{2}\, \delta M_{p_f}, \quad \text{therefore all right.}$$

4) Error on Θ at production due to multiple scattering in the H_2 target and mylar window.

$$\Theta = \frac{15(\text{MeV})}{pv(\text{MeV})} \sqrt{\frac{L}{X_0}} \ .$$

$$X_0(H_2) = 10 \text{ m} \quad X_0(\text{mylar}) = 40 \text{ cm.}$$

For 10 cm H_2 $\quad \Theta = \pm 3.2$ mrad
0.1 mm mylar $\quad \Theta = \pm 1.6$ mrad
} leading to $\delta M_\Theta \leq \tfrac{1}{3}\, \delta M_{p_f}$.

3.1.5 Monte Carlo computer study

In order to understand, in more detail, the problems associated with a given experimental arrangement, we have used the data summary tapes of the 8 GeV/c $\pi^+ p$ bubble chamber experiment which contain all the relevant information on the 4, 1, and 0 constraint events.

3.1.5-1 Experimental arrangement for method b): $\delta M_\Theta \sim 0$. In this case the apparatus is triggered on recoil protons in the momentum range ~ 0.35 to ~ 1.5 GeV/c and emitted at small laboratory angles ($\Theta \sim 0^\circ$) to the incident particle. The locus of the positions of protons emitted at $\Theta = 0^\circ$ and with momenta in the above-mentioned range was determined after they had travelled for a flight time of 30 nsec from the target (see Fig. 3.1.1). A hypothetical scintillator was placed at this locus, and the properties of trigger studied as a function of the time gate ($30 \pm \Delta t$ nsec) and the shape of the scintillator in the z direction ($\perp$ to plane of Fig. 3.1.1). It is clear that Δt determines the angles φ in the xy plane of the accepted protons. We found that a $\Delta t = \pm 2$ nsec accepts a $\Delta\varphi = \pm 12^\circ$ about $\varphi = 0^\circ$ (see Fig. 3.1.2).

a) Accidental triggers on π^+

Figure 3.1.3 shows the arrival times of protons and π^+ at the scintillator having dimensions in the z direction of $\pm$ 50 cm. We see that the number of π^+ arriving within 30 ± 2 nsec is $\sim 1.5\%$ of the protons. These π^+ will give spurious triggers. However, on measuring the events, these π^+ can essentially be identified since it is found that the probability of the π^+ having a $|\varphi| < 12^\circ$ is $\sim 3\%$. The Δt can be increased to ± 4 nsec without too much π^+ contamination, but then the φ accepted becomes rather too large if one wishes to keep δM_Θ smaller than δM_{p_f}.

b) Shape of the scintillator and the mass spectrum

If one wishes to maintain the angle of proton emission in the xz plane (λ° or dip) also $< 12^\circ$, then the counter dimension in z must decrease as one goes from the high momentum side to the low momentum side (region A to B of Fig. 3.1.1). However, this gives rise to a missing-mass spectrum which is peaked at high masses. The reason for this is that high masses are associated to small c.m.s. momenta (p^*) of the proton, and a larger fraction of these, than for events with higher p^* (lower missing mass), are transformed into the laboratory system with angles $< 12^\circ$. We thus attempted to compensate for this effect by having a counter with z dimensions constant at ± 50 cm. In this case the dip angle λ reaches 25° at $p_f = 0.35$ GeV/c and decreases to 12° at $p_f = 1.5$ GeV/c. A mass spectrum for two intervals of the final

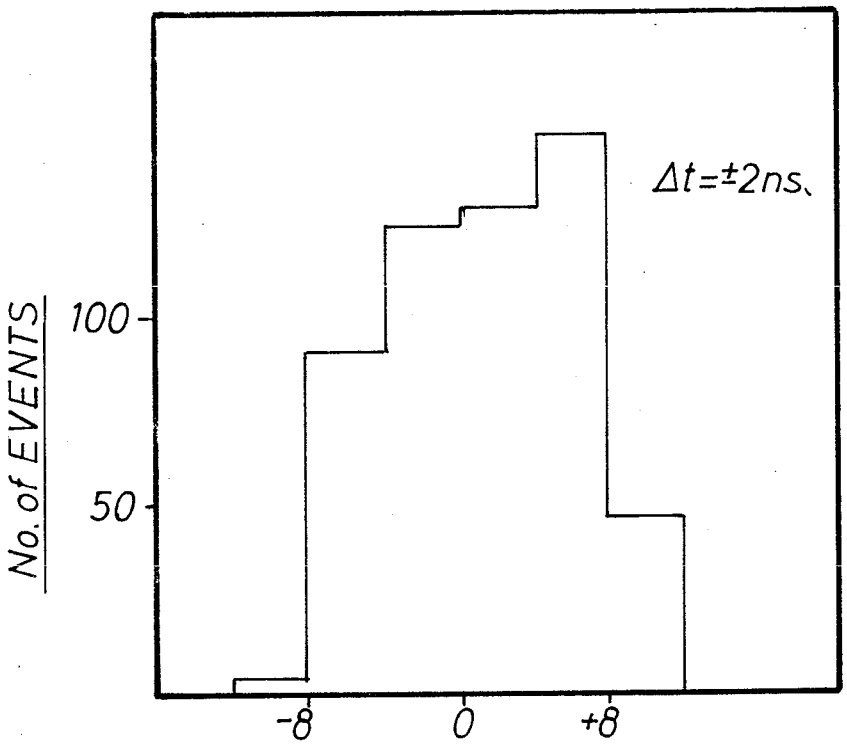

FIG 3.1.2 SELECTION OF PROTON ANGLES BY TIME OF FLIGHT TRIGGERS.

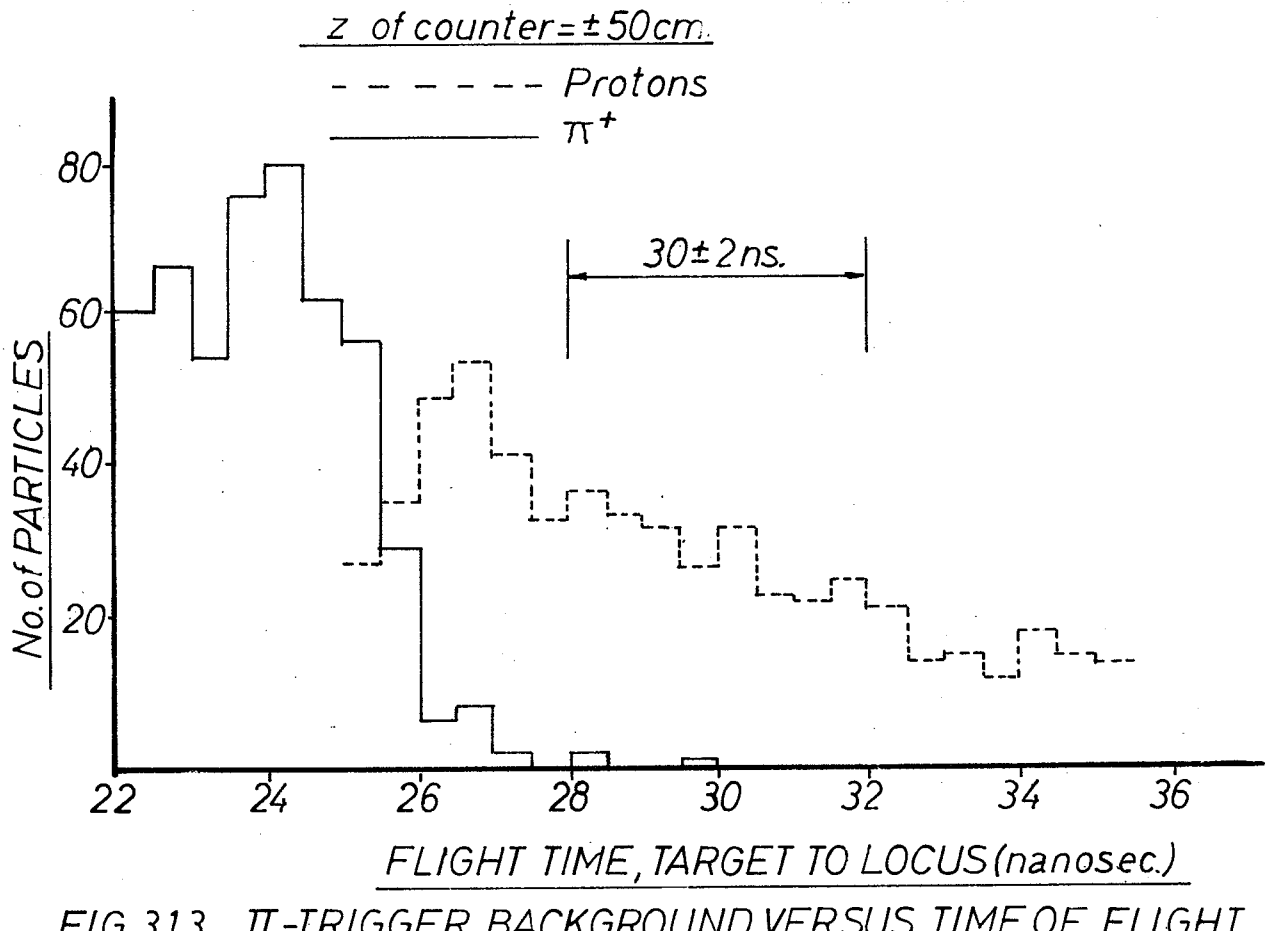

FIG. 3.1.3. TT-TRIGGER BACKGROUND VERSUS TIME OF FLIGHT

recoil proton momentum 0.6 to 1.5 GeV/c and 0.6 to 1.3 GeV/c is shown in Fig. 3.1.4. The peak in the region of 1.3 to 1.5 GeV/c comes from the rapid increase in solid angle accepted in the c.m.s. for small p*.

c) Confusion between proton and π^+ arriving earlier

For the events selected by the trigger, there is a finite probability for a π^+ of the same event to follow a trajectory which could have triggered the apparatus if it had been a proton. For these events one does not know which of the two particles actually caused the trigger, although in fact the π^+ arrived too early. The number of events where this possible confusion occurs is 4%, and can be reduced by dividing the scintillator into sections along the path of the locus.

d) Accidentals due to K^+

A study in which all the π^+ were assigned the mass of the K meson showed that the problems arising from accidental triggers due to K^+ mesons, and confusion between K^+ and proton from the same event, were similar in magnitude to those for the π^+. Since the K^+ production is an order of magnitude lower than the π^+, the problem is one in the 0.2% region.

e) $N^*_{3,3}$ production

The study showed that the percentage of events having a $p\pi^+$ mass combination lying in the $N^*_{3,3}(1238)$ region did not appreciably change, in the events selected by the trigger, from the 25% of all $p\pi^+$ mass combinations for the unselected events.

f) Conclusion on method (b)

It seems to be possible to trigger the apparatus by time-of-flight and obtain a reasonable mass spectrum with a rather small contamination and little bias coming from the need to reject ambiguous events. The trigger rate changes according to the pion multiplicity of the channel but is of the order 2% for recoil momenta between 0.6 and 1.5 GeV/c. Assuming a cross-section of 1 mb and trigger efficiency of one, we would obtain ~ 7 events/burst of 10^6 π's from a 10 cm H_2 target.

3.1.5-2 Experimental arrangement to select on a given mass interval for all Δ^2. Once it is known that a certain region of the missing mass spectrum is interesting, it would be useful to be able to trigger on events lying in this region in order to study it in more detail, e.g. a specific resonance. The locus of the protons after a flight path of 30 nsec coming from events with a missing mass of 2.6 GeV was determined, and the arrival times of the protons and π^+ crossing a scintillator placed at this locus (with z = ±50 cm) is shown in Fig. 3.1.5. In this case we see that ~ 60% of the triggers between 30 ± 2 nsec would be due to π^+. On the other hand, if we accept these triggers, nearly all could be rejected after measurement as the φ distribution of the π^+ and the protons do not overlap (see Fig. 3.1.6).

Figure 3.1.7 shows the mass region at about 2.6 GeV, which is chosen by selecting the protons which arrive at the target in the time interval 30 ± 2 nsec.

Thus it appears that such a trigger is possible if one accepts an equal number of unwanted events which can be rejected cleanly after measurement.

3.1.6 Comparison with the hydrogen bubble chamber

3.1.6-1 Missing-mass distribution of the π^0 in 1C fits. With a program, the fitted quantities (p,λ,φ) of each track were randomized according to the external errors of the equipment (bubble chamber or Omega). These external errors were those needed by the "GRIND" kinematic fitting program to give good X^2 distributions for the fitted events. As a comparison, Figs. 3.1.8 a,b show the distribution of the missing π^0 mass in the reaction $\pi^+ p \rightarrow \pi^+ p \pi^+ \pi^- \pi^0$ for (a) the 2 metre hydrogen bubble chamber, and (b) the Omega. For the Omega, the distribution is a factor of two narrower than for the bubble chamber (essentially because of less multiple scattering).

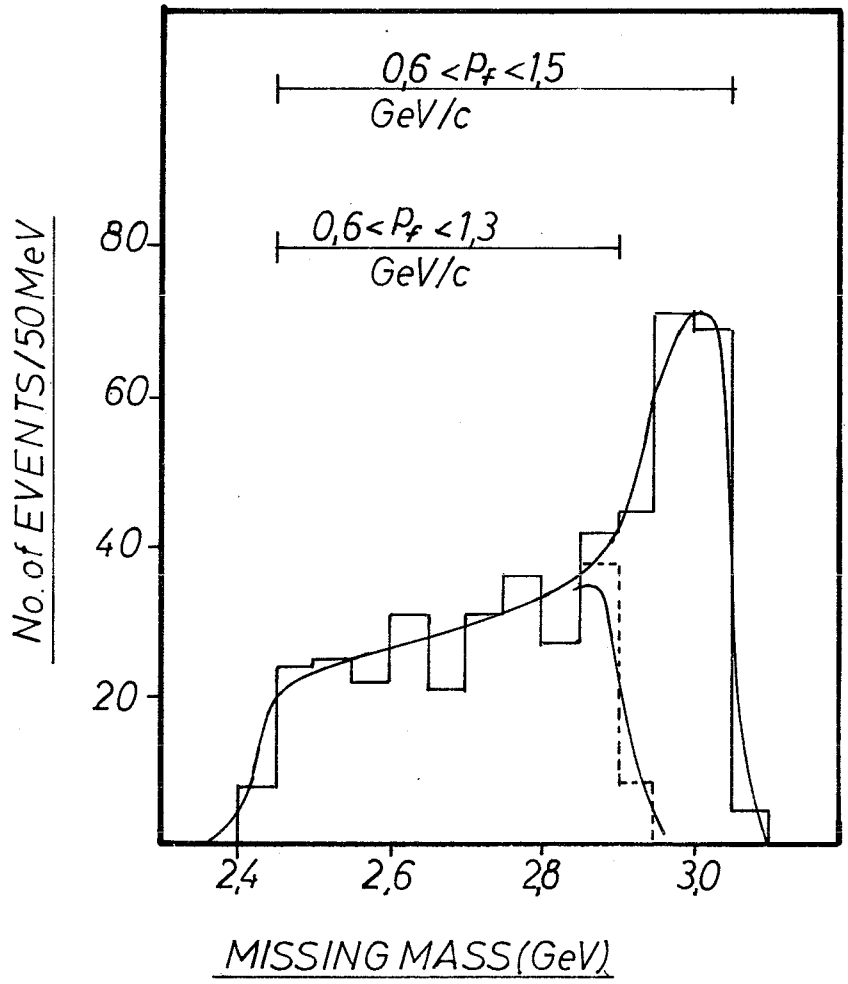

FIG. 3.1.4. MISSING MASS SPECTRA FOR TWO TRIGGER CONDITIONS

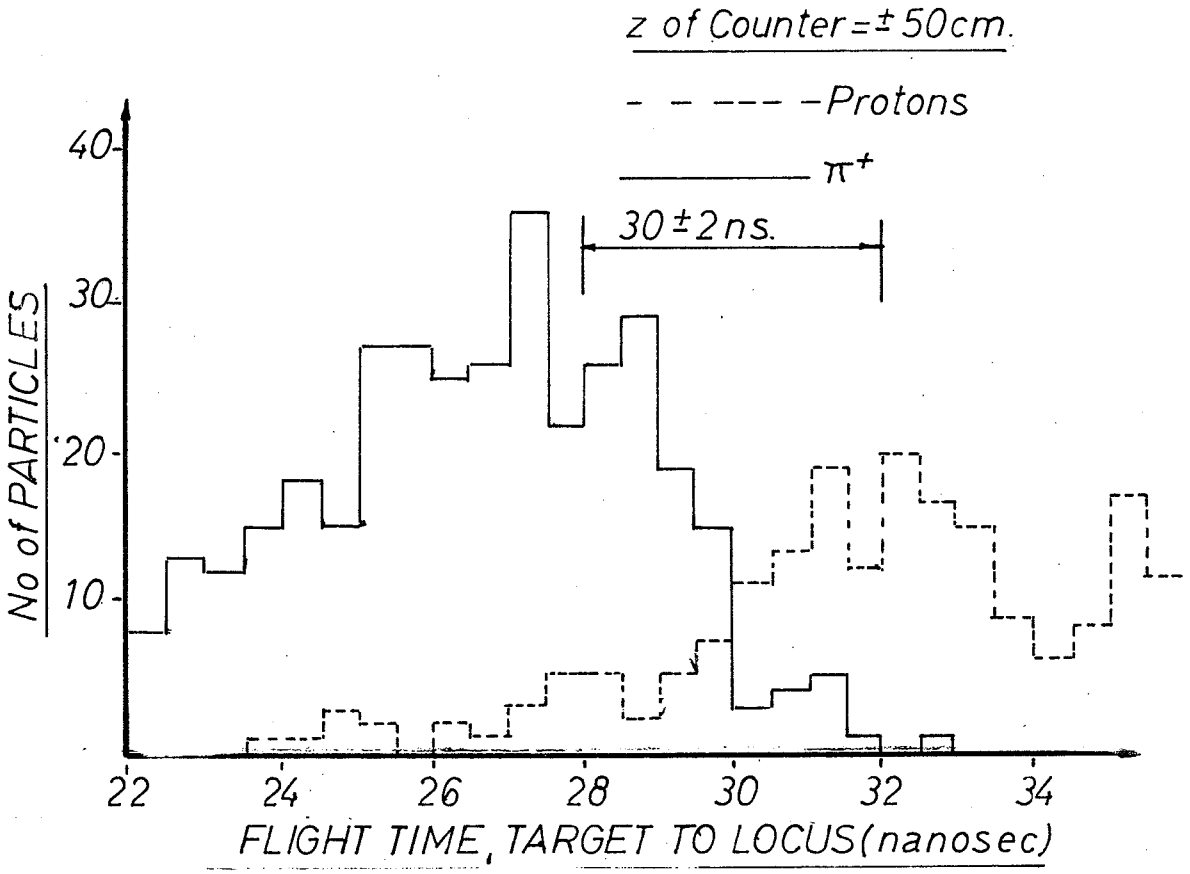

FIG. 3.1.5. TT- BACKGROUND IN A TRIGGER ON A GIVEN MISSING MASS

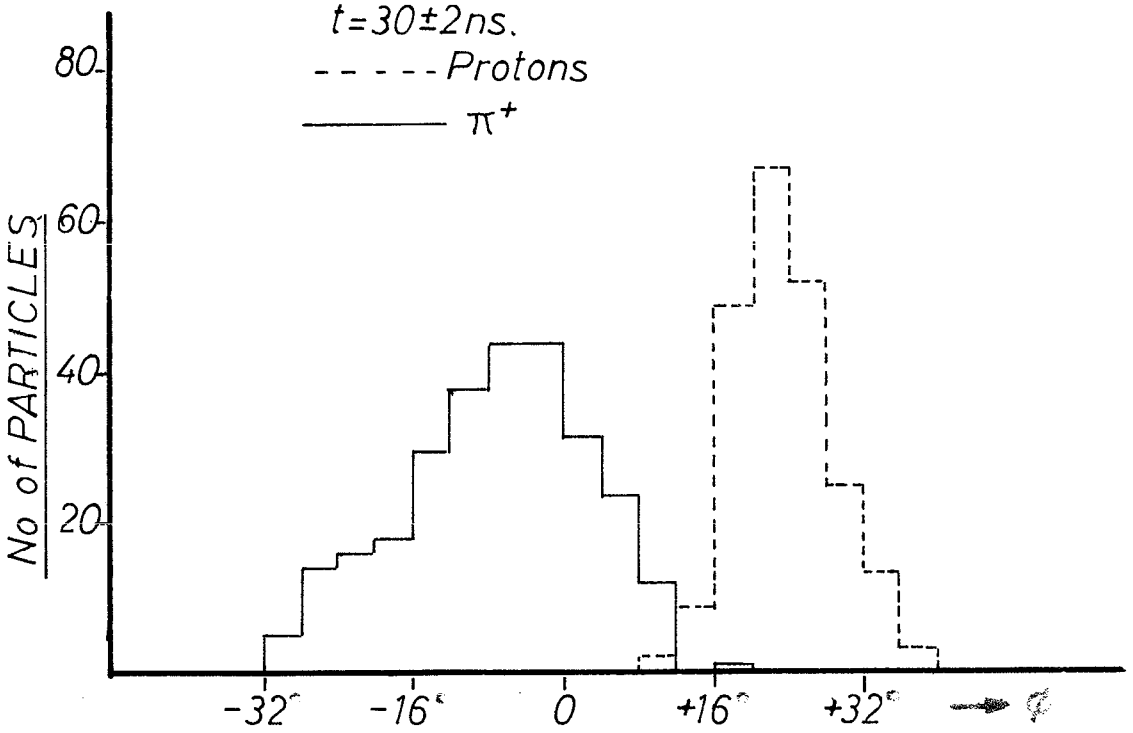

FIG 3.1.6. φ DISTRIBUTION, FOR PROTONS AND π^+ WITH FLIGHT TIME 30±2ns.

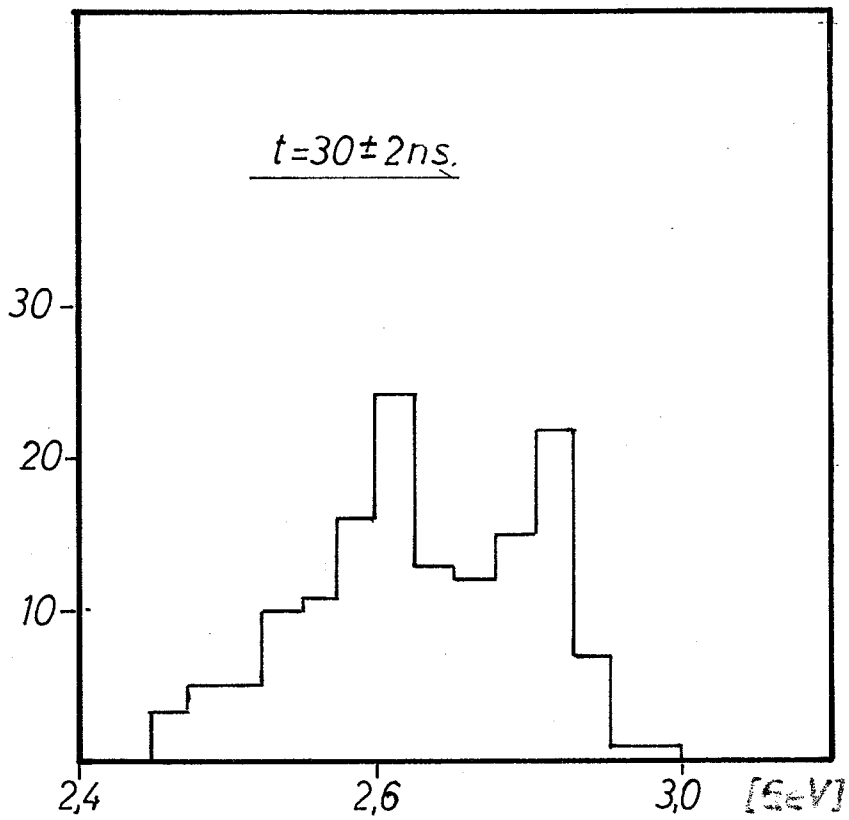

MISSING MASS (GeV)

FIG. 3.1.7. MASS SELECTION BY FLIGHT TIME TRIGGER

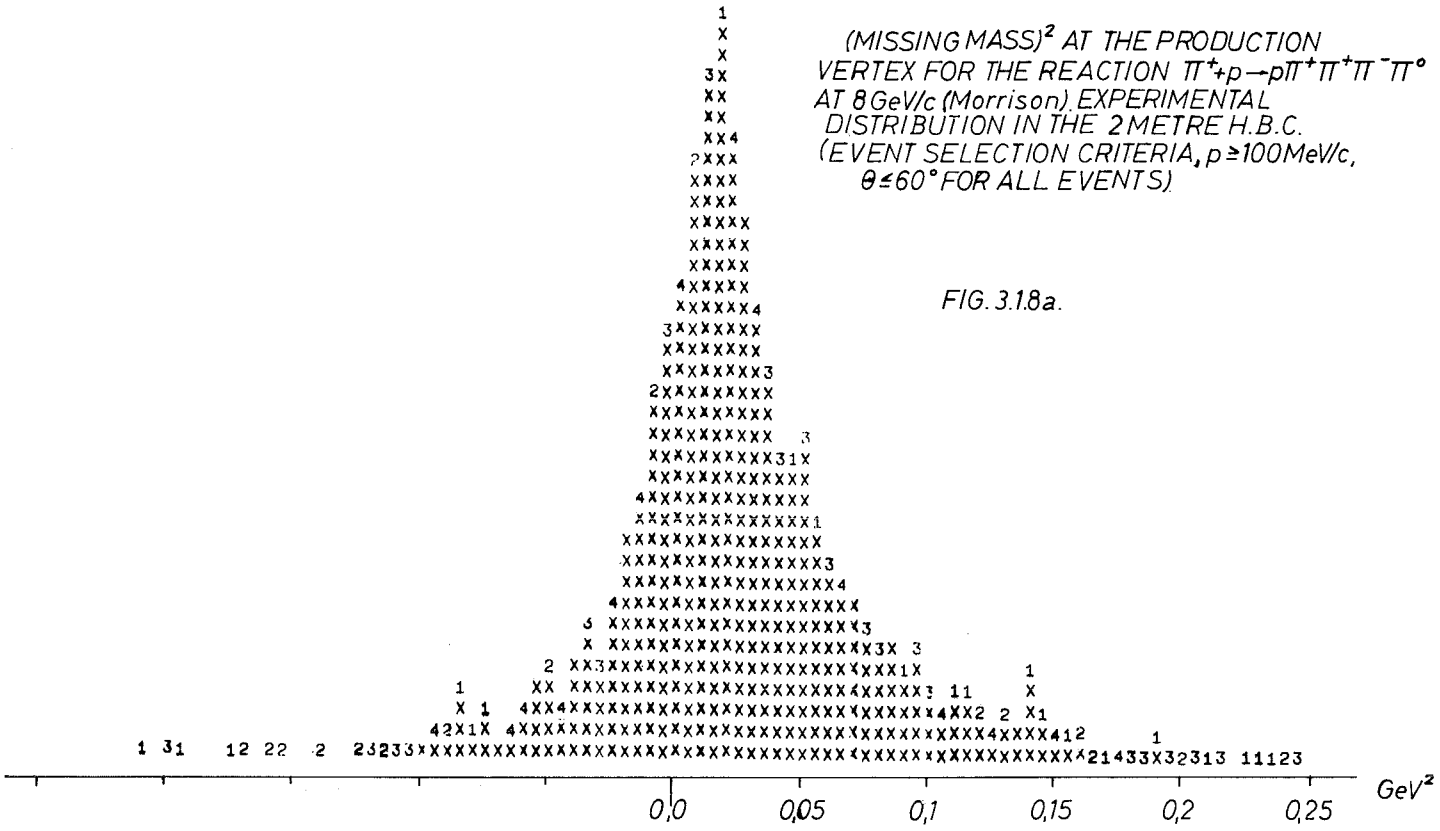

(MISSING MASS)² AT THE PRODUCTION VERTEX FOR THE REACTION $\pi^+ p \rightarrow p\pi^+\pi^+\pi^-\pi^0$ AT 8 GeV/c (Morrison). EXPERIMENTAL DISTRIBUTION IN THE 2 METRE H.B.C. (EVENT SELECTION CRITERIA, $p \geq 100$ MeV/c, $\theta \leq 60°$ FOR ALL EVENTS)

FIG. 3.1.8a.

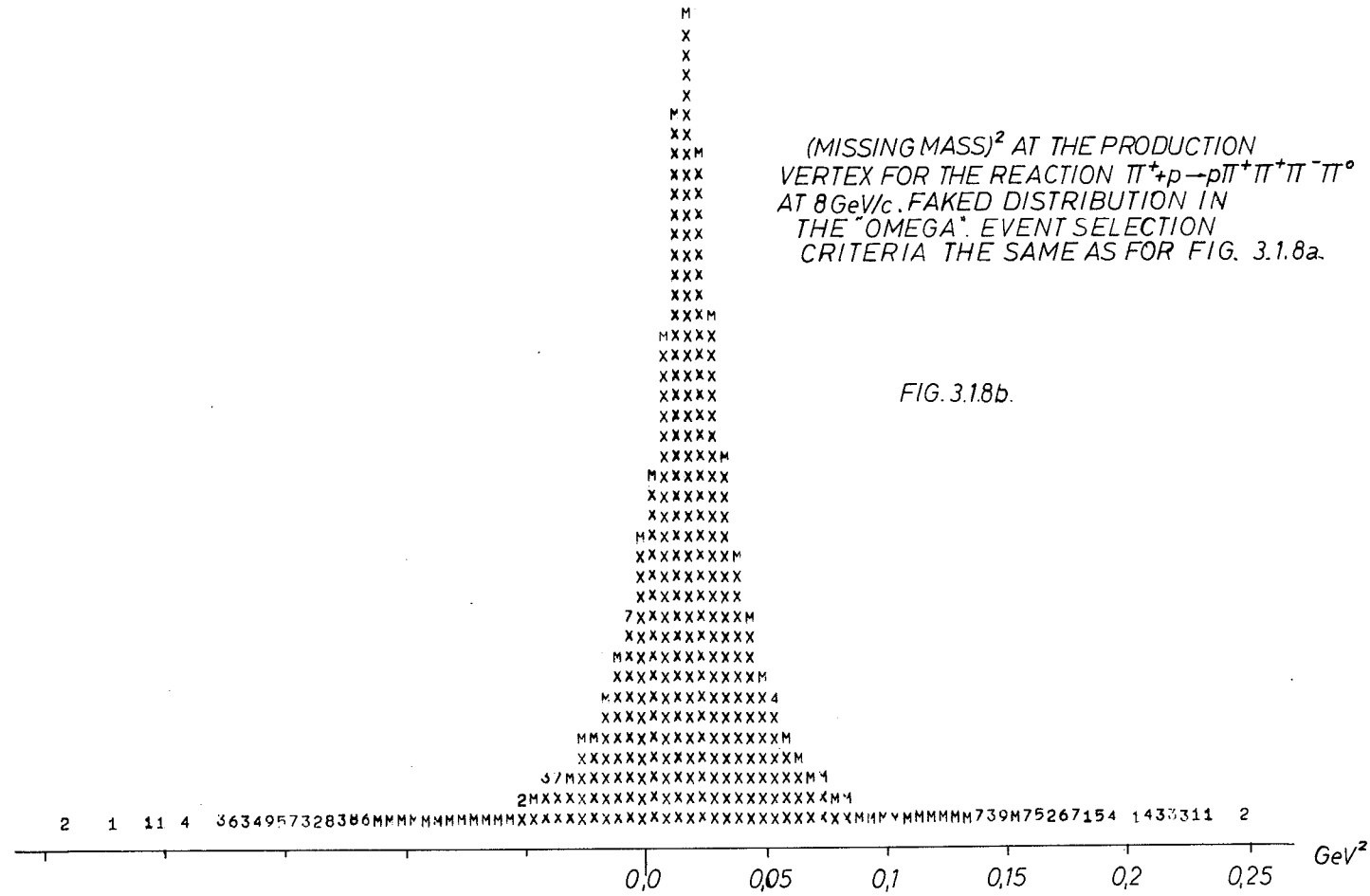

(MISSING MASS)² AT THE PRODUCTION VERTEX FOR THE REACTION $\pi^+ p \rightarrow p\pi^+\pi^+\pi^-\pi^0$ AT 8 GeV/c. FAKED DISTRIBUTION IN THE "OMEGA". EVENT SELECTION CRITERIA THE SAME AS FOR FIG. 3.1.8a.

FIG. 3.1.8b.

3.2 Study of baryon exchange processes

The class of reactions generally described as baryon exchange processes are ideally suited for study with the Omega system. They have a characteristic signature, namely a forward nucleon at close to the beam momentum; and their kinematics require the 4π geometry of the Omega for good efficiency.

3.2.1 Baryon exchange reactions. It is proposed to study processes in which an incident pion or kaon yields a high-energy proton in a small forward cone, such as:

$\pi + p \rightarrow p + \pi$ or $K + p \rightarrow p + K$,	backward elastic scattering	(1)
$\pi + p \rightarrow N^* + \pi$,	forward baryon resonance production	(2)
$\pi + p \rightarrow p + X$,	backward meson resonance production	(3)

plus similar reactions with incident K mesons and backward associated production. Some data is available on elastic scattering, but in the other processes the unique relation of the final-state particles is lost and it is essentially impossible to study them without a 4π geometry. In this sense this report describes how the Omega system could substantially improve an experiment now in progress at CERN.

Figure 3.2.1 gives some kinematics for backward pion scattering and shows the large angular range over which the scattered pion must be measured for a reasonable centre-of-mass range. The equivalent relations for Kp scattering are similar.

In reactions of type (2) in which a proton results from the N^* decay, the opening angle for the proton is small and can be detected with good efficiency; for example, it is 2.1° for the $N^*(1236)$ at 8 GeV/c. Class (3) reactions require the full 4π geometry because of the low velocity of the system X and hence the large opening angle of its decay.

3.2.2 The layout. Figure 3.2.2 shows the configuration for studying backward reactions at the Omega magnet. Upstream from the magnet are the Čerenkov counters and hodoscopes necessary to define the mass, momentum, and direction of the incident particle.

The baryon exchange trigger is downstream from the magnet and consists of a large-element hodoscope as a coincidence requirement and a large-aperture threshold Čerenkov counter to anticoincidence out all but the forward going protons. Elements of the hodoscope would be chosen as a triggering requirement to give the desired maximum proton angle about the zero degree line.

Spark chambers between the pole tips of the magnet fill a path one metre wide and two metres high along the beam line. Additional spark chambers downstream outside the magnet improve the momentum measurement of the proton, which is to a few tenths of a per cent. The liquid hydrogen target is mounted far enough into the field region to permit analysis of 180° scattering.

Particles emitted into the backward hemisphere (lab. system) have a momentum of less than 1 GeV/c in general, and a path length of 50 cm gives the momentum resolution that is permitted by the multiple scattering (a few per cent). A fence of trigger counters around the sides and back of the spark chambers could be used to reduce the triggering rate or could be used at high beam intensities to label the track of interest so as to distinguish it from accidental tracks in the chambers.

If optical chambers were used they could be mounted at 45° to the beam line thus permitting all scattering angles. If wire chambers were used, a more specialized chamber geometry would be possible with better angular coverage.

3.2.3 Trigger and event rates. Recent results on backward elastic scattering and on some backward inelastic processes permit reasonable estimates of rates. For example, at 8 GeV/c the Brookhaven-Carnegie Group *) have measured the total cross-section for backward elastic $\pi^- p$ scattering to be 1.5 μb, for the process $\pi^- p \to p\rho$ to be 1.8 μb, and for all processes in their geometry giving a high-energy forward proton about 100 μb. These results are consistent with other data which show that for reactions permitted by baryon exchange, and usually showing a backward peak, the ratios of the backward to forward cross-sections range from a few hundred to a few thousand. For other processes, the backward cross-sections are down even more, as for example in $K^- p$ elastic scattering. These generalizations are only approximate, but they permit some estimates of rates with a baryon exchange trigger.

*) R.M. Edelstein, private communication.

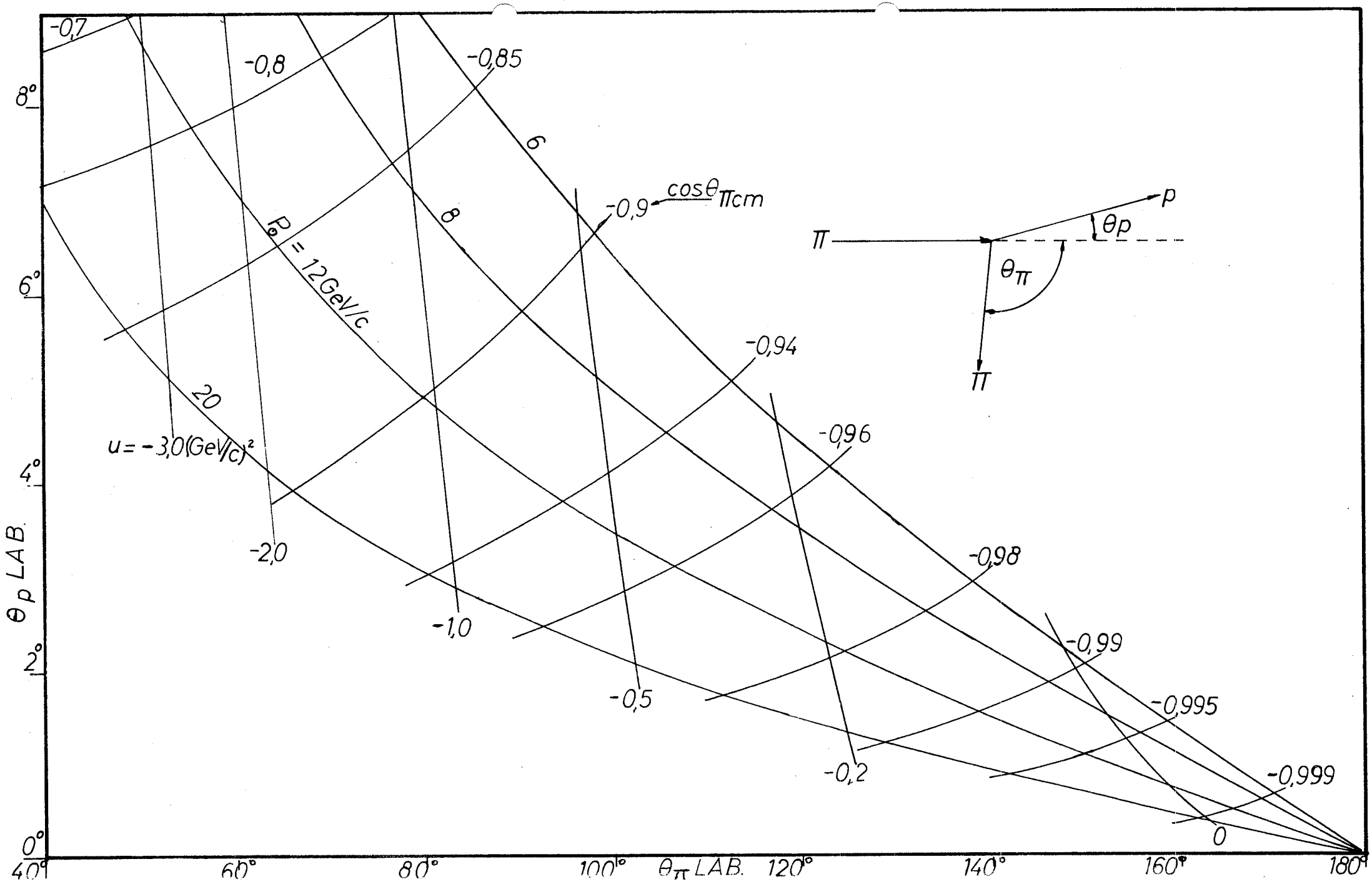

FIG 3.2.1. π-p BACKWARD ELASTIC SCATTERING

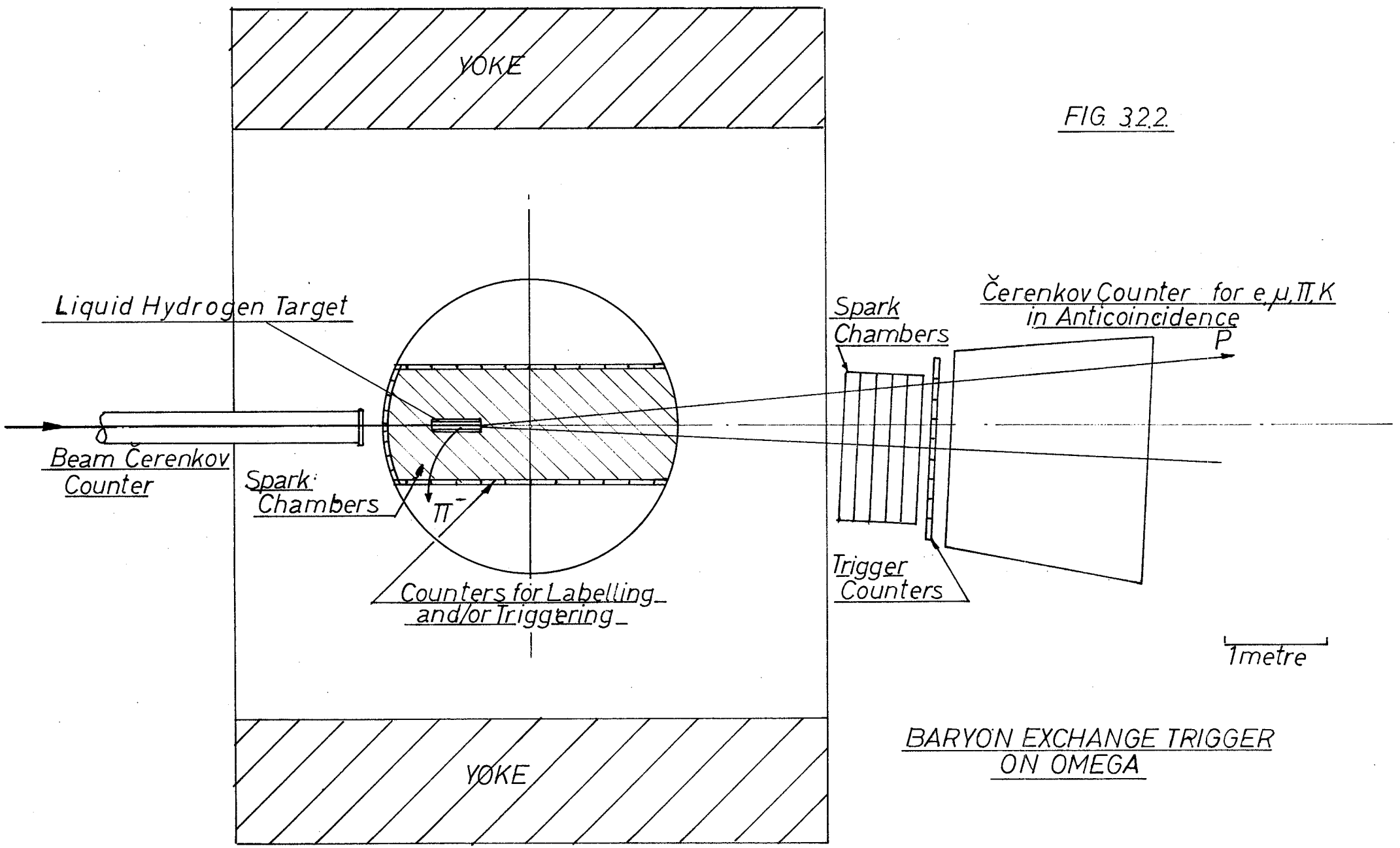

FIG. 3.2.2.

BARYON EXCHANGE TRIGGER ON OMEGA

With the configuration proposed here and a beam of $10^5 \pi^-$/burst striking a 50 cm liquid hydrogen target, a total interaction rate per burst of about 6000 is expected. The above data indicate that of these, at 8 GeV/c, approximately 20 could give rise to a forward proton, and of these 0.3 would be an elastic scattering and 0.4 a backward ρ production. The use of the appropriate fence counters in the Omega magnet could reduce some unwanted triggers. Beams of 10^5 pions per burst should be obtainable at the PS up to about 22 GeV/c.

The baryon exchange trigger alone is quite general and is better suited to wire chambers in which a number of processes could be studied simultaneously. For optical chambers, additional triggering conditions should probably be imposed.

A comparison of this proposal with an experiment now under way at CERN to measure the backward elastic scattering of pions and K mesons shows an increase in solid angle of a factor of 10 plus the momentum measurement of the scattered particle with the Omega. It also becomes feasible to study the inelastic channels.

A further refinement of the baryon exchange trigger would be the detection of a forward neutron instead of the proton. One could then do backward charge exchange scattering and studies with a deuterium target.

3.3 Experiments on leptonic hyperon decays

3.3.1 Introduction

The present*) experimental situation of leptonic hyperon decays needs considerable experimental clarification. A large number of experiments carried out so far has given only rather approximate information on the interaction rate. Only in a few cases have we indications on the form of the interaction by measurements of decay correlations.

On the other hand, current theoretical ideas based on Cabibbo's application of SU(3) to weak interactions appear to be quite capable of standing up to accurate tests. Ideally, one would like to accumulate in this field an amount of information comparable with the present information; for instance, on neutron beta decay

$$n \rightarrow p + e + \nu$$

for which about 10,000 events have been observed from a polarized ($\geq$ 90%) neutron beam.

More precisely, the Cabibbo theory is able to give exact predictions in the SU(3) limit for the absolute strength and the relative phase between the axial vector and vector interactions in terms of the phenomenological parameters F and D. A theorem due to Ademollo and Gatto ensures that, to the first order, the vector part is unaffected by the symmetry-breaking interactions. Quite accurate tests of the theory are therefore possible on the vector part of the weak coupling.

We list in Table 1 the main leptonic hyperon decay processes and the presently measured branching ratios [Brene, Veje, Roos and Cronström, Phys. Rev. 149, 1288 (1966)].

---

*) Of course, it is not known how many of the present questions on hyperon decay would still be open at the time of operation of the Omega project.

Table 1

Leptonic hyperon decays

Process	Branching ratio
$\Lambda \rightarrow pe^-\nu$	$(0.88 \pm 0.08) \times 10^{-3}$
$\Lambda \rightarrow p\mu^-\nu$	$(1.35 \pm 0.6\ ) \times 10^{-4}$
$\Sigma^- \rightarrow ne^-\nu$	$(1.28 \pm 0.16) \times 10^{-3}$
$\Sigma^- \rightarrow n\mu^-\nu$	$(0.62 \pm 0.12) \times 10^{-3}$
$\Sigma^+ \rightarrow ne^+\nu$	Forbidden by $\Delta Q = \Delta S$ rule
$\Sigma^+ \rightarrow n\mu^+\nu$	Two possible candidates detected (Columbia and Heidelberg)
$\Sigma^- \rightarrow \Lambda e\nu$	$(0.75 \pm 0.28) \times 10^{-4}$
$\Sigma^+ \rightarrow \Lambda e\nu$	$(0.13 \pm 0.13) \times 10^{-4}$
$\Xi^- \rightarrow \Lambda e^-\nu$	Only two events observed (questionable?)
$\Xi^- \rightarrow \Lambda\mu^-\nu$	Not observed
$\Xi^\circ \rightarrow \Sigma^+e^-\nu$	Not observed
$\Xi^\circ \rightarrow \Sigma^+\mu^-\nu$	Not observed

A particularly interesting decay is the strangeness conserving $\Sigma^\pm \rightarrow \Lambda^\circ e^\pm \nu$, which is predicted by Conserved Vector Current Theory to be only of the axial vector type.

From the point of view of the determination of the form of the interaction, it is required to measure for each decay the polarization of at least one of the hadrons in order to be sensitive to terms of the form $g_A \cdot g_V$, the correlations between momenta being sensitive only to terms of the form g_A^2 and g_V^2 (Weinberg). Therefore polarization measurements are very essential.

3.3.2 Experimental techniques

Until now the bulk of the information, apart from a few experiments, has been obtained from bubble chamber work.

There are two possible ways of searching for leptonic decays in a bubble chamber:

a) In an H_2 bubble chamber, by measuring all decays and identifying leptonic decays by lack of fit to the more likely (two-body) non-leptonic decay mode. About 10^3 - 10^4 events need reconstruction to yield one good leptonic count.

b) In a heavy-liquid bubble chamber, by recognizing electrons from the characteristic radiative losses. No information is available from production vertex (complex nucleus!) and multiple solutions are encountered in the fit. Furthermore, the polarization of the hyperon is unknown.

The Omega project, being a somewhat intermediate instrument between the bubble chamber and a counter arrangement, appears as an interesting detector in this field because of the possibility of triggering and the much higher incident flux of particles accepted. More precisely:

a) The leptonic (muons and electrons) decays can be readily identified by a threshold gas Čerenkov counter or by penetration of a thick shield. Recently, several experimental groups in CERN and elsewhere have operated threshold gas Čerenkov counters of atmospheric pressure capable of angular acceptances up to some 50 degrees in a variety of shapes and dimensions. The electron detector efficiency is essentially complete, while the rejection against particles below threshold can be as good as a few parts in 10^{-5} *). This clear identification of electrons is possible with the required rejection of non-leptonic decays.

---

*) We are grateful to Dr. V. Soergel for the illuminating discussions on this point.

b) The high incident flux accepted and electronic beam particle identification are such as to permit setting up the Omega spectrometer in an hyperon beam produced outside the detector. As we shall see, this would provide an intense source of hyperons of well-known direction and momentum. Alternatively, hyperons could be produced by a high-flux K^- beam incident on a hydrogen target located inside the dector.

c) The common characteristic of all decays listed in Table 1 is that hadrons at high energies are kinematically constrained to carry away the largest fraction (~ 90% on average) of the kinetic energy of the incident particle, and they are emitted in a narrow cone in the direction of the incident hyperon. For instance, in the decay $\Sigma^- \to \Lambda^0 e^- \nu$ for $p_{\Sigma^-} = 18$ GeV/c, the maximum emission angle for the Λ^0 is about 0.24° and the momenta lay in the interval $15.8 \text{ GeV/c} < p_\Lambda < 18.0 \text{ GeV/c}$.

It is possible to construct reasonably small and efficient detectors to determine the direction of neutrons emitted in decays such as $\Sigma^- \to ne\nu$, $\Sigma^- \to n\mu\nu$. Protons emitted in decays such as $\Lambda \to \pi p$ can be recognized by threshold Čerenkov counters.

The above-mentioned points make of the Omega spectrometer a much more effective instrument than a bubble chamber in searching for hyperon β-decays. On the other hand, the accuracy in momentum and angle measurement being here quite comparable to the ones of a hydrogen bubble chamber, a very precise and complete event reconstruction is expected in general. However, the fact that the spark chambers give a signal every two centimetres of track length in the beam direction, requires that the decay path of the particles involved be larger than several centimetres. Thus high-energy beams are in general preferable.

3.3.3 Negative hyperon beam

We shall try to estimate hyperon fluxes for proton collisions at 24 GeV/c on a thick target. We shall assume a 3 metre beam path embedded in heavy shielding to prevent background from the proton beam. The return yoke of

the Omega magnet would probably constitute the major part of this shield. Suitable magnetic analysis selects a negative beam of about 18 GeV/c. The experimental information on hyperon production in p-p collision is limited to the case of Σ^-, and it comes from a BNL bubble chamber experiment *).

In an exposure of 180 km of proton tracks at 28.5 GeV/c, 15 Σ^- events were observed. Assuming forward-backward symmetry in the production from proton-proton collision and a transverse momentum, p_T distribution of the form $e^{-p_T/p_\perp}$ with $p_\perp = 0.25$ GeV/c, these authors estimate that on hydrogen:

$$\frac{dN_{\Sigma^-}}{d\Omega dp}\ (0°,\ p_{\Sigma^-} = 19.0\ \text{GeV/c}) = 0.054\ \Sigma^-,\ \text{sr}^{-1}\ \text{GeV/c}^{-1}\ \text{int.p}^{-1}$$

with an estimated error of about a factor of 2. This flux is about a factor of 5 smaller than the negative pion flux at the same energies.

Completely arbitrarily we shall apply the "thumb rule" of reducing the yield by a factor of 10^2 at each additional strangeness unit of the emitted hyperon. This gives the following guesses:

$$\frac{dN_{\Xi}}{d\Omega dp}\ (0°\ p_{\Xi} = 19.0\ \text{GeV/c}) = 5\times10^{-4}\ \Xi^-\ \text{sr}^{-1}\ \text{GeV/c}^{-1}\ \text{int.p}^{-1}$$

$$\frac{dN_{\Omega^-}}{d\Omega dp}\ (0°\ p_{\Omega^-} = 19.0\ \text{GeV/c}) = 5\times10^{-6}\ \Omega^-\ \text{sr}^{-1}\ \text{GeV/c}^{-1}\ \text{int.p}^{-1}$$

A considerable loss is expected because of decays in flight. After a 3 metre path, for a momentum of 19.0 GeV/c the expected yields are as follows:

Particle	Yield at target	Yield at 3 m
	$\text{GeV}^{-1}\ \text{sr}^{-1}\ \text{int}^{-1}$	$\text{GeV}^{-1}\ \text{sr}^{-1}\ \text{int}$
Σ^-	5×10^{-2}	9×10^{-4}
Ξ^-	5×10^{-4}	8.2×10^{-6}
Ω^-	5×10^{-6}	1.75×10^{-8}

*) A. Thorndike et al. BNL. We are grateful to Dr. J. Sandweiss for providing us with this piece of information, and for many discussions on the subject.

Assuming Δp = 1 GeV/c, $N_p = 5\times10^{10}$, $\Omega = 10^{-4}$ sr, we get at 3 metres from target

Σ^-	Ξ^-	Ω^-	π^-
4500/pulse	40/pulse	0.08/pulse	1.2×10^6/pulse

These fluxes are quite adequate for several interesting experiments.

Particle identification in the incoming beam could be obtained with a differential Čerenkov counter DISC*). However a rather complicated beam transport with superconducting lens-elements is required to match the acceptance of the DISC with the emittance of the beam. More conservatively, a threshold gas Čerenkov veto-counter could be used to reject the bulk of fast particles (π^-, K^-), and hyperons could be further identified by the decay configuration and kinematics.

3.3.4 The decays of Ω^- particle

Fourteen Ω^--hyperon decays are known so far. The possible decay modes calculated as well as possible on the basis of SU(3) by Glashow [Physics Letters 10, 144 (1964)] are listed in Table 2 below:

Table 2

Decay mode	Decay rate ($\times 10^7$ sec^{-1})	Branching ratio (%)
$\Xi^0\pi^-$	178	39.5
$\Xi^-\pi^0$	86	19.1
ΛK	94	20.9
Σ^0K^-	2.4	0.6
$\Sigma^0\bar{K}_0$	0.8	0.2
$\Xi^{0*}\pi^-$	38	8.4
$\Xi^{-*}\pi^0$	22	4.9
$(\Xi\pi\pi)$ not res.	1	0.2
$\Xi^0e^-\nu$	18	4.0
$\Xi^0\mu^-\nu$	12	2.7
$\Xi^{0*}e^-\nu$	2	0.4
$\Xi^{0*}\mu^-\nu$	0.1	0.02

*) R. Meunier has designed one of such counters for the present type of investigation. We are grateful to Dr. Meunier for stimulating and interesting remarks on the subject.

There is a considerable interest in detecting the two-body decay $\Lambda^{o}K^{-}$, which could permit a convenient spin determination. Furthermore, it must be remarked that the leptonic decay rates are now predicted to be ~ 4% of all decays, and therefore it is probable that these decay channels would be accessible as well.

3.3.5 Experimental arrangements with negative hyperon beams

Every potential experiment would require its specific triggering logic. However, a number of remarks can be made:

i) The triggering could make use of the following points:

a) the incident particle is slow, or has a given velocity if DISC is provided;

b) there are a number of decay products coming from a region with little or no material;

c) in case of leptonic, electron, or muon decays, the nature of lepton is identified;

d) the last stable baryon is emitted with forward cone and identified by a neutron or proton detector.

ii) The polarization of the incoming hyperon would most likely be zero. Therefore non-leptonic decay processes are the main polarization analysers. In particular, the decays

$$\Lambda^{o} \rightarrow \pi^{-} p$$
$$\Xi^{-} \rightarrow \pi^{-} \Lambda^{o}$$
$$\Xi^{o} \rightarrow \pi^{o} \Lambda^{o}$$

have large and well-known spin correlation coefficients.

* * *

4. FUTURE DEVELOPMENTS

4.1 Use of wire chambers

4.1.1 Operation of wire chambers with core read-out at the "Omega"

Wire chambers with a suitable read-out system are of great interest for the Omega project. They offer the following advantages.

i) No need for a hole in the magnet, as compared with the case of optical chambers. This means better homogeneity of the field.

ii) High speed of data taking. Recovery time of the order of 1 msec can be achieved, particularly for chambers with core read-out, because in this case the spark current can be limited to several amperes. The read-out speed could be between 3 and 5 msec for about 10^5 cores.

iii) On-line control of the experiment.

iv) Event processing faster than for optical chambers. No HPD.

Wire chambers with core read-out have already been in use for several years. These chambers consist of two planes of parallel wires with a gap of between 4 and 12 mm. The spacing between two wires in one plane is usually of the order of 1 mm. After passage of a particle the chamber is triggered, and the HV pulse applied to one wire plane produces a spark between the two planes. The current in the corresponding wire sets a ferrite core similar to that in the core memory of a computer. Both planes, ground plane and HV plane, may be connected to such a core memory in order to record two coordinates of the spark when the wires of the group plane and the HV plane are not parallel to each other. After some delay, the read-out electronics scans all the cores and transfers the coordinate of the spark position to an on-line computer.

The chambers for the Omega project will have a size of approximately 1.5 × 1.5 m, and they will be placed in a magnetic field of about 15 kG. The total number of ferrite cores may well exceed 10^5. The following points will be discussed briefly. To trigger the chamber, a HV pulse of several kilo-

volts and 150-200 nsec width has to be applied. Smaller chambers are normally treated as a capacitive load, where the HV pulse is fed in at one corner or one side. Baker et al. at CERN use chambers which are driven by a bus-bar going along one side of the chamber. The wires are connected to the HV bus via a resistive paste in order to limit the spark current and to decouple the wires from each other (Fig. 4.1.1). The present size of such chambers reaches 1025 mm × 512 mm. Another system is used by the groups of Schopper in Karlsruhe and Vivargent-Winter at CERN. In their chambers (size: 150 cm × 50 cm), the wires are capacitively coupled to the HV bus. At the other end a resistive paste connects the wires to ground (Fig. 4.1.2).

Going over to large chambers, one has to consider the fact that reflections to the HV bus may cause different voltages along the chamber, leading to non-uniformity in efficiency because of the rather small plateau width compared with normal optical spark chambers. One certainly can overcome this problem by feeding the HV pulse to the bus-bar at several points along the chamber. But this might turn out to be difficult for chambers which have the wires of the ground- and HV-plane perpendicular to each other.

A third system, used by the CERN-Aachen Collaboration, is very well suited for large chambers. The HV bus-bar is constructed as a stripline with a well-defined distance to the ground plate, and the wires of the HV plane are connected to this HV bus-bar by means of a resistive network, with resistors between bus-bar and wire and between two neighbouring wires (Fig. 4.1.3). In this way the whole chamber, together with the HV line, forms a distributed stripline of defined impedance (in this particular case of 8 Ω). Several chambers can be joined in series through an 8 Ω cable (six 50 Ω cables), and the last chamber is terminated with an 8 Ω resistor. The time constant to charge the wires is about 3 nsec, which means the rise-time on the chamber is determined by the pulsing system. After two chambers, 190 cm × 46 cm, the rise-time of the pulse is increased by about 5 nsec. The resistors limit the spark current to several amperes in order not to disturb the transmission properties of the stripline, to guarantee high multispark efficiency, and to avoid breaking the wires. The HV pulser can be connected to the chamber by an 8 Ω cable of almost any length.

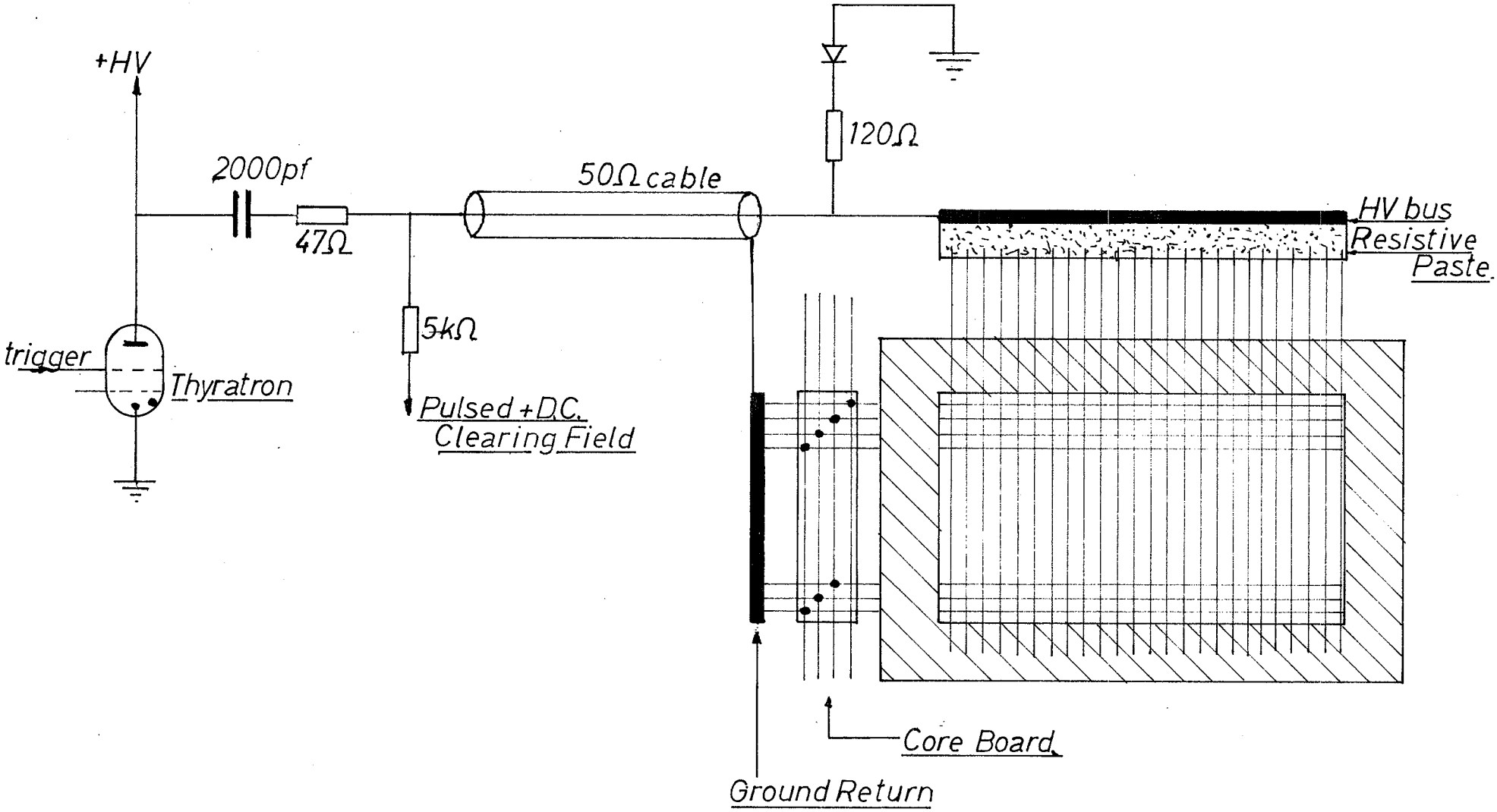

FIG.4.1.1 WIRE CHAMBER SYSTEM F.W.BAKER et.al.

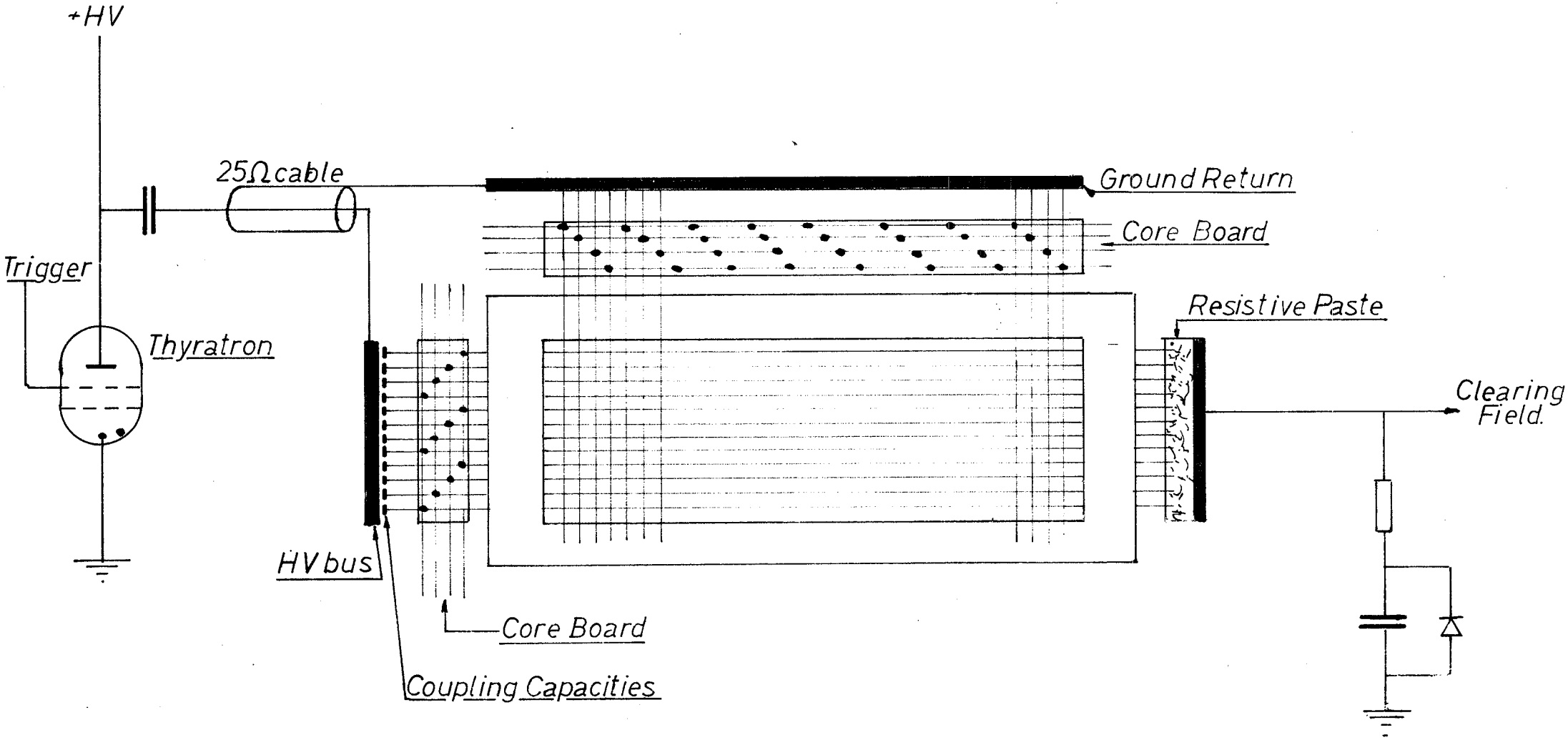

FIG.4.1.2. WIRE CHAMBER SYSTEM, H.SCHOPPER et al.

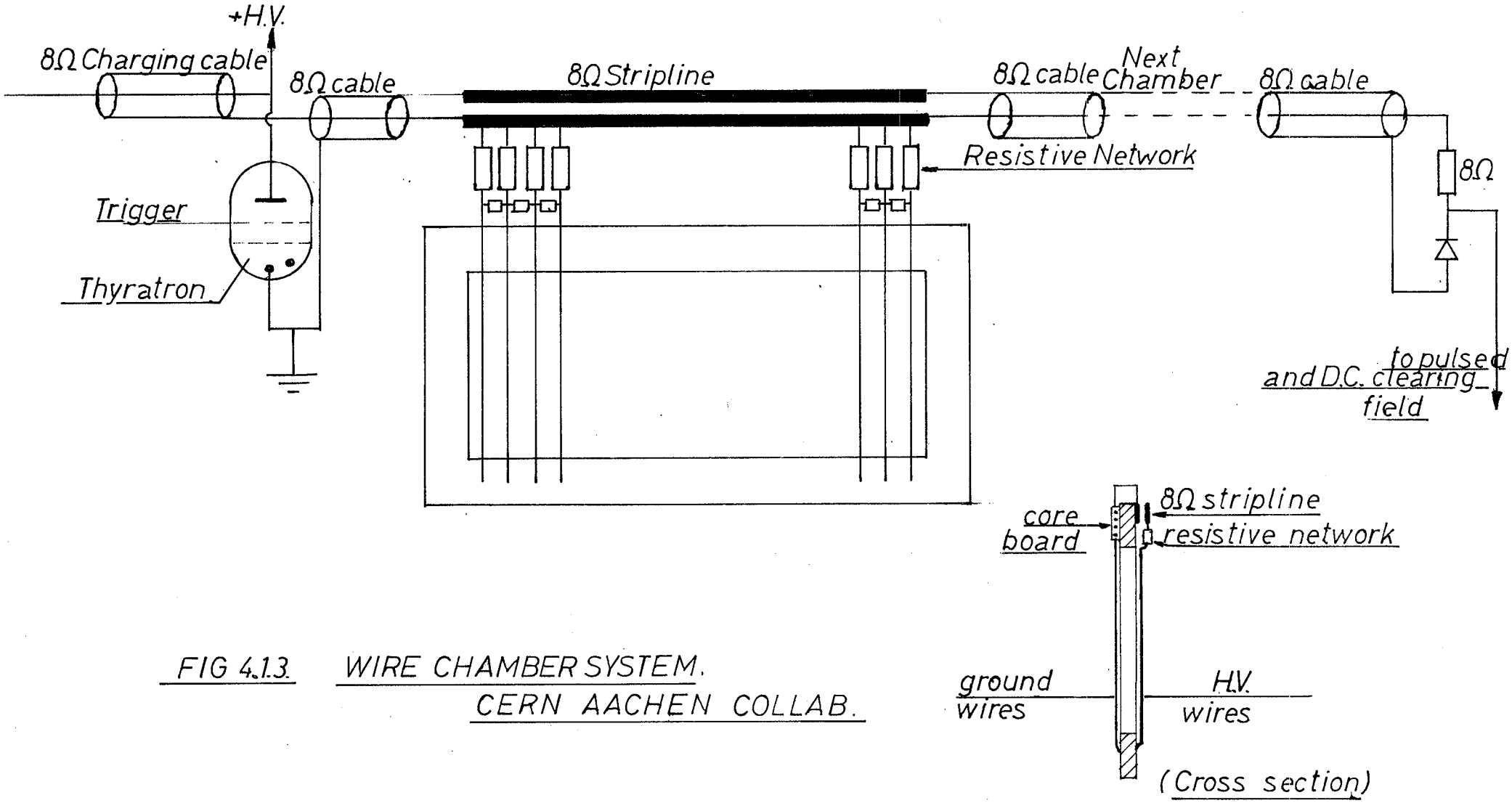

FIG 4.1.3 WIRE CHAMBER SYSTEM.
CERN AACHEN COLLAB.

To pulse the chamber, one discharges a capacitance, or to obtain a square pulse a charging cable, with a conventional spark gap, or more recently with a hydrogen thyratron. The latter offers the advantage of higher reliability, longer lifetime, and faster repetition rate (up to 1 kHz). A rise-time of 15-20 nsec and a delay of the order of 40 nsec can be achieved. The thyratron is triggered with a chain of avalanche transistors, or with an avalanche transistor followed by a microwave triode.

One applies a d.c. clearing field to the chamber to reduce the memory-time. Additionally, a pulsed clearing field of about 1 kV for 1 msec, immediately after the trigger pulse, sweeps the electrons and ions, and in this way reduces the recovery-time. At Brookhaven, chambers have been running with a repetition rate of 1 kHz.

One problem, which still has to be solved, is that of the proper shielding of the ferrite cores from a magnetic field. The cores currently in use at CERN will not function in a field larger than 50 gauss. To shield the cores properly in the Omega magnet seems to be rather difficult. A possible solution is to bring them out to a place with a sufficiently low field. The distance between chamber and coreboard might then be easily several metres. It can be bridged by striplines of defined impedance for each wire in the chamber. There exist straps containing 30 or more such striplines of an appropriate size. Chambers with the cores far from the frame have already been operated in Chicago. The Saclay Group at CERN uses twisted wires to connect the chamber to a compact core module. This module is still attached to the frame.

The CERN read-out system, developed by the group of Pizer and Lindsay, is now in use in two experiments (Baker-Lundby and CERN-Aachen Collaboration). It is able to read 64 thousand cores. Extension should certainly be possible. Furthermore, two read-out systems, perhaps even more, can work in parallel.

The read-out speed is about 40 nsec/core + 2-4 μsec/wire coordinate transfer time to the computer, depending on the type of computer. This results in a total read-out time of about 3.5 msec for 120 thousand cores, with two read-out systems in parallel, and about 200 sparks/event with two wires/spark on the average.

One important figure is the spatial resolution. Ideally one should expect ± ¼ wire spacing. The Baker-Lundby Group measured a spatial distribution of sparks in a chamber around the fitted straight line with a half maximum width of ± 0.3 mm for 1 mm wire spacing, very close to the above-mentioned limit. Regarding the effective radiation length of such a system for the beryllium bronze wires of 0.1 mm diameter, one gets about 10^{-3} radiation lengths per coordinate plane reading only the ground plane (foils and gas not included). Reading both planes one gains a factor of two. A further improvement is possible by use of bronze wires of 0.05 mm diameter (increase in X_0 by factor 4) or aluminium wires.

4.1.2 Operation of wire chambers with magnetostrictive read-out in a magnetic field

A wire chamber with magnetostrictive read-out [V. Perez-Mendez and J.M. Pfab, Nucl. Instr. and Methods 33, 141 (1965)] can be operated in a magnetic field, provided appropriate precautions are taken. If FeCo (Vacoflux) wire is used, then the magnetostrictive properties most relevant for this application are the following [L. Kaufmann et al., UCRL 16536 (1966)]:

i) a magnetic bias with a component along the wire of 10 to 100 Oe must be applied at the receiving coil;

ii) if the component of the magnetic field along the wire increases to more than ~ 2 kOe, the output amplitude decreases until it becomes comparable with noise;

iii) the polarity of the output pulse is dependent on the orientation of the component of H along the wire.

A test of wire chambers with magnetostrictive read-out has been made in an existing spark chamber magnet. To fulfil condition (i), a shielding cylinder of soft iron around the receiving coil has been used. This shielding is not very critical. Good operation up to 12 kOe has been achieved. In order not to exceed the maximum longitudinal field, all the magnetostrictive wires are put perpendicular to the average direction of the magnetic field. Since in this way one cannot read electrode wires perpendicular to the magnetic field, the electrode wires are arranged at 0° and ~ ±11° to the magnetic field, as shown in Fig. 4.1.4. The output pulses change the

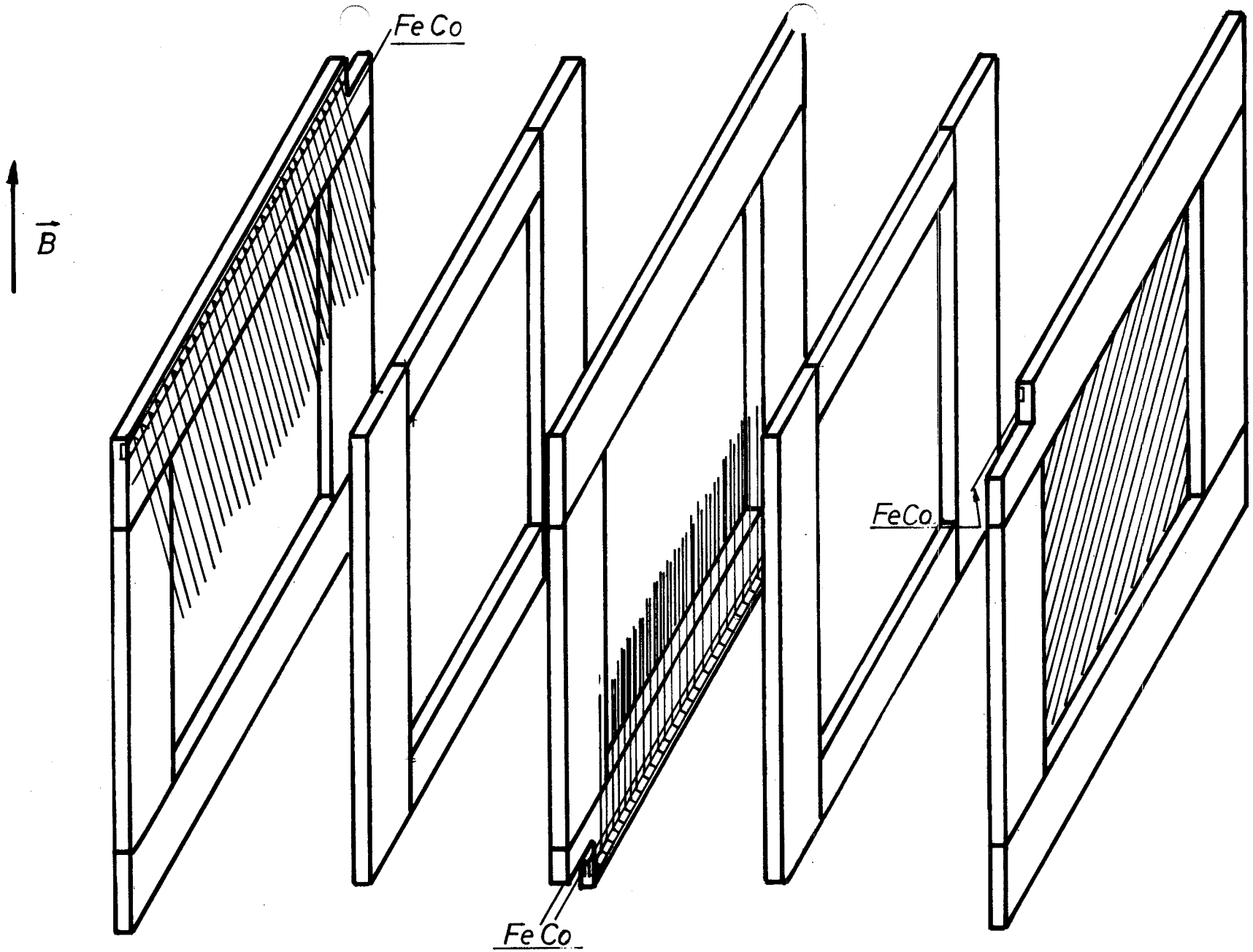

FIG. 4.1.4. WIRE CHAMBER WITH MAGNETOSTRICTIVE READOUT

polarity where the component of H along the wire goes through a zero. A special discriminator can give a timing which is independent from the polarity and to a large extent from the amplitude of the pulses (~ 6 : 1 range). A block diagram of the discriminator is shown in Fig. 4.1.5, together with the waveforms at various points. The dead-time is increased by at least a factor of 2 in comparison with standard one-polarity magnetostrictive read-outs, giving so a two-spark resolution of 9 mm.

More sophisticated circuits can attain the same two-spark resolution as found in chambers with one-polarity output, and allow a true zero-crossing timing for better accuracy and independence from pulse-height amplitude.

4.1.2-1 Possibility of applications to the Omega. The operation of wire chambers with magnetostrictive read-out is possible in uniform fields of up to 12 kG. This is the field at the position of the magnetostrictive wire. Whenever the field value required in the chamber or the homogeneity in the readout region do not meet the specifications, it is possible to apply shielding and shimming which can be designed by straightforward methods. The most obvious solution for fields lower than the saturation of iron is to locate the magnetostrictive wires in slots made in the pole piece of the magnet.

4.1.2-2 Main features and possibilities of the magnetostrictive read-out. The coordinate measurement is made by encoding the delays of series of pulses. The read-out time depends on the degree of serialization in the read-out system [G. Brautti, CERN 66-30 (1966)]. It is 200 μsec per metre of total length of read-out wires connected in series. The number of series connections has to match the input capabilities of the on-line computer, so that the computer input speed is the only limiting factor.

A system which can be adapted to many series-parallel operation schemes is now (August 1967) being prepared for an experimental group (Kienzle) by the NP data-handling group. Important operating experience will be gained with it in the next months, to be added to that of the full serial system already in use.

The recovery-time of the chambers is largely dependent on the energy dissipation in the spark. With the present system, recovery times of the order of 10 msec were observed. By the use of de-exciting agents (alcohol) or a pulsed clearing field, shorter recovery-times are expected.

4.1.3 Non-magnetic read-out methods of wire chambers

4.1.3-1 Standard sonic chambers. The standard sonic chambers were used in experiments with no more than one particle per chamber. Their use with multiple tracks has proved to be possible but difficult. The additional difficulties in existing models are:

i) large energy / spark and long recovery-time;

ii) two-spark resolution of a few cm;

iii) large dead area around the gap, needed to damp the sonic waves;

iv) long read-out time (1 msec/m + damping time). This is not a strong limitation if compared with systems using a (partially) serial system.

The advantages are:

a) good precision;

b) simple construction;

c) cheap read-out systems are possible because of low speed.

4.1.3-2 Sonic wire with piezoelectric read-out [L. Kaufmann et al., UCRL 16536 (1966)]. Sonic pulses can be generated in a wire stretched perpendicular to the electrode wires (as the magnetostrictive wire) if a secondary spark is allowed to jump from the electrode wire to the delay wire. The electrode wires have to be connected to the common electrode through high resistances. The return path for the current of the spark is through the delay wire (non-magnetic stainless steel or brass). The sonic pulse is detected by a piezoelectric detector.

Disadvantages: minimum two-spark separation larger than in magnetostrictive read-out, due to mismatch at the detector. It can be reduced by careful matching of the wire to detector [B. Leskovar, UCRL 17434 (1967)].

Advantages: fully non-magnetic.

The mismatch problem can also be solved by transforming the longitudinal waves into torsion waves, and bringing the torsion wire out of the magnet, where conventional magnetostrictive transducers can be used. The longitudinal-to-torsion and torsion-to-longitudinal wave conversion is a well-tested procedure widely used in commercial delay lines.

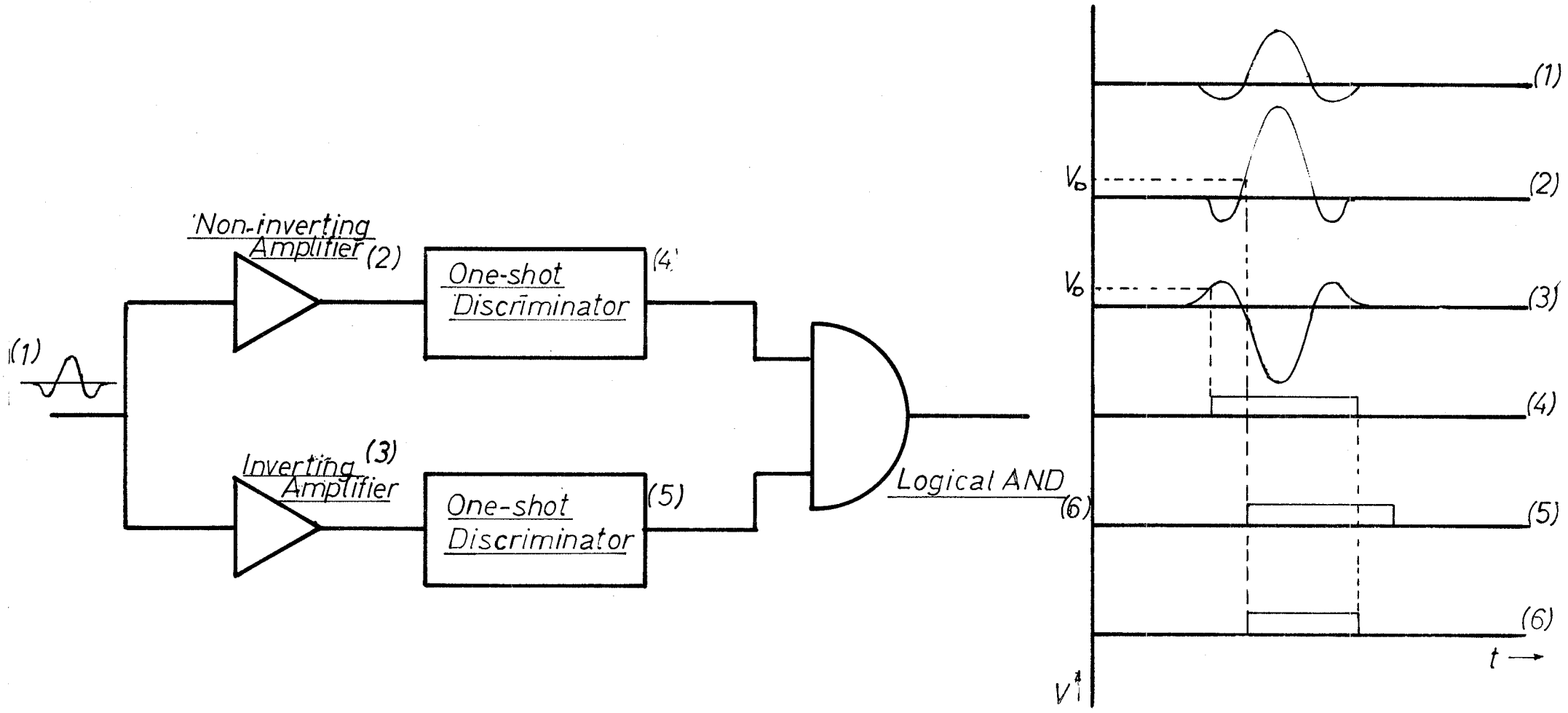

FIG.4.1.5. DISCRIMINATION OF MAGNETOSTRICTIVE SIGNALS

4.1.3-3 Secondary discharge spark chamber (SDSC). The SDSC is a three-electrode structure [M.J. Neumann, CERN 64-30, 133 (1964)] with two unequal gaps (e.g. 6 and 1 mm). The larger gap is used as a normal triggered gap. To the second one a d.c. voltage is applied and a secondary spark is produced corresponding to the position of the first one (Fig. 4.1.6). This spark can be maintained for many μsec, until the d.c. voltage is switched off, giving a (semi-)permanent memory of the coordinate. There are several methods of interrogating the wires, and it is possible to resolve all the ambiguities with one such unit. A prototype of this chamber has already been built [M.J. Neumann, idem], but its performance is not well known. Weak discharges and low recovery times should be possible. Simpler chambers with a single gap were also proposed [M.J. Neumann, idem], but they require one output wire per electrode wire as do the core chambers when used in a magnet.

A different and simpler version of this chamber is sketched in Fig. 4.1.7. The secondary spark is obtained between the electrode wires and the read-out wire. The interrogation of one plane is made by switching off the d.c. voltage on the read-out wire. The output is taken from the resistors on the electrode wires, where many chambers can be connected in parallel.

4.1.3-4 Scratch-pad memories. An obvious solution is to use a bistable circuit (tunnel diode, flip-flop) connected to each wire. The memory can then be interrogated at a much higher speed than for a core memory. If the circuit can work in the magnetic field, only the address wires plus the output bit need be brought outside the magnet. We have noticed that normal transistors and integrated circuits have very short lifetimes when operated in the magnetic field. However, more experience is needed in order to draw any conclusion. If integrated scratch-pad memories can be used, the system is somewhat more expensive than that of cores, but it allows the highest speed of operation ($\sim$ 50 nsec/wire).

4.1.3-5 Current division chambers. The current division chambers [G. Charpak et al., CERN 64-30, 333 (1964)] can be used without magnetic components in the magnet. However, they can handle only one track/plane, and their precision is lower than in the other chambers considered. Some use could be envisaged in chambers where only one particle is expected.

4.1.3-6 Capacitive storage system. Capacitive storage seems to be a fairly natural choice [E. Quercigh, Nucl. Instr. and Methods 41, 355 (1966)]. If integrated circuits can be used inside the magnet for sensing the voltage on single wires, then a development study would be very interesting. Otherwise they require the same number of wires out of the magnet as do core chambers. This type of chamber is highly competitive in speed, precision, and completeness of information.

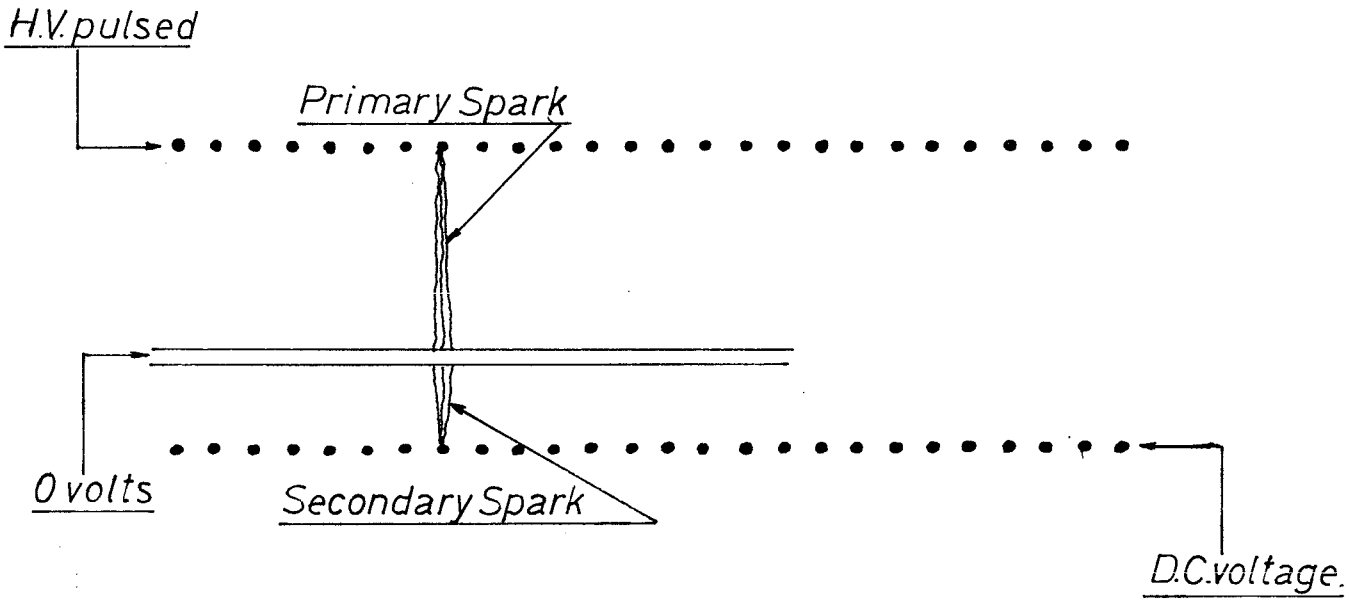

FIG. 4.1.6. SECONDARY DISCHARGE SPARK CHAMBER

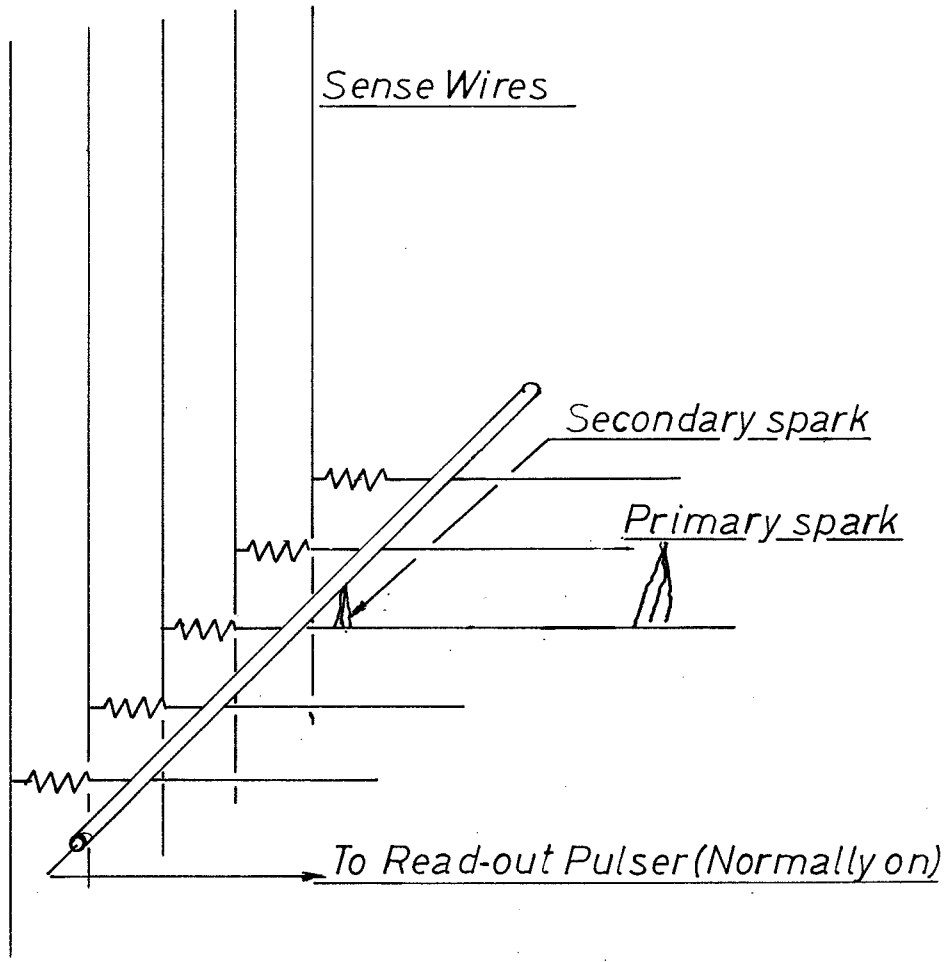

FIG. 4.1.7. SIMPLIFIED VERSION OF S.D.S.C.

4.2 Magnet set-up at the intersecting storage rings

4.2.1 General layout

The possibility of installing and using the Omega instrument in connection with the ISR has been considered.

It has been found that the best conditions for detecting and analysing events produced in the intersection region will be obtained if the colliding beams cross the Omega magnet. The intersection point should be situated approximately at the magnet centre.

Clearly, if the colliding beams cross the Omega magnet field, the bending effect of this field must be compensated so that the normal operation of the ISR is not disturbed.

The compensation in a first-order approximation will be obtained if, at the beginning and at the end of the straight section where the Omega is installed, the radial and angular displacements of the equilibrium orbits of the two colliding beams is zero.

A more detailed analysis of the second-order errors introduced by this compensation will be given in Section 4.2.2.

For a given bending power of the Omega magnet, the simplest scheme of compensation is the one represented in Fig. 4.2.1a. In this scheme there are two compensating magnets, symmetrically placed with respect to the centre of the Omega magnet.

This scheme has, however, two main disadvantages:

i) the intersection point of the colliding beams does not coincide with the centre of the Omega magnet;

ii) particles emitted from the intersection point at small angles are at first deflected by the Omega magnet field in one direction, and then are deflected back by the compensating magnet which could make their detection very difficult.

A second scheme which eliminates or reduces these inconveniences is shown in Fig. 4.2.1b. In this scheme, for each one of the two intersecting beams,

all the compensating elements are located at one side (upstream) of the Omega magnet. The main disadvantage of this scheme is that the total required bending power of the compensating elements is much larger than before. Since the available straight sections are of limited length, high-field bending magnets will be required.

The preferred scheme (which is shown in Fig. 4.2.2) closely approaches the scheme of Fig. 4.2.1b. Only a very small bending magnet is located downstream after the Omega magnet. In spite of its small dimensions, this magnet allows for compensation, within the limits of the available length, using magnets producing fields not higher than 30 kG. We estimate that, at the present time, it would not be practical to exceed this field value. The equilibrium orbit through the Omega and compensating magnets is shown in Fig. 4.2.3.

To detect particles emitted at small angles from the intersection point, it would be very useful for the diameter of the colliding beams to be made as small as possible. The Terwilliger scheme or a reduced momentum band would permit the use in the straight section of vacuum pipes for the circulating beams of a diameter not larger than 5 cm.

In the example shown in Fig. 4.2.4 it is easy to calculate that it will be possible to detect particles emitted at zero angle from the central interaction point only if these particles have a momentum lower than 18 GeV/c (the momentum of the circulating beam is assumed = 27 GeV/c).

The detection of particles emitted at small angles will require also that the wall thickness of the vacuum pipes be very small, and that the detectors be placed as near as possible to the vacuum pipe.

An aluminium wall thickness of 0.2 mm will introduce an error due to the particle scattering through the metal which is comparable to the error made when determining the particle direction using two spark chambers spaced 2 m apart.

In our example, the over-all error with which the momentum of an emitted particle can be measured will be approximately 1%.

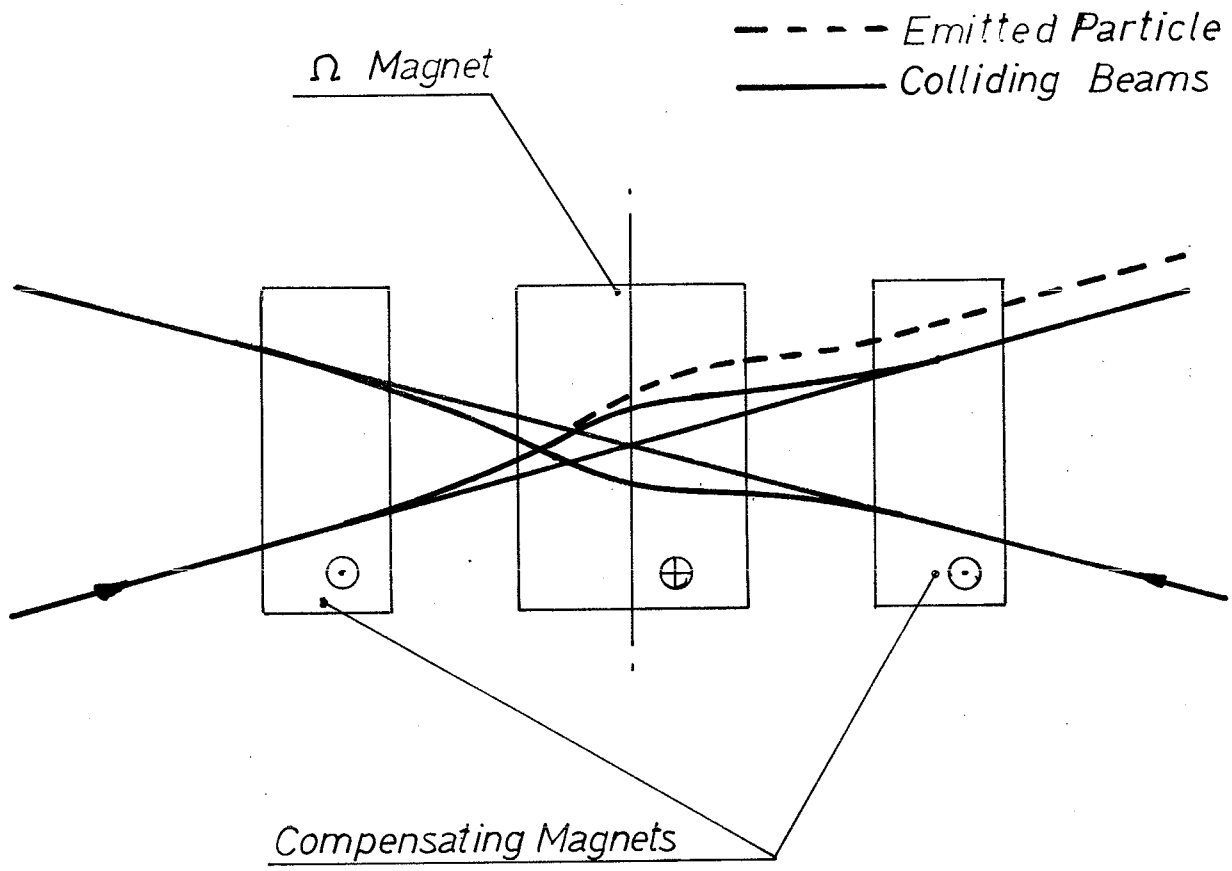

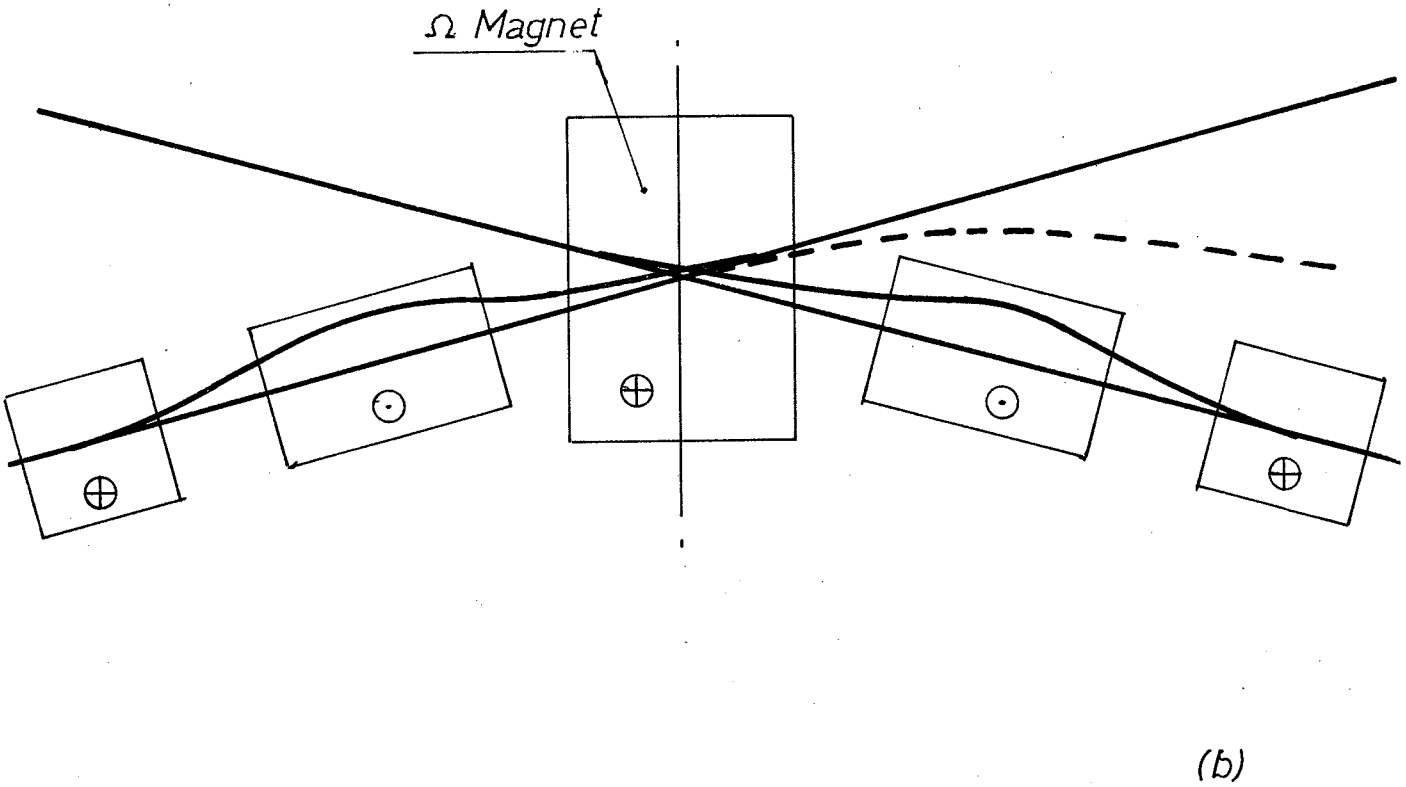

FIG. 4.2.1. TWO POSSIBLE FIELD COMPENSATIONS IN THE STORAGE RING

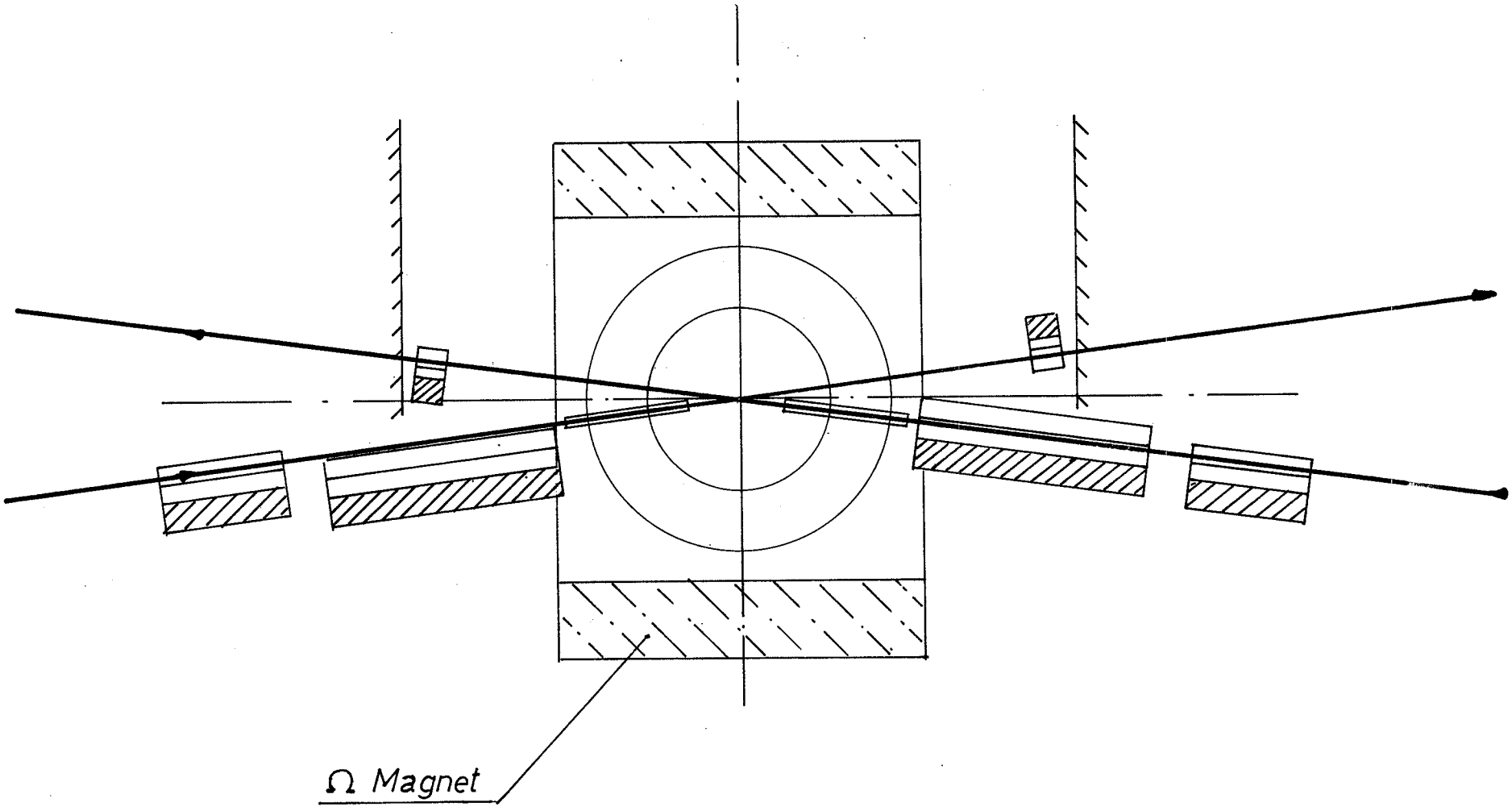

FIG 4.2.2. PROPOSED SCHEME OF FIELD COMPENSATION

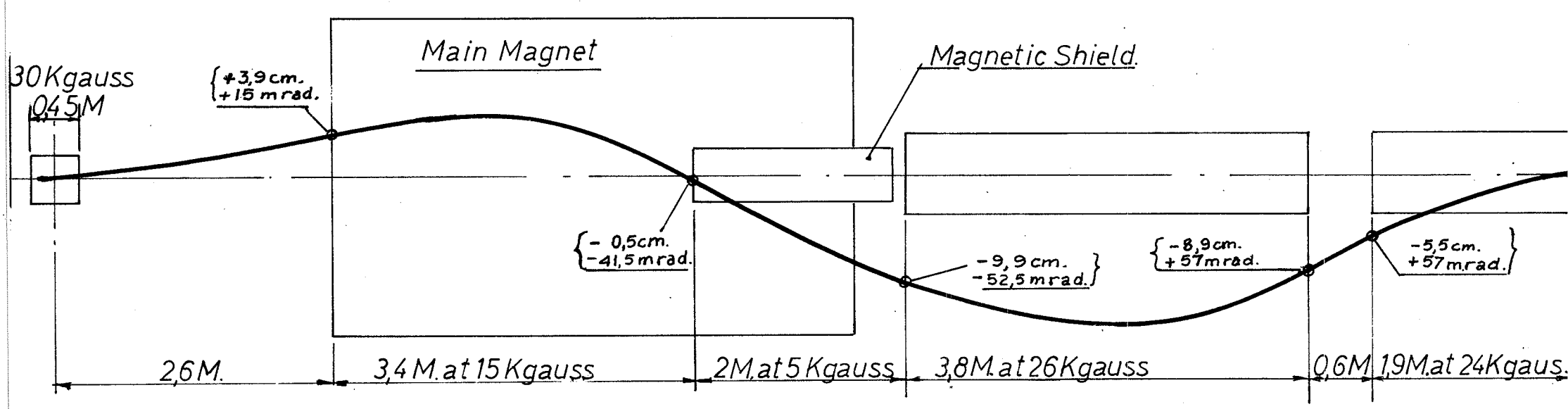

FIG 4.2.3. FIELD DISTRIBUTION ALONG THE BEAMS

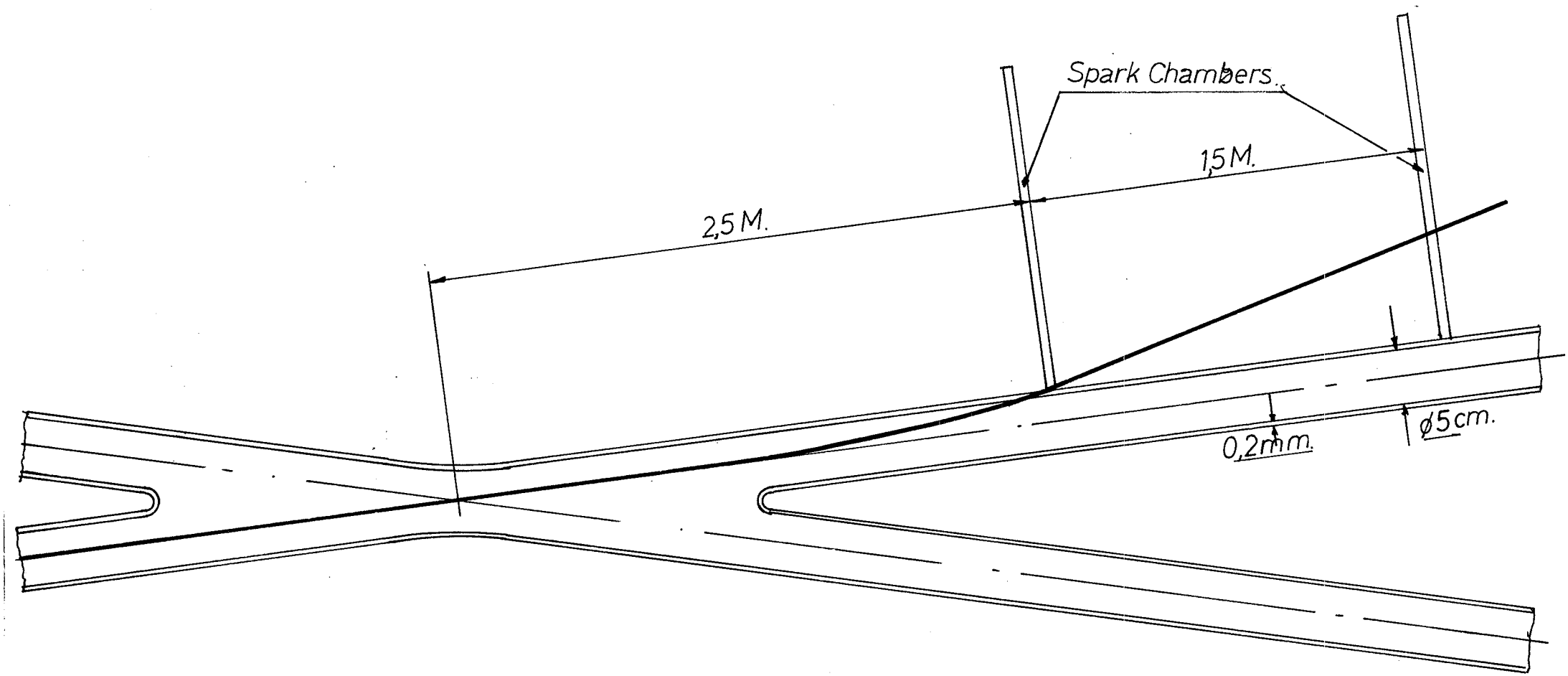

Fig. 4.2.4. TRACK OF 18GeV/c ZERO ANGLE PARTICLE . BEAM MOMENTUM = 27 GeV/c

The installation of the Omega instrument at the ISR will raise problems of a more practical nature, which should be seriously considered. It should be remembered that when the Omega is installed in the ISR, no maintenance or modification work will be possible without stopping the circulating beams.

For this reason it will be necessary, on the one hand, that all parts and elements of the Omega instrument be of the highest standard so as to keep to a minimum the unforeseen interruptions of the ISR operation. This is particularly true for some elements of the detector to which it will be difficult to have access, and which may require a considerable amount of work before they can be repaired or replaced.

On the other hand (in the event of modifications being required, or if there are radical changes in the experimental set-up), we have foreseen the possibility of removing the entire Omega installation by rolling it into the adjacent experimental hall. However, this operation would not be very simple, and it could be done only in the case of major modifications. To displace the Omega it would, in fact, be necessary to

a) disconnect all cables and pipes;

b) dismount the shielding wall of the ISR tunnel;

c) break the vacuum in the section of the vacuum pipe crossing the Omega;

d) roll the Omega into the experimental hall;

e) replace and repump the vacuum pipe section;

f) install a bending magnet with the same bending power as that of the Omega magnet;

g) remount the shielding wall.

These operations would require a few days of machine interruption.

4.2.2 Tolerances

4.2.2-1 The ideal situation. We consider straight homogeneous magnets of the strengths indicated in Fig. 4.2.5. Such magnets have, in the central region not perturbed by fringe effects, a magnetic field which is independent of radial position, and an effective lenght which is also constant across the aperture.

One expects such magnets not to focus a beam horizontally, but to have some vertical edge focusing. An arrangement of several of them such that the total bending angle vanishes, does not disturb the momentum compaction function in first order.

This is confirmed by the figures given in Table 1 for the maximum values of the horizontal and vertical betatron function β_H and β_V, and for the momentum compaction function α_p with and without the Omega magnet arrangement, respectively. It is seen that the vertical edge focusing also has a very small effect on the maximum value of β_V.

Table 1

Orbit parameters with and without Omega magnet

	β_H (m)	β_V (m)	α_p (m)
No Omega magnet	41.0441	51.2040	2.2787
With Omega magnet	41.0547	52.3384	2.2803

4.2.2-2 Gradient tolerance in M4. We have concentrated our effort on the magnet labelled M4 which is the strongest one in the whole arrangement. The tolerances to be imposed on the other magnets can be calculated by straightforward scaling.

Increases in the maximum values of β_H, β_V and α_p contribute to a reduction factor in luminosity in the following way:

i) The momentum spread and hence the current which can be accumulated in a given aperture is reduced by a factor:

$$\frac{\alpha_{p_0}}{\alpha_p} \quad . \qquad (1)$$

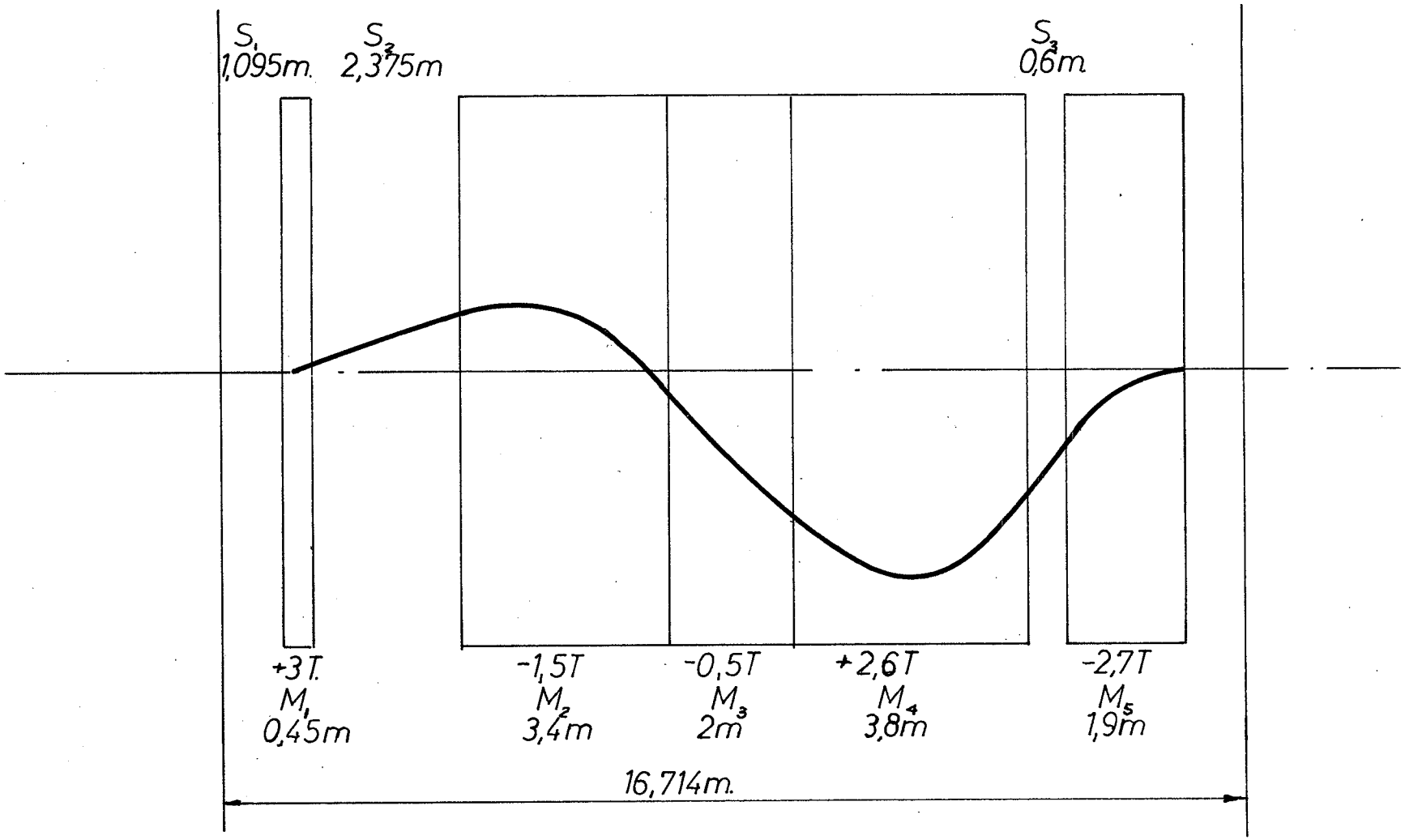

FIG 4.2.5. FIELD DISTRIBUTION ALONG THE BEAM

ii) The aperture available for stacking becomes smaller when the size of the injected and of the circulating beam due to betatron oscillations are increased, and when the injection kicker magnet is not at a maximum of α_p. This is due to the following effect:

There should be 15 mm free space between the injected beam and the stack at the injection kicker magnet to accommodate a screen which protects the stack from the kicker stray field. If α_p at that point is less than the maximum value (as will be the case when α_p has a wiggle on top of the normal one), then this gap will be magnified to 15 $\alpha_{p_{max}}/\alpha_{p_{KM}}$ at the azimuthal position where $\alpha_{p_{max}}$ occurs and where our aperture calculations are done. This reduces the available stack width.

This effect does not occur with the improved PS and two-turn injection into the ISR, since in this case we assume that the injection is done with full-aperture kicker magnets [E. Keil, "Stacking in betatron phase space for the ISR", ISR-TH/67-10 (8.3.1967)].

The ratio taking both the increased beam size and the increased gap between stack and injected beam into account is:

$$\frac{w_o - d_o \left(\alpha_p/\alpha_{p_{KM}}\right) - 2a_o \left(\beta_H/\beta_{H_o}\right)^{1/2}}{w_o - d_o - 2a_o} \quad . \tag{2}$$

iii) The current also depends on the vertical β value if we assume that the present beam height fills the available vertical aperture. The corresponding factor becomes:

$$\frac{\beta_{V_o}}{\beta_V} \quad . \tag{3}$$

iv) With the assumption (iii), the beam height at the intersection point is determined by the ratio of the vertical β values. Hence the ratio of the square roots of the heights becomes:

$$\left(\frac{\beta_{i_o}}{\beta_{V_o}} \cdot \frac{\beta_V}{\beta_i}\right)^{1/4} . \qquad (4)$$

Putting all these factors together we have for the square root of the change in luminosity:

$$L^{1/2} = \frac{\alpha_{p_o}}{\alpha_p} \frac{w_o - d_o\,(\alpha_p/\alpha_{p_{KH}}) - 2a_o\,(\beta_H/\beta_{H_o})}{w_o - d_o - 2a_o}^{1/2} \left(\frac{\beta_{V_o}}{\beta_V}\right)^{3/4} \left(\frac{\beta_{i_o}}{\beta_i}\right)^{1/4} . \qquad (5)$$

We have evaluated this expression for a number of gradients in M4 and for two sets of apertures and beam sizes, the first corresponding to the present PS, the second to an improved PS with multiturn injection [scheme 14a* in C. Bovet and E. Keil, "ISR performances related to CPS injector schemes", MPS/Int. DL/B 67-6 (2.5.1967)]. The numerical values are

	w_o	d_o	$2a_o$
present PS	117	15	56 mm
improved PS	117	0	78 mm

The results are displayed in Table 2; the gradient parameter K is defined as follows:

$$K = \frac{1}{B\rho} \frac{dB}{dx} . \qquad (6)$$

The sign convention is $K < 0$ for horizontally focusing magnets.

Table 2

Gradient tolerance in M4, Omega in intersection region I1

K (m^{-2})	β_H (m)	β_V (m)	$\alpha_{p_{KM}}$ (m)	α_p (m)	Luminosity	
					present PS	improved PS
0.005	49.8	59.1	1.60	3.05	0.14	0.27
0.002	44.2	54.5	1.98	2.60	0.50	0.58
0.001	42.6	53.4	2.12	2.43	0.71	0.76
0.0	41.1	52.3	2.28	2.28	0.96	0.96
-0.001	42.8	51.7	2.40	2.45	0.81	0.78
-0.002	44.6	51.9	2.55	2.65	0.64	0.62
-0.005	50.4	56.1	3.03	3.30	0.28	0.25

It seems desirable to keep the luminosity above 50% of the present value. This limits K to

$$K < 0.002\ m^{-2}$$

which, for $B\rho$ = 100 Tm (about 30 GeV), corresponds to a gradient

$$\frac{dB}{dx} < 20\ \text{gauss/cm}\ .$$

The gradient tolerance can be transformed into a wedge angle tolerance by comparing the focusing action of magnet edges and a gradient. We find that the angle γ between the end faces of the magnet must fulfil the following condition:

$$\gamma < 0.25 \text{ radians.}$$

The Q-shifts resulting from tolerable gradients can easily be taken care of by the correcting equipment in the ISR.

67/1372/5
SIS/sb

4.2.2-3 Estimates for non-linear fields. Here we consider only the quadrupole action of non-linear field components in M4. We impose the condition that at the edge of the aperture x = 0.05 m the resulting gradient should be below tolerance.

Hence, we find for the sextupole component where $K = K'x$:

$$K' < 0.04\ m^{-3}\ ; \quad \frac{d^2B}{dx^2} < 4\ \text{gauss/cm}^2\ ,$$

and for the octupole component where $K = 0.5\ K''x^2$:

$$K'' < 1.6\ m^{-4}\ ; \quad \frac{d^3B}{dx^3} < 1.6\ \text{gauss/cm}^3\ .$$

The genuine non-linear effects of such non-linearities which are smaller than those built into the ISR are not harmful.

4.2.2-4 Magnet ripple. A magnet ripple $\Delta B/B$ causes displacements of the closed orbit with the following maximum amplitude

$$\hat{x} = \frac{\psi}{2} \frac{(\beta \cdot \beta_{max})^{1/2}}{\sin \pi Q}\ , \qquad (7)$$

where ψ is the kick angle due to the ripple:

$$\psi = \varphi \frac{\Delta B}{B}\ .$$

φ is the bending angle. Putting in numbers, in particular $\hat{x} = 1$ mm, yields:

$$\frac{\Delta B}{B} < 3 \times 10^{-4}\ .$$

The setting tolerance for the magnets is the same.

4.2.2-5 Tilt of median plane. Tilts in the median plane of the magnets cause a distortion of the vertical closed orbit, resulting in a reduction of the permissible beam dimensions.

Using a formula similar to Eq. (7) and $\hat{z}$ = 1 mm, we find the tolerance for the tilt angle ψ

$$\psi < 0.3 \text{ mrad.}$$

4.2.2-6 A remark on compensation. All tolerances for gradients given are based on the assumption that an unwanted gradient in the Omega magnet arrangement is not compensated by a correcting magnet nearby. The reason for this is that a good compensation requires that the distance between the source of the error and the correcting device should be small compared to one-half of the local β value. Because of the size of the magnets concerned -- several metres -- and the small vertical β value, this condition cannot be met.

4.3 Possible use of a polarized proton target in the Omega magnet

The main characteristics of a dynamic polarized proton target are:

- the sample X,
- its hydrogen density d_H,
- its contamination by bound protons $n(p \neq H)/n(H)$,
- the magnetic field H,
- its inhomogeneity $\Delta H/H$,
- the operating temperature T,
- the microwave frequency F,
- the target length L,
- and the maximum proton polarization P_n.

The table summarizes these values for (i) the present CERN targets, and (ii) the best results so far achieved in organic compounds.

X	d_H (g/cm^3)	$\frac{n(p \neq H)}{n_H}$	H (kG)	$\frac{\Delta H}{H}$	T (°K)	F (GHz)	L (mm)	P_n (%)	$P_n d_H^{1/2}$
(i) LMN	0.07	15	18.5	10^{-4}	1	70	45	70	1
(ii) Ethanol	0.14	3.3	25	5×10^{-4}	1	70	(45)*)	35	0.7

*) Measurements have been limited to L = 15 mm, but 45 mm should be feasible.

For experiments with a full kinematic separation between scattering events occurring on free protons and on bound protons it is possible that the statistical accuracy is proportional to $P_n d_H^{1/2}$, which is given in arbitrary units in the table. Although in this respect organic targets are not yet as good as LMN targets, we feel confident that by the time the Omega project is achieved this situation will have changed. We thus suggest that the parameters defined for ethanol should be used with a possible stronger requirement on the field homogeneity.

As it is unlikely that the field of the Omega magnet in the position where the target will be located will have the required value and homogeneity, a special set of coils will have to be designed to correct the field shape and to increase locally the field strength. In this way it will also be possible to adjust independently the polarized target field and the Omega magnet.

* * *

APPENDIX

REASONS FOR THE CHOICE OF THE MAGNET SIZE

The total length of the system along the beam should be sufficient to detect the decays of high momentum hyperons. The mean decay lengths at 20 GeV/c are for example:

1.35 m for Λ
0.41 m for Σ^+
0.83 m for $\bar{\Sigma}^-$
1.37 m for Ξ^0
0.79 m for Ξ^-
0.54 m for Ω^-

The corresponding K_1^0 decay length is 1.05 m.

The precision of the momentum determination is limited by two different sources of errors:

i) the error in the position determination of single sparks, which is 0.2 mm (r.m.s. error) for optical chambers [P. Astbury et al., Nucl.Instr. and Methods 46, 61 (1967)];

ii) the multiple scattering by the chamber media (the radiation length of optical chambers with one aluminium foil per cm, each 25 microns thick, is about 30 m).

The error of the momentum determination due to spark position errors is proportional to $L^{-5/2}$ (L = detected track length) if the density of spark chambers is fixed. The error due to multiple scattering, which dominates for large detected track lengths, is proportional to $L^{-1/2}$. Thus it is not reasonable to make the magnet much longer than the critical length L_K at which the influence of both sources of errors is equal:

$$L_K = \left(1.9 \frac{\sigma_Y}{\sqrt{N'}} \cdot \frac{\sqrt{L_o}}{\cos^2 \alpha} \cdot p\right)^{1/2},$$

where

σ_Y = r.m.s. error of spark position measurement (cm)

N' = number of sparks per cm track length

α = angle between track and plane normal to the field

L_o = radiation length (cm)

p = momentum (MeV/c)

For $\sigma_Y = 0.02$ cm, $L_o = 3 \times 10^3$ cm, $N' = 1$ cm^{-1}, $p = 2 \times 10^4$ MeV/c, $\alpha = 0$, one gets $L_K = 200$ cm. (For wire chambers, σ_Y and L_o and thus L_K will be somewhat larger.)

The momentum of backward emitted particles is always very small. The target should therefore be located outside the centre of the magnetic field in upstream beam direction. The reasonable width of the field volume can be derived by calculating the maximum of $L_K \cdot \sin \vartheta$ using the extreme case of $\bar{p}p \rightarrow e^+e^-$ and taking into account that σ_Y be higher and N' be reduced for larger angles. The total width of the used field volume should therefore be about 1.5 m. The gap between the magnet poles has to be the sum of the effective height of the spark chambers plus the frames plus some space for trigger or neutral particle counters. Although the required field width is smaller than its length, a circular coil is a reasonable choice because of its simpler construction and the higher field homogeneity which can be achieved in the used volume.

To compare the accuracy of momentum determination of the proposed system with that which has been used by the CERN-ETH group, the following table gives the relative momentum errors $\Delta p/p$ due to multiple scattering, to the measurement error, and to the combination of both, each for three different momenta and for three different systems:

a) the proposed system with 25 μ Al-foils (1 foil per cm);

b) the same system with 10 μ Al-foils;

c) the CERN-ETH system (25 μ Al-foils, 1 foil per cm, magnetic field 10.5 kG, field length 170 cm, useful width 60 cm).

The errors are calculated for the case where the production angle is zero.

Figure A.1 shows for the three systems the total error of momentum determination as a function of momentum.

System	p (GeV/c)	$\frac{\Delta p}{p}$ (measurement)	$\frac{\Delta p}{p}$ (multiple scattering)	$\frac{\Delta p}{p}$ (total)
a	0.2	1.35×10^{-3}	4.6×10^{-3}	4.8×10^{-3}
	3.0	7.6×10^{-4}	2.8×10^{-3}	3.0×10^{-3}
	20	3.2×10^{-3}	2.8×10^{-3}	4.2×10^{-3}
b	0.2	1.35×10^{-3}	3.2×10^{-3}	3.6×10^{-3}
	3.0	7.6×10^{-4}	2.0×10^{-3}	2.4×10^{-3}
	20	3.2×10^{-3}	2.0×10^{-3}	3.8×10^{-3}
c	0.2	2.5×10^{-3}	1.06×10^{-2}	1.1×10^{-2}
	1.5	1.7×10^{-3}	6.8×10^{-3}	6.9×10^{-3}
	20	1.6×10^{-2}	6.3×10^{-3}	1.8×10^{-2}

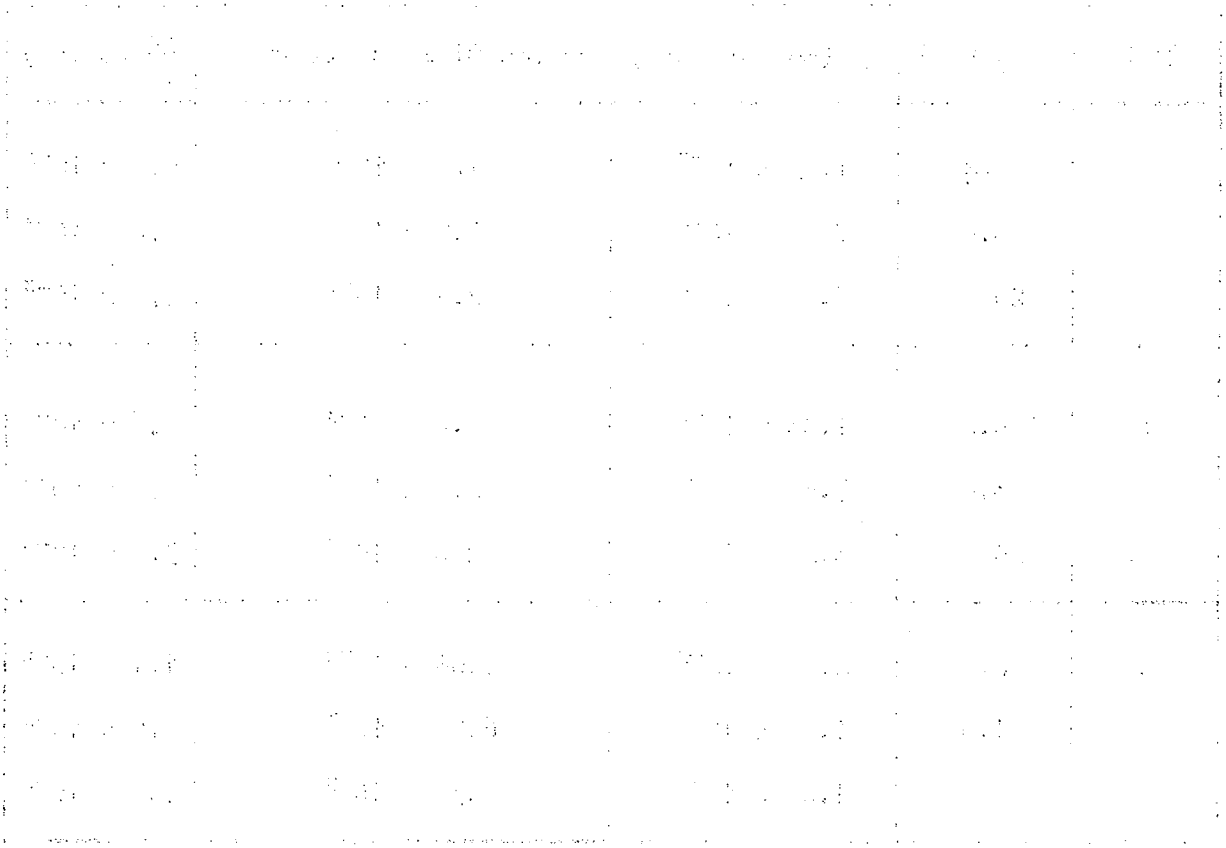

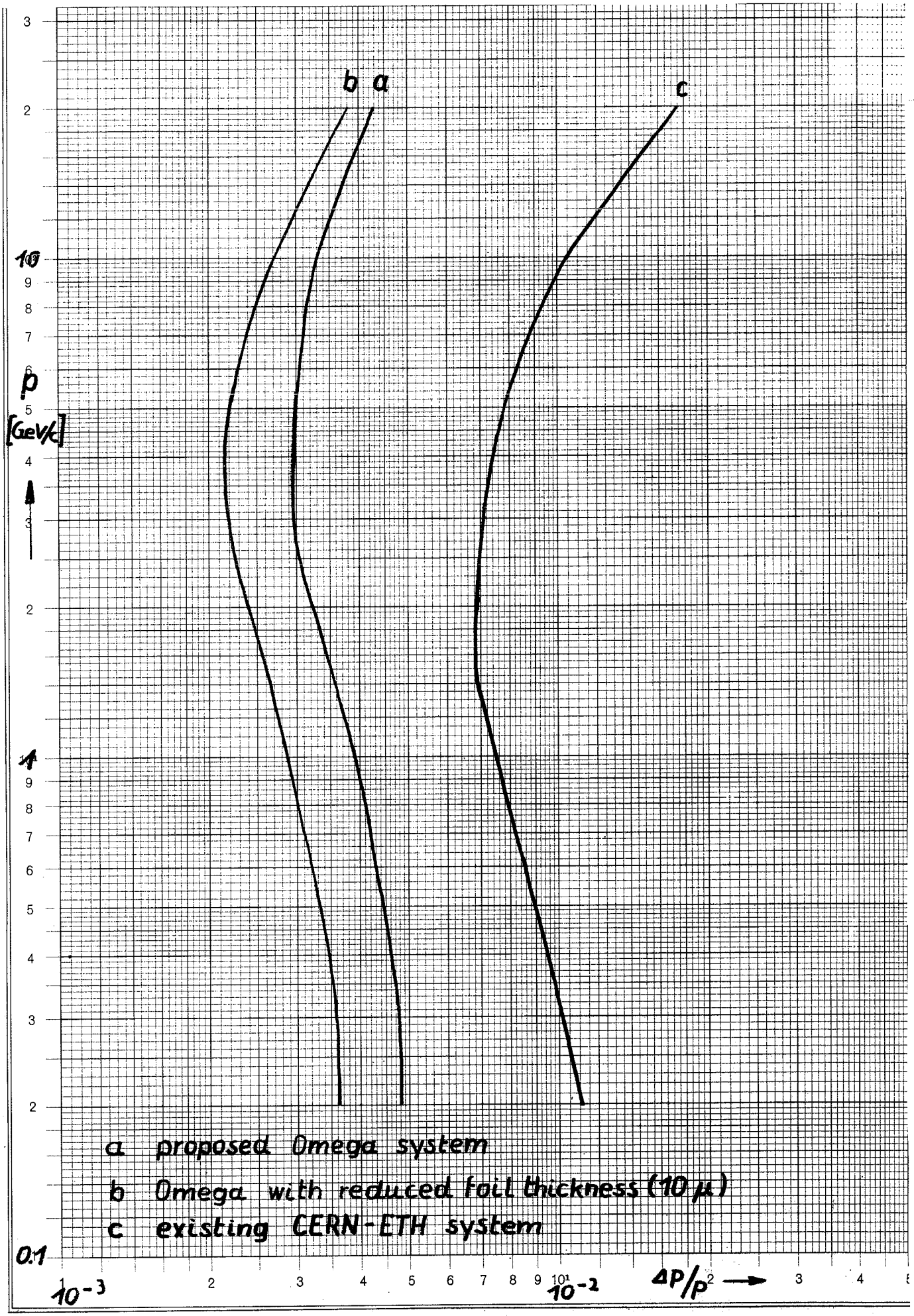

Logar. Teilung / Division } 1-10000 und 1-100000 Einheit / Unité } 100 mm

Fig. A 1 Error of momentum determination